27. Nanotribology, Nanomechanics and Materials Characterization

Bharat Bhushan

Nanotribology and nanomechanics studies are needed to develop a fundamental understanding of interfacial phenomena on a small scale, and to study interfacial phenomena in micro/nanoelectromechanical systems (MEMS/NEMS), magnetic storage devices, and many other applications. Friction and wear of lightly loaded micro/nanocomponents are highly dependent on surface interactions (a few atomic layers). These structures are generally coated with molecularly thin films. Nanotribology and nanomechanics studies are also valuable in the fundamental understanding of interfacial phenomena in macrostructures, and provide a bridge between science and engineering. An atomic force microscope (AFM) tip is used to simulate a single-asperity contact with a solid or lubricated surface. AFMs are used to study the various tribological phenomena, which include surface roughness, adhesion, friction, scratching, wear, detection of material transfer, and boundary lubrication. In situ surface characterization of local deformation of materials and thin coatings can be carried out using a tensile stage inside an AFM. Mechanical properties such as hardness, Young's modulus of elasticity, and creep/relaxation behavior can be determined on micro- to picoscales using a depth-sensing indentation system in an AFM. Localized surface elasticity and viscoelastic mapping near surface regions can be obtained with nanoscale lateral resolution. Finally, an AFM can be used for nanofabrication/nanomachining.

The mechanisms and dynamics of the interactions of two contacting solids during relative motion, ranging from atomic scale to microscale, need to be understood in order to develop a fundamental understanding of adhesion, friction, wear, indentation, and lubrication processes. For most solid–solid interfaces of technological relevance, contact occurs at multiple asperities. Consequently, the importance of investigating single-asperity contacts in studies of the fundamental micro/nanomechanical and micro/nanotribological properties of surfaces and interfaces has long been recognized. The emergence and proliferation of proximal probes, in particular scanning probe microscopies (the scanning tunneling microscope and the atomic force microscope), the surface force apparatus, and computational techniques for simulating tip–surface interactions and interfacial properties, allowed systematic investigations of interfacial problems with high resolution as well as ways and means for modifying and manipulating nanoscale structures. These advances led to the appearance of the field of nanotribology. The word nanotribology was used for the first time in the title of a research paper by *Bhushan* et al. [27.1] and a first book on the field by Bhushan in 1995 (first edition of [27.2]). The first dedicated international meeting on the topic was organized in 1996 in Sesimbra, Portugal [27.3].

Nanotribology pertains to experimental and theoretical investigations of interfacial processes on scales ranging from the atomic- and molecular scale to the microscale, occurring during adhesion, friction, scratching, wear, indentation, and thin-film lubrication at sliding surfaces [27.1–14]. Proximal probes have also been used for mechanical and electrical characterization, in situ characterization of local deformation, and other nanomechanics studies [27.8, 11, 14, 15].

Nanotribological and nanomechanical studies are needed to develop a fundamental understanding of interfacial phenomena on a small scale, and to study interfacial phenomena in nanostructures used in magnetic storage devices, micro/nanoelectromechanical systems (MEMS/NEMS), and other applications [27.1–3, 7–20]. Friction and wear of lightly loaded micro/nanocomponents are highly dependent on surface interactions (a few atomic layers). These structures are generally coated with molecularly thin films. Nanotribological and nanomechanical studies also are valuable in the fundamental understanding of interfacial phenomena in macrostructures, and provide a bridge between science and engineering.

The surface force apparatus (SFA), the scanning tunneling microscopes (STMs), and atomic force and friction force microscopes (AFM and FFMs) are used widely in nanotribological and nanomechanical studies. Typical operating parameters are compared in Table 27.1. The SFA, developed in 1968, is commonly employed to study both static and dynamic properties of molecularly thin films sandwiched between two molecularly smooth surfaces. The STM, developed in 1981, allows the imaging of electrically conducting surfaces with atomic resolution, and has been used for the imaging of clean surfaces as well as of lubricant molecules. The introduction of the AFM in 1985 provided a method for measuring ultrasmall forces between a probe tip and an engineering (electrically conducting or insulating) surface. AFM has been used for morphological and surface roughness measurements of surfaces on the nanoscale, as well as for adhesion measurements. Subsequent modifications of the AFM led to the development of the FFM, designed for atomic- and microscale studies of friction. This instrument measures forces in the scanning direction. The AFM is being used

Table 27.1 Comparison of typical operating parameters in SFA, STM, and AFM/FFM used for micro/nanotribological studies

Operating parameter	SFA	STM[a]	AFM/FFM
Radius of mating surface/tip	$\approx 10\,\text{mm}$[b]	$5-100\,\text{nm}$	$5-100\,\text{nm}$
Radius of contact area	$10-40\,\mu\text{m}$	N/A	$0.05-0.5\,\text{nm}$
Normal load	$10-100\,\text{mN}$	N/A	$< 0.1-500\,\text{nN}$
Sliding velocity	$0.001-100\,\mu\text{m/s}$	$0.02-200\,\mu\text{m/s}$ (scan size $\approx 1\,\text{nm} \times 1\,\text{nm}$ to $125\,\mu\text{m} \times 125\,\mu\text{m}$; scan rate $< 1-122\,\text{Hz}$)	$0.02-200\,\mu\text{m/s}$ (scan size $\approx 1\,\text{nm} \times 1\,\text{nm}$ to $125\,\mu\text{m} \times 125\,\mu\text{m}$; scan rate $< 1-122\,\text{Hz}$)
Sample limitations	Typically atomically smooth, optically transparent mica; opaque ceramic, smooth surfaces can also be used	Electrically conducting samples	None of the above

[a] Can be used for atomic-scale imaging.
[b] Since stresses scale inverse of tip radius, SFA can provide very low stress measurement capabilities.

for various investigations including scratching, wear, indentation, detection of transfer of material, boundary lubrication, and fabrication and machining [27.1, 2, 14, 15]. Meanwhile, significant progress in understanding the fundamental nature of bonding and interactions in materials, combined with advances in computer-based modeling and simulation methods, has allowed theoretical studies of complex interfacial phenomena with high resolution in space and time. Such simulations provide insights into atomic-scale energetics, structure, dynamics, thermodynamics, transport, and rheological aspects of tribological processes.

The nature of interactions between two surfaces brought together closely, and those between two contacting surfaces as they are separated, have been studied experimentally with the SFA. This has led to a basic understanding of the normal forces between surfaces and the way in which these are modified by the presence of thin liquid or a polymer film. The frictional properties of such systems have been studied by moving the surfaces laterally. Such experiments have provided insights into the molecular-scale operation of lubricants such as thin
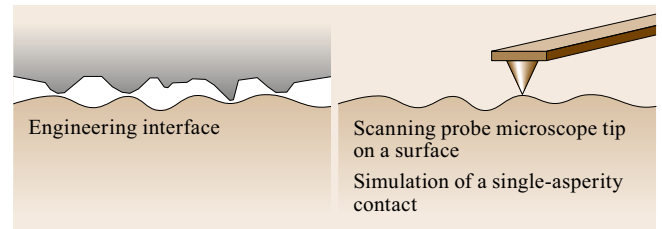
Fig. 27.1 Schematics of an engineering interface and scanning probe microscope tip in contact with an engineering interface

liquid or polymer films. Complementary to these studies are those in which the AFM tip is used to simulate a single-asperity contact with a solid or lubricated surface (Fig. 27.1). These experiments have demonstrated that the relationship between friction and surface roughness is not always simple or obvious. AFM studies have also revealed much about the nanoscale nature of intimate contact during wear, indentation, and lubrication.

In this chapter, we present a review of significant aspects of nanotribological, nanomechanical, and materials characterization studies conducted using AFM/FFM.

27.1 Description of AFM/FFM and Various Measurement Techniques

The AFM was developed by Gerd Binnig et al. in 1985. It is capable of investigating surfaces of scientific and engineering interest on an atomic scale [27.21, 22]. The AFM relies on a scanning technique to produce very high-resolution, three-dimensional images of sample surfaces. It measures ultrasmall forces (less than 1 nN) present between the AFM tip surface mounted on a flexible cantilever beam and a sample surface. These small forces are obtained by measuring the motion of a very flexible cantilever beam having an ultrasmall mass, by a variety of measurement techniques including optical deflection, optical interference, capacitance, and tunneling current. The deflection can be measured to within 0.02 nm, so for a typical cantilever spring constant of 10 N/m, a force as low as 0.2 nN can be detected. To put these numbers in perspective, individual atoms and human hair are typically a fraction of a nanometer and about 75 µm in diameter, respectively, and a drop of water and an eyelash have a mass of about 10 µN and 100 nN, respectively. In the operation of high-resolution AFM, the sample is generally scanned rather than the tip because any cantilever movement would add vibrations. AFMs are available for the measurement of large samples, where the tip is scanned and the sample is stationary. To obtain an atomic resolution with the AFM, the spring constant of the cantilever should be weaker than the equivalent

spring between atoms. A cantilever beam with a spring constant of about 1 N/m or lower is desirable. For high lateral resolution, tips should be as sharp as possible. Tips with a radius ranging from 5 to 50 nm are commonly available. Interfacial forces, adhesion, and surface roughness, including atomic-scale imaging, are routinely measured using the AFM.

A modification to the AFM providing a sensor to measure the lateral force led to the development of the friction force microscope (FFM) or the lateral force microscope (LFM), designed for atomic- and microscale studies of friction [27.1–3, 7, 9, 10, 14, 23–38] and lubrication [27.12, 20, 39, 39–54]. This instrument measures lateral or friction forces (in the plane of the sample surface and in the scanning direction). By using a standard or a sharp diamond tip mounted on a stiff cantilever beam, AFM is used in investigations of scratching and wear [27.1, 2, 7, 8, 11, 28, 55–58], nanoindentation [27.1, 11, 18, 28, 59–63], and nanofabrication/machining [27.2, 20, 28]. An oscillating cantilever is used for localized surface elasticity and viscoelastic mapping, referred to as dynamic AFM [27.36, 64–72]. In situ surface characterization of local deformation of materials and thin coatings has been carried out by imaging the sample surfaces using an AFM, during tensile deformation using a tensile stage [27.73–75].
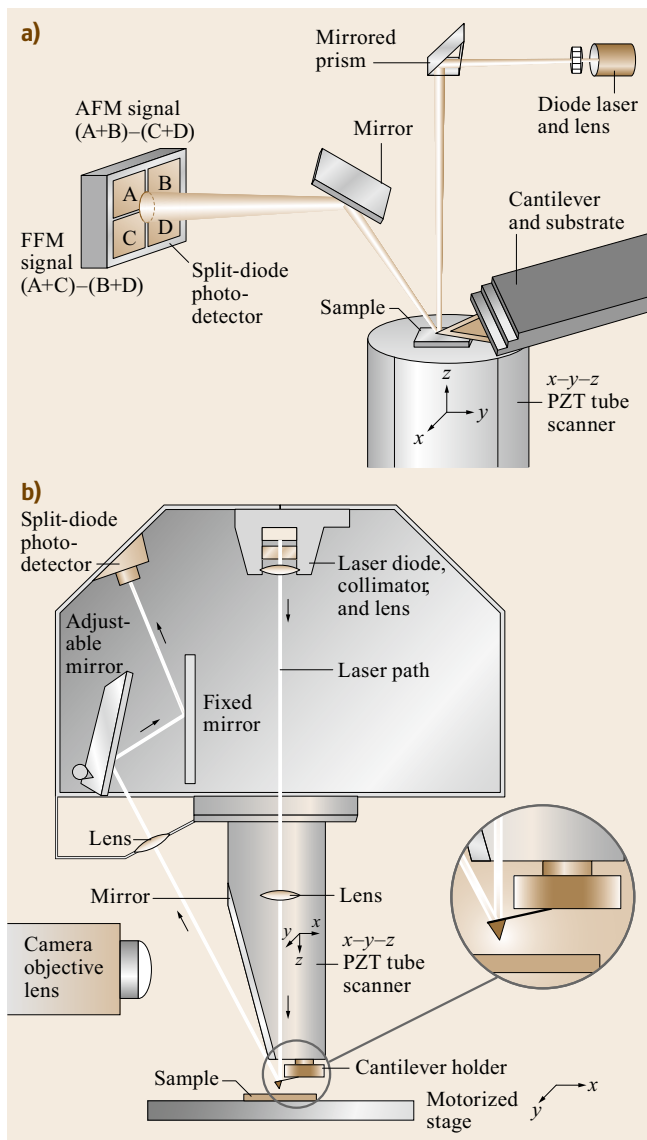
27.1.1 Surface Roughness and Friction Force Measurements

Surface height imaging down to atomic resolution of electrically conducting surfaces is carried out using an STM. An AFM is also used for surface height imaging and roughness characterization down to nanoscale. Commercial AFM/FFM are routinely used for simultaneous measurements of surface roughness and friction force [27.2, 14]. These instruments are available for the measurement of small samples and large samples. In

Fig. 27.2a,b Schematics (**a**) of a commercial small-sample atomic force microscope/friction force microscope (AFM/FFM), and (**b**) of a large-sample AFM/FFM

a small-sample AFM shown in Fig. 27.2a, the sample, generally no larger than $10\,\mathrm{mm} \times 10\,\mathrm{mm}$, is mounted on a piezoelectric crystal in the form of a cylindrical tube (referred to as a PZT tube scanner) which consists of separate electrodes to scan the sample precisely in the x–y plane in a raster pattern and to move the sample in the vertical (z) direction. A sharp tip at the free end of a flexible cantilever is brought into contact with the sample. The normal and frictional forces being applied at the tip–sample interface are measured using a laser beam deflection technique. A laser beam from a diode laser is directed by a prism onto the back of a cantilever near its free end, tilted downward at about $10°$ with respect to the horizontal plane. The reflected beam from the vertex of the cantilever is directed through a mirror onto a quad photodetector (a split photodetector with four quadrants). The differential signal from the top and bottom photodiodes provides the AFM signal which is a sensitive measure of the cantilever vertical deflection. Topographic features of the sample cause the tip to deflect in the vertical direction as the sample is scanned under the tip. This tip deflection will change the direction of the reflected laser beam, changing the intensity difference between the top and bottom sets of photodetectors (the AFM signal). In the AFM operating mode called the height mode, for topographic imaging or for any other operation in which the applied normal force is to be kept constant, a feedback circuit is used to modulate the voltage applied to the PZT scanner to adjust the height of the PZT, so that the cantilever vertical deflection (given by the intensity difference between the top and bottom detector) will remain constant during scanning. The PZT height variation is thus a direct measure of the surface roughness of the sample.

In a large-sample AFM, both force sensors using the optical deflection method and a scanning unit are mounted on the microscope head (Fig. 27.2b). Because of vibrations caused by the cantilever movement, lateral resolution of this design can be somewhat poorer than the design in Fig. 27.2a in which the sample is scanned instead of the cantilever beam. The advantage of the large-sample AFM is that large samples can be measured readily.

Most AFMs can be used for surface roughness measurements in the so-called tapping mode (TM) (intermittent contact mode), also referred to as dynamic (atomic) force microscopy. In the tapping mode, during scanning over the surface, the cantilever/tip assembly with a normal stiffness of $20-100\,\mathrm{N/m}$ (Bruker tapping mode etched Si probe or TESP) is sinusoidally vibrated at its resonance frequency ($350-400\,\mathrm{kHz}$) by a piezo mounted above it, and the oscillating tip slightly taps the surface. The piezo is adjusted using the feedback control in the z-direction to maintain a constant

Nanotribology, Nanomechanics and Materials Characterization | 27.1 Description of AFM/FFM and Various Measurement Techniques | 873

Part F | 27.1

(20−100 nm) oscillating amplitude (setpoint) and constant average normal force (Fig. 27.3) [27.2, 14]. The feedback signal to the z-direction sample piezo (to keep the setpoint constant) is a measure of surface roughness. The cantilever/tip assembly is vibrated at some amplitude, here referred to as the free amplitude, before the tip engages the sample. The tip engages the sample at some setpoint, which may be thought of as the amplitude of the cantilever as influenced by contact with the sample. The setpoint is defined as a ratio of the vibration amplitude after engagement to the vibration amplitude in free air before engagement. A lower setpoint gives a reduced amplitude and closer mean tip-to-sample distance. The amplitude should be kept large enough so that the tip does not get stuck to the sample because of adhesive attractions. Also the oscillating amplitude applies less average (normal) load as compared to the contact mode and reduces sample damage. The tapping mode is used in topography measurements to minimize the effects of friction and other lateral forces and to measure topography of soft surfaces.

To measure the friction force at the tip surface during sliding, the left hand and right hand sets of quadrants of the photodetector are used. In the so-called friction mode, the sample is scanned back and forth in a direction orthogonal to the long axis of the cantilever beam. A friction force between the sample and the tip will produce a twisting of the cantilever. As a result, the laser beam will be reflected out of the plane defined by the incident beam and the beam reflected vertically from an untwisted cantilever. This produces an intensity difference of the laser beam received in the left hand and right hand sets of quadrants of the photodetector. The intensity difference between the two sets of detectors (FFM signal) is directly related to the degree of twisting and hence to the magnitude of the friction force. One problem associated with this method is that any misalignment between the laser beam and the photodetector axis would introduce error in the measurement. However, by following the procedures developed by *Ruan* and *Bhushan* [27.25], in which the average FFM signal for the sample scanned in two opposite directions is subtracted from the friction profiles of each of the two scans, the misalignment effect is eliminated. This method provides three-dimensional maps of friction force. By following the friction force calibration procedures developed by *Ruan* and *Bhushan* [27.25], voltages corresponding to friction forces can be converted to force units [27.76, 77]. The coefficient of friction is obtained from the slope of friction force data measured as a function of normal loads typically ranging from 10 to 150 nN. This approach eliminates any contributions due to the adhesive forces [27.28]. To calculate the coefficient of friction based on a single point

measurement, friction force should be divided by the sum of the applied normal load and intrinsic adhesive
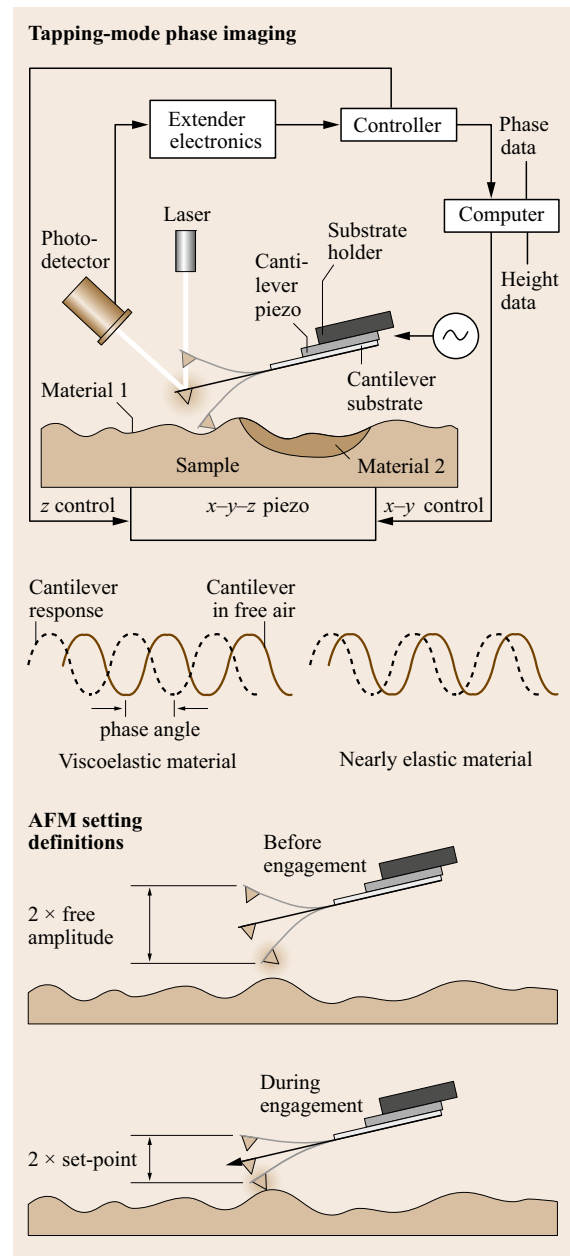
Fig. 27.3 Schematic of tapping mode used to obtain height and phase data and definitions of free amplitude and setpoint. During scanning, the cantilever is vibrated at its resonance frequency and the sample x–y–z piezo is adjusted by feedback control in the z-direction to maintain a constant setpoint. The computer records height (which is a measure of surface roughness) and phase angle (which is a function of the viscoelastic properties of the sample) data

force. Furthermore, it should be pointed out that for a single-asperity contact, the coefficient of friction is not independent of load (see discussion later).
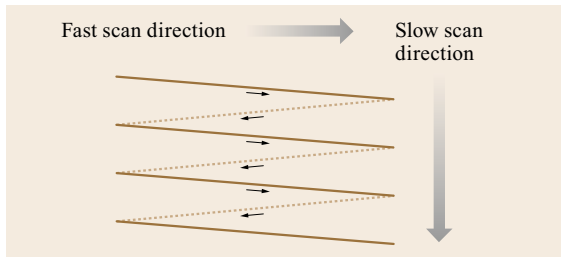
Surface roughness measurements in the contact mode are typically made using a sharp, microfabricated square-pyramidal Si_3N_4 tip with a radius of $30-50$ nm on a triangular cantilever beam (Fig. 27.4a) with normal stiffness on the order of $0.06-0.58$ N/m with a normal natural frequency of $13-40$ kHz (Bruker silicon nitride probe or NP) at a normal load of about 10 nN, and friction measurements are carried out in the load range of $1-100$ nN. Surface roughness measurements in the tapping mode utilize a stiff cantilever with high resonance frequency; typically a square-pyramidal etched single-crystal silicon tip, with a tip radius of $5-10$ nm, integrated with a stiff rectangular silicon cantilever beam (Fig. 27.4a) with a normal stiffness on the order of $17-60$ N/m and a normal resonance frequency of $250-400$ kHz (DI TESP), is used. Multiwalled car-

bon nanotube (MWNT) tips having a small diameter (few nm) and a length of about $1\,\mu m$ (high aspect ratio) attached on the single-crystal silicon, square-pyramidal tips are used for the high-resolution imaging of surfaces and of deep trenches in the tapping mode (noncontact mode) (Fig. 27.4b) [27.78]. The MWNT tips are hydrophobic. To study the effect of radius of a single asperity (tip) on adhesion and friction, microspheres of silica with radii ranging from about 4 to $15\,\mu m$ are attached at the end of cantilever beams. Optical micrographs of two of the microspheres at the ends of triangular cantilever beams are shown in Fig. 27.4c.

The tip is scanned in such a way that its trajectory on the sample forms a triangular pattern (Fig. 27.5). Scanning speeds in the fast and slow scan directions depend on the scan area and scan frequency. Scan sizes ranging from less than 1×1 nm to $125 \times 125\,\mu m$ and scan rates from less than 0.5 to 122 Hz typically can be used. Higher scan rates are used for smaller scan lengths. For
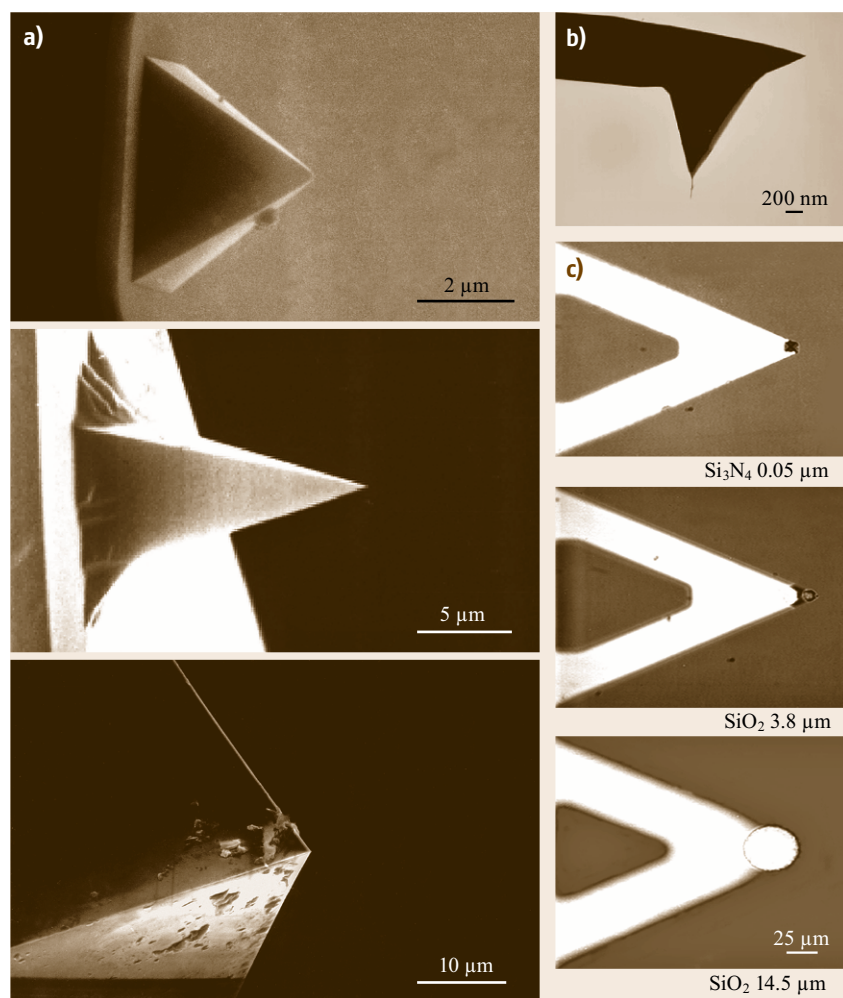
Fig. 27.4 **(a)** SEM micrographs of a square-pyramidal plasma-enhanced chemical vapor deposition (PECVD) Si_3N_4 tip with a triangular cantilever beam, a square-pyramidal etched single-crystal silicon tip with a rectangular silicon cantilever beam, and a three-sided pyramidal natural diamond tip with a square stainless steel cantilever beam. **(b)** SEM micrograph of a MWNT physically attached on the single-crystal silicon, square-pyramidal tip, and **(c)** optical micrographs of a commercial Si_3N_4 tip and two modified tips showing SiO_2 spheres mounted over the sharp tip, at the end of the triangular Si_3N_4 cantilever beams (radii of the tips are given in the figure)

Nanotribology, Nanomechanics and Materials Characterization | 27.1 Description of AFM/FFM and Various Measurement Techniques   875

Part F | 27.1

Fig. 27.5 Schematic of triangular pattern trajectory of the tip as the sample (or the tip) is scanned in two dimensions. During scanning, data are recorded only during scans along the *solid scan lines*
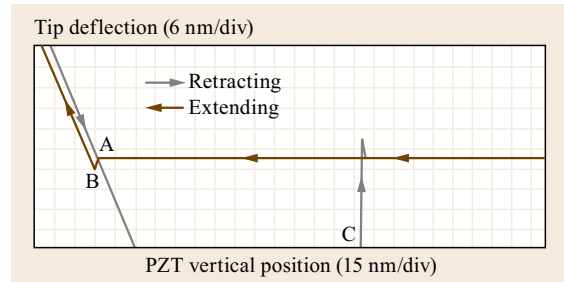

Fig. 27.6 Typical force–distance curve for contact between an Si_3N_4 tip and single-crystal silicon surface in measurements made in the ambient environment. Snap-in occurs at point A; contact between the tip and silicon occurs at point B; tip breaks free of adhesive forces at point C as the sample moves away from the tip

example, scan rates in the fast and slow scan directions for an area of $10\,\mu m \times 10\,\mu m$ scanned at $0.5\,Hz$ are $10\,\mu m/s$ and $20\,nm/s$, respectively.

27.1.2 Adhesion Measurements

Adhesive force measurements are performed in the so-called force calibration mode. In this mode, force-distance curves are obtained, for an example see Fig. 27.6. The horizontal axis gives the distance that the piezo (and hence the sample) travels, and the vertical axis gives the tip deflection. As the piezo extends, it approaches the tip, which is at this point in free air and hence shows no deflection. This is indicated by the flat portion of the curve. As the tip approaches the sample within a few nanometers (point A), an attractive force exists between the atoms of the tip surface and the atoms of the sample surface. The tip is pulled towards the sample and contact occurs at point B on the graph. From this point on, the tip is in contact with the surface and as the piezo further extends, the tip gets further deflected. This is represented by the sloped portion of the curve. As the piezo retracts, the tip goes beyond the zero deflection (flat) line because of attractive forces (van der Waals forces and long-range meniscus forces), into the adhesive regime. At point C in the graph, the tip snaps free of the adhesive forces and is again in free air. The horizontal distance between points B and C along the retrace line gives the distance moved by the tip in the adhesive regime. This distance multiplied by the stiffness of the cantilever gives the adhesive force. Incidentally, the horizontal shift between the loading and unloading curves results from the hysteresis in the PZT tube [27.2, 14].

27.1.3 Scratching, Wear, and Fabrication/Machining

For microscale scratching, microscale wear, nanofabrication/nanomachining, and nanoindentation hardness

measurements, an extremely hard tip is required. A three-sided pyramidal single-crystal natural diamond tip with an apex angle of $80°$ and a radius of about $100\,nm$ mounted on a stainless steel cantilever beam with normal stiffness of about $25\,N/m$ is used at relatively higher loads ($1-150\,\mu N$; Fig. 27.4a). For scratching and wear studies, the sample is generally scanned in a direction orthogonal to the long axis of the cantilever beam (typically at a rate of $0.5\,Hz$) so that friction can be measured during scratching and wear. The tip is mounted on the cantilever such that one of its edges is orthogonal to the long axis of the beam. Therefore, wear during scanning along the beam axis is higher (about $2-3\times$) than that during scanning orthogonal to the beam axis. For wear studies, an area on the order of $2\,\mu m \times 2\,\mu m$ is scanned at various normal loads (ranging from 1 to $100\,\mu N$) for a selected number of cycles [27.2, 14, 28].

Scratching can also be performed at ramped loads and the coefficient of friction can be measured during scratching [27.58]. A linear increase in the normal load approximated by a large number of normal load increments of small magnitude is applied using a software interface (lithography module in Nanoscope III) that allows the user to generate controlled movement of the tip with respect to the sample. The friction signal is tapped out of the AFM and is recorded on a computer. A scratch length on the order of $25\,\mu m$ and a velocity on the order of $0.5\,\mu m/s$ are used and the number of loading steps is usually taken to be 50.

Nanofabrication/nanomachining is conducted by scratching the sample surface with a diamond tip at specified locations and scratching angles. The normal load used for scratching (writing) is on the order of $1-100\,\mu N$ with a writing speed on the order of $0.1-200\,\mu m/s$ [27.2, 8, 14, 20, 28, 79].

27.1.4 Surface Potential Measurements

Various electrical measurements on the nanoscale can be made using a conducting tip. The conducting tip acts as a voltage electrode to provide stimuli and monitor surface electrical properties [27.80]. Various electrical techniques are used and include scanning Kelvin probe microscopy (SKPM), scanning capacitance microscopy (SCM), and scanning spreading resistance microscopy (SSRM) [27.53, 81, 82].
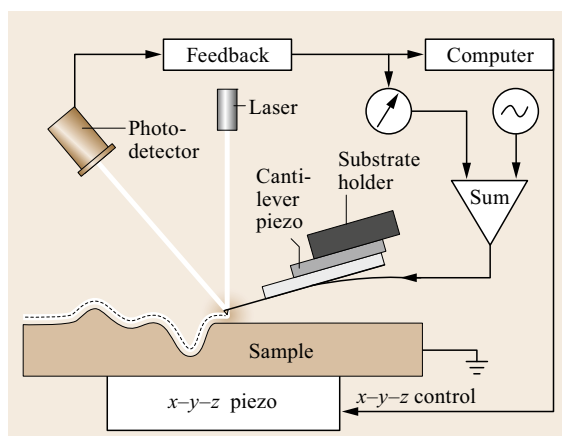
Kelvin probe microscopy can be used to detect wear precursors and to study the early stages of localized wear [27.81, 83, 84]. In this technique (also called *nano-Kelvin probe* technique), the potential difference is measured between the tip and the sample by applying a DC bias potential and an oscillating (AC (alternating current)) potential to a conducting tip over a grounded substrate. Mapping of the surface potential is carried out in the so-called *lift mode* (Fig. 27.7). These measurements are made simultaneously with the topography scan in the tapping mode, using an electrically conducting (nickel-coated single-crystal silicon) tip. After each line of the topography scan is completed, the feedback loop controlling the vertical piezo is turned off, and the tip is lifted from the surface and traced over the same topography at a constant distance of 100 nm. During the lift mode, a DC bias potential

Fig. 27.7 Schematic of lift mode used to make surface potential measurement. The topography is collected in tapping mode in the primary scan. The cantilever piezo is de-activated. Using topography information of the primary scan, the cantilever is scanned across the surface at a constant height above the sample. An oscillating voltage at the resonant frequency is applied to the tip and a feedback loop adjusts the DC (direct current) bias of the tip to maintain the cantilever amplitude at zero. The output of the feedback loop is recorded by the computer and becomes the surface potential map

and an oscillating potential (3−7 V) is applied to the tip. The frequency of oscillation is chosen to be equal to the resonance frequency of the cantilever (≈ 80 kHz). When a DC bias potential equal to the negative value of surface potential of the sample (on the order of +2 V) is applied to the tip, it does not vibrate. During scanning, a difference between the DC bias potential applied to the tip and the potential of the surface will create DC electric fields that interact with the oscillating charges (as a result of the AC potential), causing the cantilever to oscillate at its resonance frequency, as in tapping mode. However, a feedback loop is used to adjust the DC bias on the tip to exactly nullify the electric field, and thus the vibrations of the cantilever. The required bias voltage follows the localized potential of the surface. The surface potential was obtained by reversing the sign of the bias potential provided by the electronics [27.81, 84].

Surface and subsurface changes of structure and/or chemistry can cause changes in the measured potential of a surface. Thus, mapping of the surface potential after sliding can be used for detecting wear precursors and studying the early stages of localized wear [27.81, 83, 84].
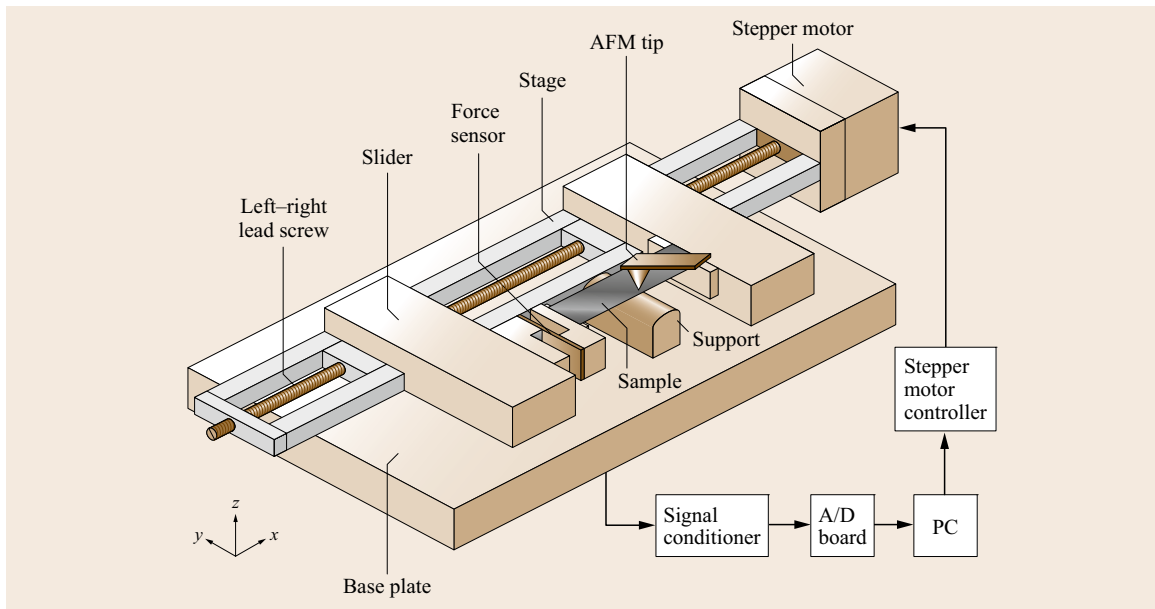
27.1.5 In situ Characterization of Local Deformation Studies

In situ characterization of local deformation of materials can be carried out by performing tensile, bending, or compression experiments inside an AFM and by observing nanoscale changes during the deformation experiment [27.18]. In these experiments, small deformation stages are used to deform the samples inside an AFM. For tensile testing of the polymeric films carried out by *Bobji* and *Bhushan* [27.73, 74] and *Tambe* and *Bhushan* [27.75] and of the hair by *Seshadri* and *Bhushan* [27.85, 86], a tensile stage was used (Fig. 27.8). The stage with a left-right combination lead screw (which helps to move the slider in the opposite direction) was used to stretch the sample to minimize the movement of the scanning area, which was kept close to the center of the tensile specimen. One end of the sample was mounted on the slider via a force sensor to monitor the tensile load. The samples were stretched for various strains using a stepper motor and the same control area at different strains was imaged. In order to better locate the control area for imaging, a set of four markers was created at the corners of a 30 μm × 30 μm square at the center of the sample by scratching the sample with a sharp silicon tip. The scratching depth was controlled such that it did not affect the cracking behavior of the coating. A minimum displacement of 1.6 μm could be obtained. This corresponded to a strain

Fig. 27.8 Schematic of the tensile stage to conduct in situ tensile testing of the polymeric films in AFM

increment of $8 \times 10^{-3}\%$ for a sample length of 38 mm. The maximum travel distance was about 100 mm. The resolution of the force sensor was 10 mN with a capacity of 45 N. While stretching, a stress–strain curve was obtained during the experiment to study any correlation between the degree of plastic strain and the propensity of cracks.

27.1.6 Nanoindentation Measurements

For nanoindentation hardness measurements the scan size is set to zero, and then a normal load is applied to make the indents using the diamond tip. During this procedure, the tip is continuously pressed against the sample surface for about two seconds at various indentation loads. The sample surface is scanned before and after the scratching, wear, or indentation to obtain the initial and the final surface topography, at a low normal load of about 0.3 μN using the same diamond tip. An area larger than the indentation region is scanned to observe the indentation marks. Nanohardness is calculated by dividing the indentation load by the projected residual area of the indents [27.61].

Direct imaging of the indent allows one to quantify piling up of ductile material around the indenter. However, it becomes difficult to identify the boundary of the indentation mark with great accuracy. This makes the direct measurement of contact area somewhat inaccurate. A technique with the dual capability of depth-sensing as well as in situ imaging, which is most appropriate in nanomechanical property studies, is used

for accurate measurement of hardness with shallow depths [27.2, 14, 60]. This nano/picoindentation system is used for the load–displacement measurement process and for subsequent in situ imaging of the indent, if required. The indentation system, shown in Fig. 27.9, consists of a three-plate transducer with electrostatic actuation hardware used for the direct application of a normal load and a capacitive sensor used for the measurement of vertical displacement. The AFM head is replaced with this transducer assembly while the specimen is mounted on the PZT scanner, which remains stationary during indentation experiments. The transducer consists of a three (Be-Cu)-plate capacitive structure, and the tip is mounted on the center plate. The upper and lower plates serve as drive electrodes, and the load is applied by applying appropriate voltage to the drive
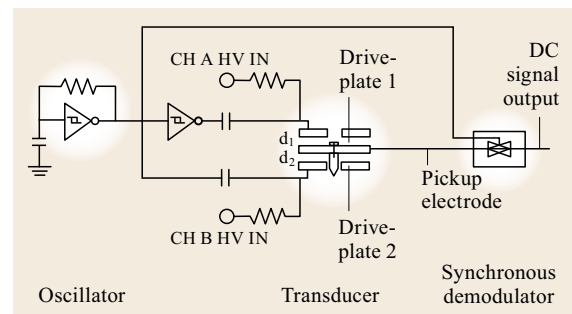
Fig. 27.9 Schematic of a nano/picoindentation system with three-plate transducer with electrostatic actuation hardware and capacitance sensor (after [27.60])

electrodes. Vertical displacement of the tip (indentation depth) is measured by measuring the displacement of the center plate relative to the two outer electrodes using the capacitance technique. Indent area and consequently hardness value can be obtained from the load–displacement data. The Young's modulus of elasticity is obtained from the slope of the unloading curve.

27.1.7 Localized Surface Elasticity and Viscoelasticity Mapping

Localized Surface Elasticity
Indentation experiments provide a single-point measurement of the Young's modulus of elasticity calculated from the slope of the indentation curve during unloading. Localized surface elasticity maps can be obtained using dynamic force microscopy, in which an oscillating tip is scanned over the sample surface in contact under steady and oscillating load. Lower frequency operation modes in the kHz range, such as force modulation mode [27.64, 66] or pulsed force mode [27.87], are well suited for soft samples such as polymers. However, if the tip-sample contact stiffness becomes significantly higher than the cantilever stiffness, the sensitivity of these techniques strongly decreases. In this case, sensitivity of the measurement of stiff materials can be improved by using high-frequency operation modes in the MHz range with a lateral motion, such as acoustic (ultrasonic) force microscopy, referred to as atomic force acoustic microscopy (AFAM), or contact resonance spectroscopy [27.68, 88, 89]. Inclusion of vibration frequencies other than only the first cantilever flexural or torsional resonance frequency also allows additional information to be obtained.

In the negative lift mode force modulation technique, during primary scanning height data is recorded in tapping mode as described earlier. During interleave scanning, the entire cantilever/tip assembly is moved up and down at the force modulation holder's bimorph resonance frequency (about 24 kHz) at some amplitude, here referred to as the force modulation amplitude, and the z-direction feedback control for the sample x–y–z piezo is deactivated (Fig. 27.10a) [27.64, 66, 69]. During this scanning process, height information from the primary scan is used to maintain a constant lift scan height. This eliminates the influence of height on the measured signals during the interleave scan. Lift scan height is the mean tip-to-sample distance between the tip and sample during the interleave scan. The lift scan height is set such that the tip is in constant contact with the sample, i.e., a constant static load is applied. (A higher lift scan height gives a closer mean tip-to-sample distance.) In addition, the tip motion caused by the bimorph vibration results in a modulating pe-
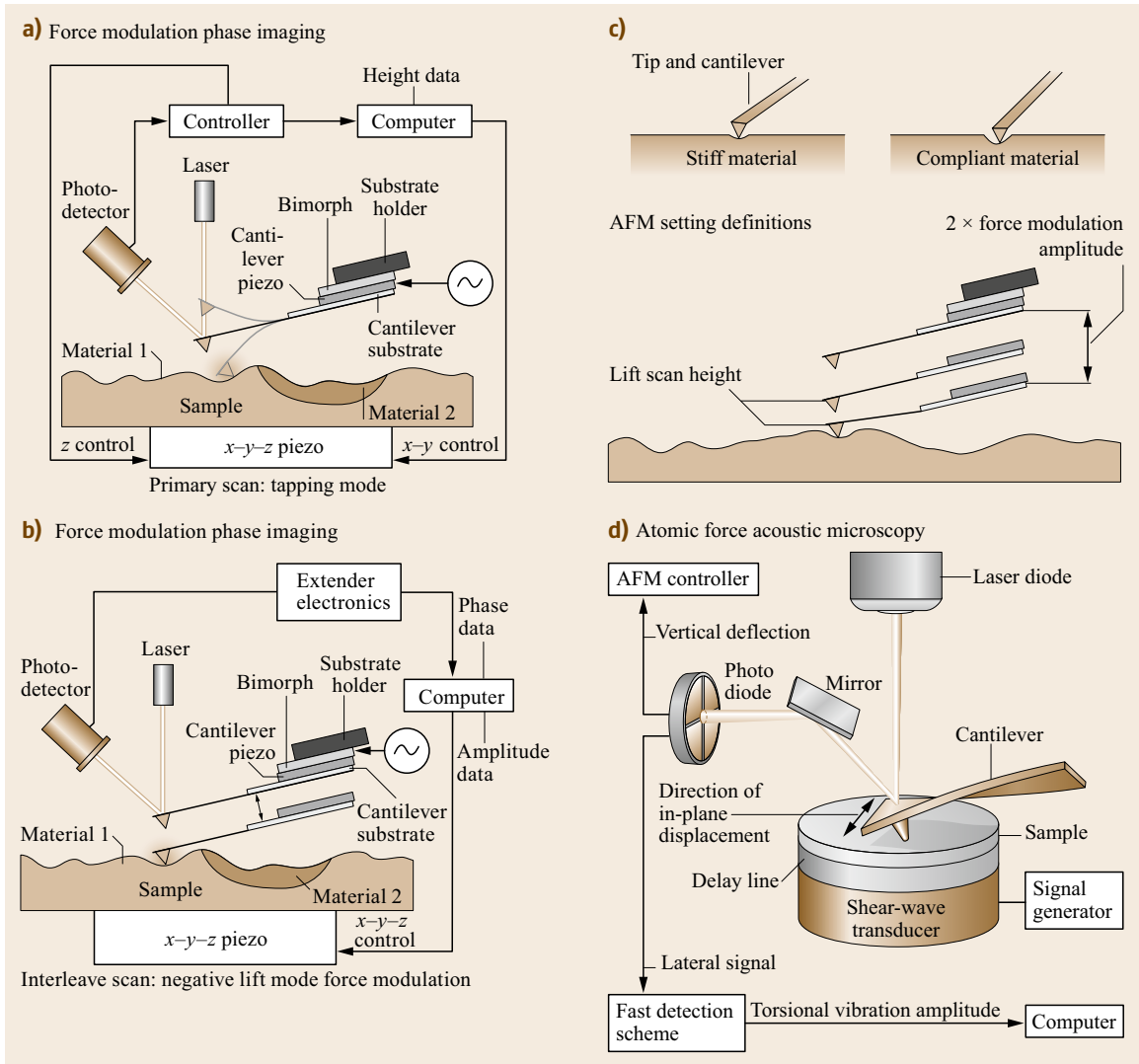
riodic force. The sample surface resists the oscillations of the tip to a greater or lesser extent depending upon the sample's stiffness. The computer records amplitude (which is a function of elastic stiffness of the material). Contact analyses can be used to obtain a quantitative measure of localized elasticity of soft surfaces [27.66]. Etched single-crystal silicon cantilevers with integrated tips (Bruker force modulation etched Si probe or FESP) with a radius of 25−50 nm, a stiffness of 1−5 N/m, and a natural frequency of 60−100 kHz, are commonly used for the measurements. Scanning is normally set to a rate of 0.5 Hz along the fast axis.

In the AFAM technique [27.68, 88, 89], the cantilever/tip assembly is moved either in the normal or lateral mode, and the contact stiffness is evaluated by comparing the resonance frequency of the cantilever in contact with the sample surface to those of the free vibrations of the cantilever. Several free resonance frequencies are measured. On the basis of the shift of the measured frequencies, the contact stiffness is determined by solving the characteristic equation for the tip vibrating in contact with the sample surface. The elastic modulus is calculated from contact stiffness using Hertz analysis for a spherical tip indenting a plane. Contact stiffness is equal to 8 × contact radius × reduced shear modulus in shear mode.

In the lateral mode using the AFAM technique, the sample is glued on cylindrical pieces of aluminum which serves as ultrasonic delay lines coupled to an ultrasonic shear wave transducer (Fig. 27.10b) [27.34, 68, 89]. The transducer is driven with frequency sweeps to generate in-plane lateral sample surface vibrations. These couple to the cantilever via the tip–sample contact. To measure torsional vibrations of the cantilever at frequencies up to 3 MHz, the original electronic circuit of the lateral channel of the AFM (using a lowpass filter with limited bandwidth to a few hundred kHz) was replaced by a high-speed scheme which bypasses the lowpass filter. The high-frequency signal was fed to a lock-in amplifier, digitized using a fast analog/digital (A/D) card, and fed into a broadband amplifier, followed by an root mean square (RMS)-to-DC converter and read by a computer. Etched single-crystal silicon cantilevers (normal stiffness of 3.8−40 N/m) with integrated tips are used.

Viscoelastic Mapping
Another form of dynamic force microscopy, phase contrast microscopy, is used to detect the contrast in viscoelastic (viscous energy dissipation) properties of different materials across the surface [27.48, 65, 69, 70, 72, 90, 91]. In these techniques, both deflection amplitude and phase angle contrasts are measured, which are measures of the relative stiffness and viscoelastic

Nanotribology, Nanomechanics and Materials Characterization | 27.1 Description of AFM/FFM and Various Measurement Techniques 879

Part F | 27.1

Fig. 27.10 (a–c) Schematic of force modulation mode used to obtain amplitude (stiffness) and definitions of force modulation amplitude and lift scan height. During primary scanning, height data is recorded in tapping mode. During interleave scanning, the entire cantilever/tip assembly is vibrated at the bimorph's resonance frequency and the z-direction feedback control for the sample x–y–z piezo is deactivated. During this scanning, height information from the primary scan is used to maintain a constant lift scan height. The computer records amplitude (which is a function of material stiffness) during the interleave scan. **(d)** Schematic of an AFM incorporating shear wave transducer which generates in-plane lateral sample surface vibrations. Because of the forces between the tip and the surface, torsional vibrations of the cantilever are excited (after [27.34]). The shift in contact resonance frequency is a measure of contact stiffness

properties, respectively. Two phase measurement techniques – tapping mode and torsional resonance (TR) mode – have been developed. We describe them next.

In the tapping mode (TM) technique, as described earlier, the cantilever/tip assembly is sinusoidally vibrated at its resonant frequency, and the sample x–y–z piezo is adjusted using feedback control in the z-direction to maintain a constant setpoint

(Fig. 27.3) [27.69, 70]. The feedback signal to the z-direction sample piezo (to keep the setpoint constant) is a measure of surface roughness. The extender electronics is used to measure the phase angle lag between the cantilever piezo drive signal and the cantilever response during sample engagement. As illustrated in Fig. 27.3, the phase angle lag (at least partially) is a function of the viscoelastic properties of the sample material.

A range of tapping amplitudes and setpoints can be used for measurements. A commercially etched single-crystal silicon tip (DI TESP), with a radius of 5−10 nm, a stiffness of 20−100 N/m, and a natural frequency of 350−400 kHz, is normally used for tapping mode. Scanning is normally set to a rate of 1 Hz along the fast axis.

In the torsional mode (TR mode), a tip is vibrated at high frequency at the resonance frequency of the cantilever beam. An etched single-crystal silicon cantilever with integrated tip (DI FESP) with a radius of about 5−10 nm, normal stiffness of 1−5 N/m, torsional stiffness of about 30 times normal stiffness, and torsional natural frequency of 800 kHz is normally used. A major difference between the TM and TR modes is the directionality of the applied oscillation – a normal (compressive) amplitude exerted for the TM and a torsional amplitude for the TR mode. The TR mode is expected to provide good contrast in the tribological and mechanical properties of the near-surface region as compared to the TM. Two of the reasons are as follows. (1) In the TM, the interaction is dominated by the vertical properties of the sample, so the tip spends a small fraction of its time in near-field interaction with the sample. Furthermore, the distance between the tip and the sample changes during the measurements, which changes interaction time and forces, and affects measured data. In the TR mode, the distance remains nearly constant. (2) The lateral stiffness of a cantilever is typically about two orders of magnitude larger than the normal (flexural) stiffness. Therefore, in the TM, if the sample is relatively rigid, much of the deformation occurs in the cantilever beam, whereas in the TR mode, much of the deformation occurs in the sample. A few comments on the special applications of the TR mode are made next. Since most of the deformation occurs in the sample, the TR mode can be used to measure stiff and hard samples. Furthermore, properties of thin films can be measured more readily with the TR mode. For both the TM and TR modes, if the cantilever is driven to vibrate at frequencies above resonance, it would have less motion (high apparent stiffness), leading to higher sample deformation and better contrast. It should be further noted that the TM exerts a compressive force, whereas the TR mode exerts torsional force, therefore normal and shear properties are measured in the TM and TR modes, respectively.

In the TR mode, the torsional vibration of the cantilever beam is achieved using a specially designed cantilever holder. It is equipped with a piezo system mounted in a cantilever holder, in which two piezos vibrate out-of-phase with respect to each other. A tuning process prior to scanning is used to select the torsional vibration frequency. The piezo system excites torsional vibration at the cantilever's resonance frequency. The torsional vibration amplitude of the tip (TR amplitude) is detected by the lateral segments of the split-diode photodetector (Fig. 27.11) [27.71]. The TR mode measures surface roughness and phase angle as follows. During the measurement, the cantilever/tip assembly is
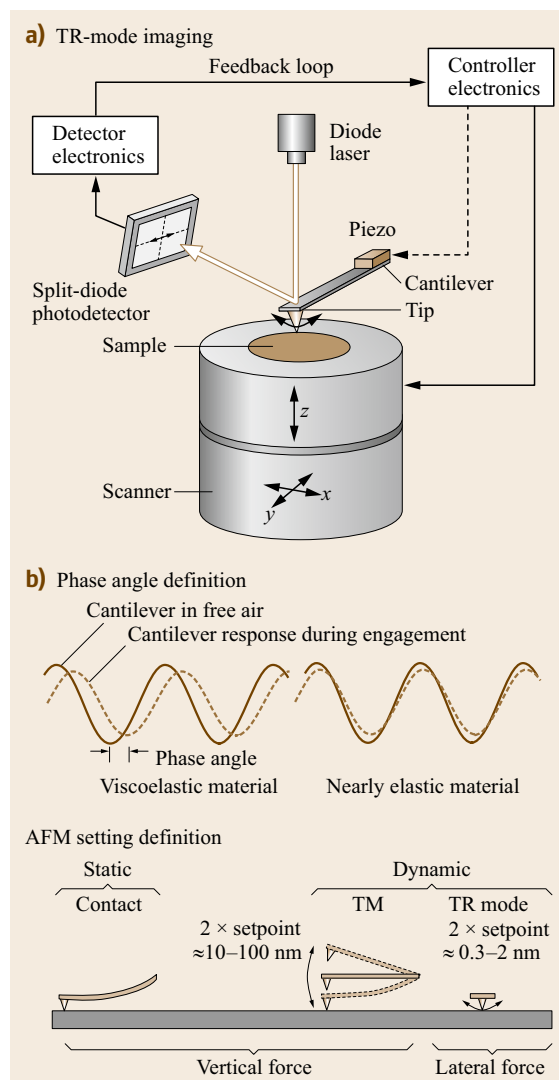
Fig. 27.11a,b Schematic of torsional resonance mode shown *at the top* (**a**). Two examples of the phase angle response are shown *in the middle* (**b**). One is for materials exhibiting viscoelastic and the other nearly elastic properties. Three AFM settings are compared *at the bottom*: contact, tapping mode (TM), and TR modes. The TR mode is a dynamic approach with a laterally vibrating cantilever tip that can interact with the surface more intensively than other modes. Therefore, more detailed near-surface information is available

Nanotribology, Nanomechanics and Materials Characterization | 27.1 Description of AFM/FFM and Various Measurement Techniques 881

Part F | 27.1

first vibrated at its resonance at some amplitude dependent upon the excitation voltage, before the tip engages the sample. Next, the tip engages the sample at some setpoint. A feedback system coupled to a piezo stage is used to keep a constant TR amplitude during scanning. This is done by controlling the vertical position of the sample using a piezo moving in the z-direction, which changes the degree of tip interaction. The displacement of the sample z piezo gives a roughness image of the sample. A phase angle image can be obtained by measuring the phase lag of the cantilever vibration response in the torsional mode during engagement with respect to the cantilever vibration response in free air before engagement. The control feedback of the TR mode is similar to that of tapping, except that the torsional resonance amplitude replaces flexural resonance amplitude [27.71].

Chen and *Bhushan* [27.72] used a variation to the approach just described (referred to as mode I here). They performed measurements at constant normal cantilever deflection (constant load; mode II) instead of using the constant setpoint in the *Kasai* et al. [27.71] approach. Their approach overcomes the meniscus adhesion problem present in mode I and reveals true surface properties.

Song and *Bhushan* [27.92] presented a forced torsional vibration model for a tip-cantilever assembly under viscoelastic tip–sample interaction. This model provides a relationship of torsional amplitude and phase shift with lateral contact stiffness and viscosity which can be used to extract in-plane interfacial mechanical properties.

Various operating modes of AFM used for surface roughness, localized surface elasticity, and viscoelastic

mapping and friction force measurements (to be discussed later) are summarized in Table 27.2.

27.1.8 Boundary Lubrication Measurements

To study nanoscale boundary lubrication properties, adhesive forces are measured in the force calibration mode, as previously described. The adhesive forces are also calculated from the horizontal intercept of friction versus normal load curves at a zero value of friction force. For friction measurements, the samples are typically scanned using an Si tip over an area of $2 \times 2\,\mu m^2$ at the normal load ranging from 5 to 130 nN. The samples are generally scanned with a scan rate of 0.5 Hz resulting in a scanning speed of $2\,\mu m/s$. Velocity effects on friction are studied by changing the scan frequency from 0.1 to 60 Hz, while the scan size is maintained at $2 \times 2\,\mu m^2$, which allows velocity to vary from 0.4 to $240\,\mu m/s$. To study the durability properties, the friction force and coefficient of friction are monitored during scanning at a normal load of 70 nN and a scanning speed of $0.8\,\mu m/s$, for a desired number of cycles [27.42, 43, 47].

27.1.9 AFM Tip Wear

AFM tips wear during use. Wear can result in an increase in tip radius and adhesion between the tip and the sample, thus reducing the image resolution and introducing artifacts. The tip geometry can be measured by AFM imaging using an ultrasharp geometry (sharper than the AFM tip), known as a tip characterizer, and analyzing the data for tip reconstruction using a tip de-

Table 27.2 Summary of various operating modes of AFM for surface roughness, stiffness, phase angle, and friction

Operating mode	Direction of cantilever vibration	Vibration frequency of cantilever (kHz)	Vibration amplitude (nm)	Feedback control	Data obtained
Contact	N/A			Constant normal load	Surface height, friction
Tapping	Vertical	350−400	10−100	Setpoint (constant tip amplitude)	Surface height, phase angle (normal viscoelasticity)
Force modulation	Vertical	10−20 (bimorph)	10−100	Constant normal load	Surface height, amplitude (normal stiffness)
Lateral	Lateral (AFAM)	100−3000 (sample)	≈ 5 (sample)	Constant normal load	Shift in contact resonance (normal stiffness, friction)
TR mode I	Torsional	≈ 800	0.3−2	Setpoint (constant tip amplitude)	Surface height, phase angle (lateral viscoelasticity)
TR mode II	Torsional	≈ 800	0.3−2	Constant normal load	Surface height, amplitude and phase angle (lateral stiffness and lateral viscoelasticity)
TR mode III	Torsional	> 800 in contact	0.3−2	Constant normal load	Shift in contact resonance (friction)

convolution algorithm [27.93]. A grating sample with an array of sharp tips with a radius less than 10 nm is commonly used.

Tao and *Bhushan* [27.93] developed fluoropolymer coatings deposited on the silicon probe to reduce their tip wear.

27.2 Surface Imaging, Friction, and Adhesion

27.2.1 Atomic–Scale Imaging and Friction

Surface height imaging down to atomic resolution of electrically conducing surfaces can be carried out using an STM. An AFM can also be used for surface height imaging and roughness characterization down to the nanoscale. Figure 27.12 shows a sequence of STM images at various scan sizes of solvent-deposited C_{60} film on 200 nm thick gold-coated freshly cleaved mica [27.94]. The film consists of clusters of C_{60} molecules 8 nm in diameter. The C_{60} molecules within a cluster appear to pack into a hexagonal array with a spacing of about 1 nm, however, they do not follow any long-range order. The measured cage diameter of the C_{60} molecule is about 0.7 nm, very close to the projected diameter of 0.71 nm.

In an AFM measurement during surface imaging, the tip comes into intimate contact with the sample surface and leads to surface deformations with finite tip–sample contact area (typically few atoms). The finite size of the contact area prevents the imaging of individual point defects, and only the periodicity of the atomic lattice can be imaged. Figure 27.13a shows the topography image of a freshly cleaved surface of highly oriented pyrolytic graphite (HOPG) [27.26]. The periodicity of the graphite is clearly observed.

To study the friction mechanisms on an atomic scale, a freshly cleaved HOPG was studied by *Mate* et al. [27.23] and *Ruan* and *Bhushan* [27.26]. Figure 27.14a shows the atomic-scale friction force map (raw data) and Fig. 27.13a shows the friction force maps (after two-dimensional (2-D) spectrum filtering with high-frequency noise truncated) [27.26]. Figure 27.14a also shows a line plot of friction force profiles along some crystallographic direction. The actual shape of the friction profile depends upon the spatial location of the axis of tip motion. Note that a portion of atomic-scale lateral force is conservative. *Mate* et al. [27.23] and *Ruan* and *Bhushan* [27.26] reported that the average friction force linearly increased with normal load and was reversible with load. Friction profiles were similar during the sliding of the tip in either direction.

During scanning, the tip moves discontinuously over the sample surface and jumps with discrete steps from one potential minimum (well) to the next. This leads to a saw-tooth-like pattern for the lateral mo-

tion (force) with a periodicity of the lattice constant. This motion is called the stick-slip movement of the tip [27.2, 23, 26]. The observed friction force includes two components – conservative and periodic, and non-
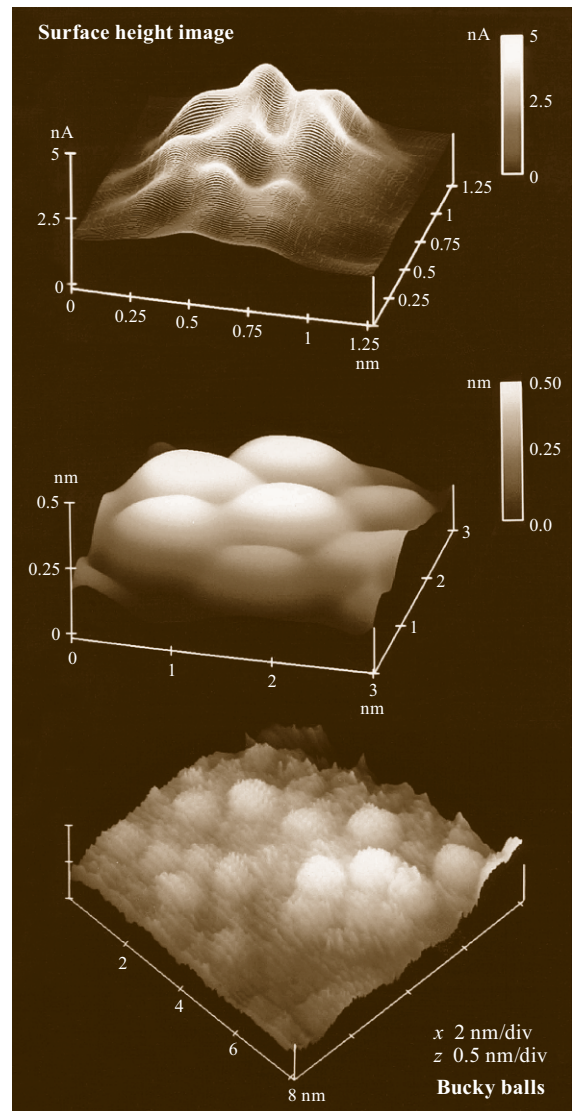
Fig. 27.12 STM images of solvent-deposited C_{60} film on a gold-coated freshly cleaved mica at various scan sizes (after [27.95])

conservative and constant. If the relative motion of the sample and tip were simply that of two rigid collections of atoms, the effective force would be a conservative force oscillating about zero. Slow reversible elastic de-
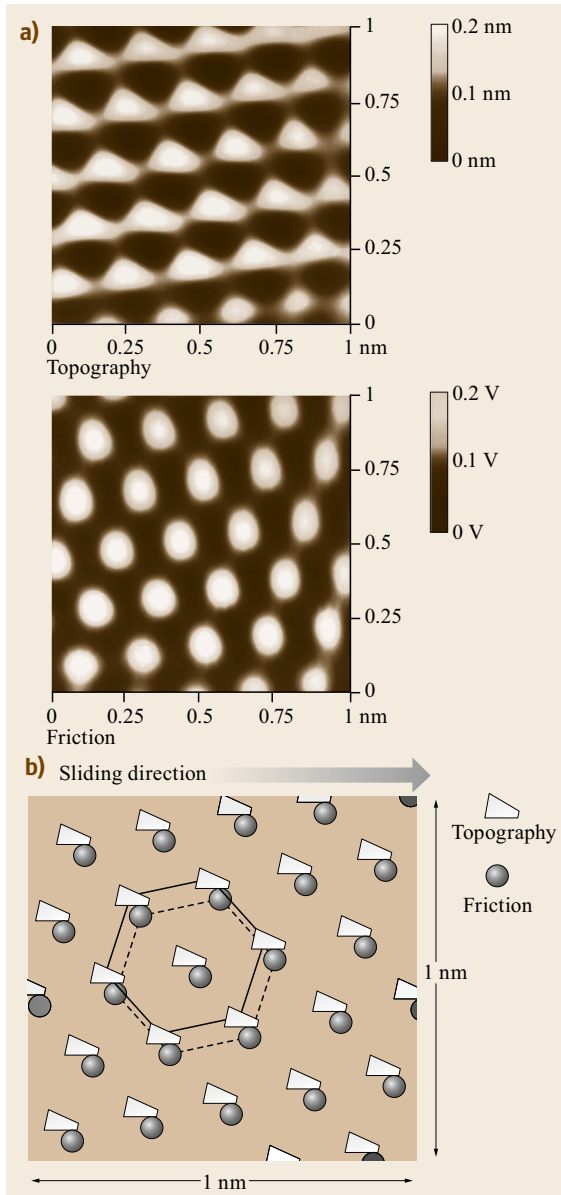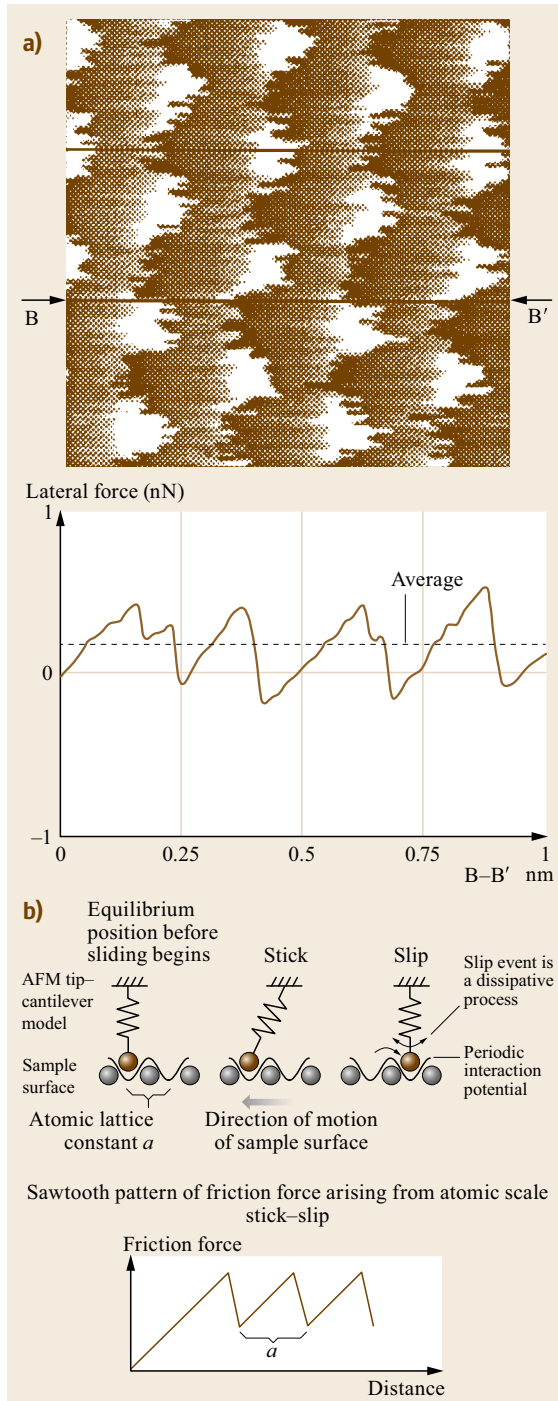

Fig. 27.13 (a) Gray-scale plots of surface topography and friction force maps (2-D spectrum filtered), measured simultaneously, of a 1 nm × 1 nm area of freshly cleaved HOPG, showing the atomic-scale variation of topography and friction, and **(b)** schematic of superimposed topography and friction maps from **(a)**; the *symbols* correspond to maxima. Note the spatial shift between the two plots (after [27.26])

formation would also contribute to conservative force. The origin of the nonconservative direction-dependent force component would be phonon generation, viscous dissipation, or plastic deformation.

Stick-slip on the atomic scale, discussed above, is the result of the energy barrier required to be overcome to jump over the atomic corrugations on the sample surface. It corresponds to the energy required for the jump of the tip from a stable equilibrium position on the surface to a neighboring position. The perfect atomic regularity of the surface guarantees the periodicity of the lateral force signal, independent of the actual atomic structure of the tip apex. A few atoms (based on the magnitude of the friction force, less than ten) on a tip sliding over an array of atoms on the sample are expected to undergo the stick-slip. For simplicity, Fig. 27.14b shows a simplified model for one atom on a tip with a one-dimensional spring mass system. As the sample surface slides against the AFM tip, the tip remains *stuck* initially until it can overcome the energy (potential) barrier, which is illustrated by a sinusoidal interaction potential as experienced by the tip. After some motion, there is enough energy stored in the spring which leads to *slip* into the neighboring stable equilibrium position. During the slip and before attaining stable equilibrium, stored energy is converted into vibrational energy of the surface atoms in the range of 10^{13} Hz (phonon generation) and decays within the range of 10^{-11} s into heat. (A wave of atoms vibrating in concert are termed a phonon). The stick-slip phenomenon, resulting from irreversible atomic jumps, can be theoretically modeled with classical mechanical models [27.96, 97]. The Tomanek-Zhong-Thomas model [27.97] is the starting point for determining friction force during atomic-scale stick-slip. The AFM model describes the total potential as the sum of the potential acting on the tip due to interaction with the sample and the elastic energy stored in the cantilever. Thermally activated stick-slip behavior can explain the velocity effects on friction, to be presented later.
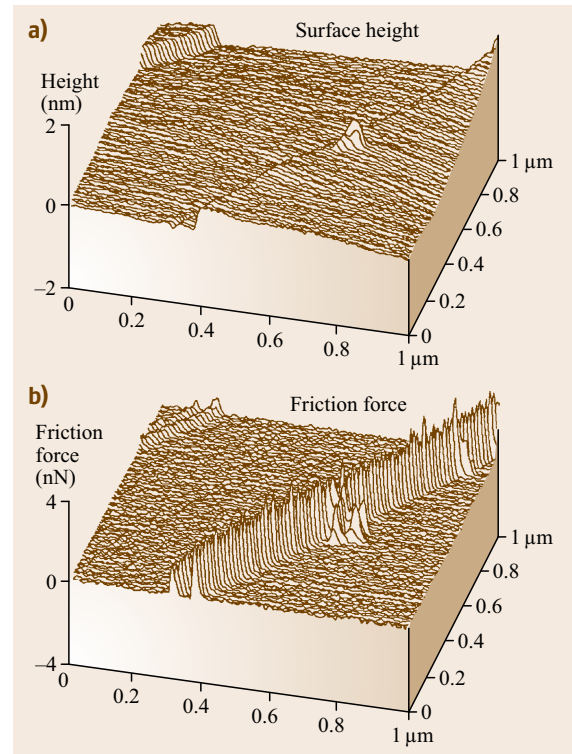
Finally, based on Fig. 27.13a, the atomic-scale friction force of HOPG exhibited the same periodicity as that of the corresponding topography, but the peaks in friction and those in the topography are displaced relative to each other (Fig. 27.13b). A Fourier expansion of the interatomic potential was used by *Ruan* and *Bhushan* [27.26] to calculate the conservative interatomic forces between the atoms of the FFM tip and those of the graphite surface. Maxima in the interatomic forces in the normal and lateral directions do not occur at the same location, which explains the observed shift between the peaks in the lateral force and those in the corresponding topography.

Fig. 27.14 **(a)** Gray-scale plot of a friction force map (raw data) of a 1×1 nm^2 area of freshly cleaved HOPG, showing atomic-scale variation of friction force. High points are shown by a *lighter color*. Also shown is a line plot of the friction force profile along the line indicated by the *arrows*. The normal load was 25 nN and the cantilever normal stiffness was 0.4 N/m (after [27.26]). **(b)** Schematic of a model for a tip atom sliding on an atomically flat periodic surface. The schematic shows the tip jumping from one potential minimum to another, resulting in stick-slip behavior ◄

Fig. 27.15 **(a)** Surface roughness and **(b)** friction force maps at a normal load of 42 nN of a freshly cleaved HOPG surface against an Si$_3$N$_4$ FFM tip. Friction in the *line-shaped region* is over an order of magnitude larger than the smooth areas (after [27.26])

27.2.2 Microscale Friction

Local variations in the microscale friction of cleaved graphite are observed (Fig. 27.15). Microscale friction is defined as the friction measured with a scan size equal to or larger than $1\,\mu m \times 1\,\mu m$. These arise from structural changes that occur during the cleaving process [27.27]. The cleaved HOPG surface is largely atomically smooth but exhibits line-shaped regions in which the coefficient of friction is more than an order of magnitude larger. Transmission electron microscopy indicates that the line-shaped regions consist of graphite planes of different orientation, as well as of amorphous carbon. Differences in friction have also been observed for multiphase ceramic materials [27.56]. Figure 27.16 shows the surface roughness and friction
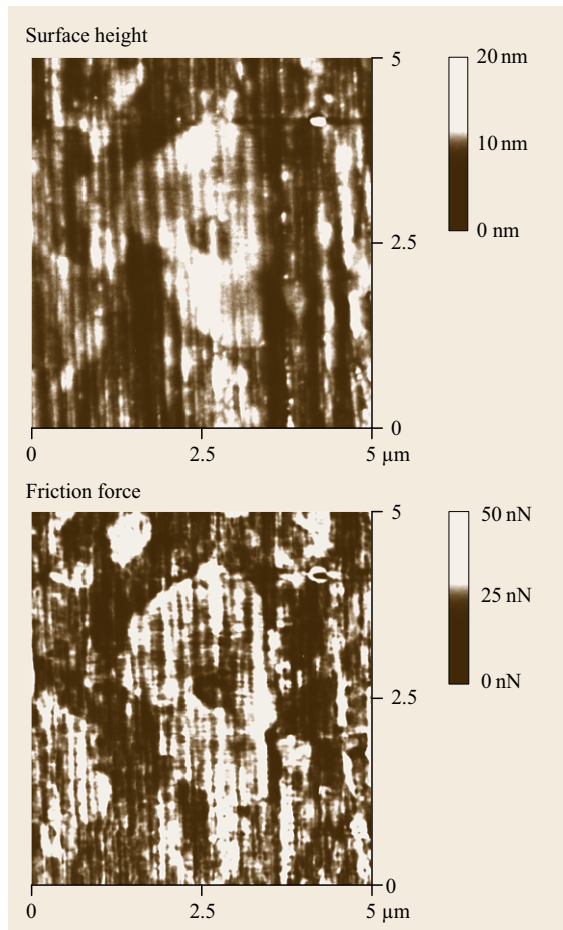
force maps of Al_2O_3-TiC (70−30 wt%). TiC grains have a Knoop hardness of about $2800\,kg/mm^2$ and Al_2O_3 has $2100\,kg/mm^2$, therefore, TiC grains do not polish as much and result in a slightly higher elevation (about 2−3 nm higher than that of Al_2O_3 grains). TiC grains exhibit higher friction force than Al_2O_3 grains. The coefficients of friction of TiC and Al_2O_3 grains are 0.034 and 0.026, respectively, and the coefficient of friction of Al_2O_3-TiC composite is 0.03. Local variation in friction force also arises from the scratches present on the Al_2O_3-TiC surface. *Meyer* et al. [27.98] also used FFM to measure structural variations of organic mono- and multilayer films. All of these measurements suggest that the FFM can be used for structural mapping of the surfaces. FFM measurements can also be used to map chemical variations, as indicated by the use of the FFM with a modified probe tip to map the

spatial arrangement of chemical functional groups in mixed organic monolayer films [27.99]. Here, sample regions that had stronger interactions with the functionalized probe tip exhibited greater friction.

Local variations in the microscale friction of nominally rough, homogeneous material surfaces can be significant, and are seen to depend on the local surface slope rather than the surface height distribution (Fig. 27.17). This dependence was first reported by

Fig. 27.16 Gray-scale surface roughness ($\sigma = 0.80\,nm$) and friction force maps (mean = 7.0 nN, $\sigma = 0.90\,nN$) for Al_2O_3-TiC (70−30 wt%) at a normal load of 138 nN (after [27.56])
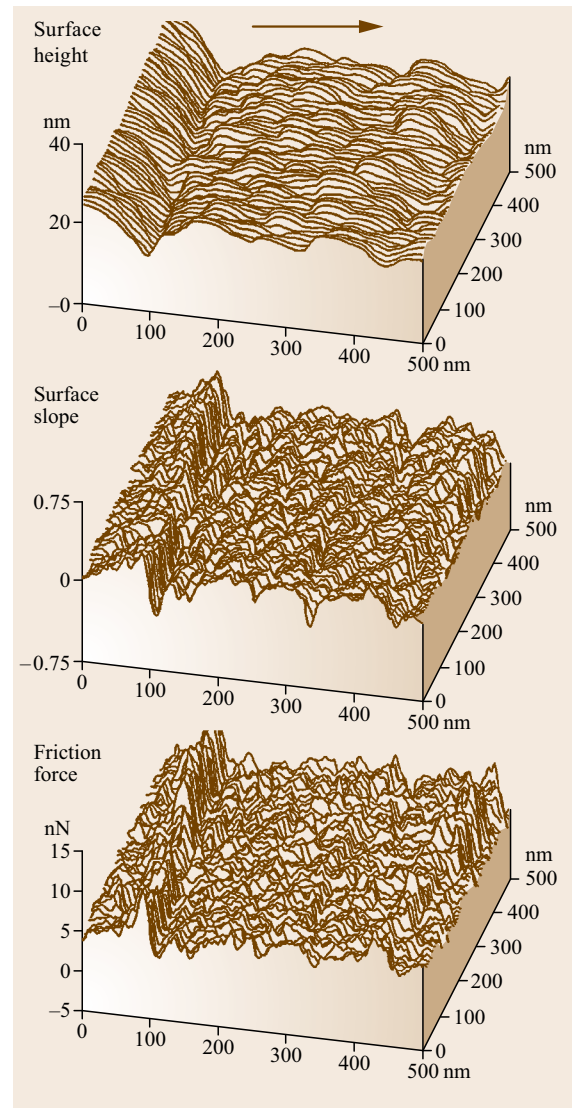
Fig. 27.17 Surface roughness map ($\sigma = 4.4\,nm$), surface slope map taken in the sample-sliding direction (the *horizontal axis*; mean = 0.023, $\sigma = 0.197$), and friction force map (mean = 6.2 nN, $\sigma = 2.1\,nN$) for a lubricated thin-film magnetic rigid disk for a normal load of 160 nN (after [27.28])

Bhushan and Ruan [27.24], Bhushan et al. [27.28] and Bhushan [27.79] and later discussed in more detail by Koinkar and Bhushan [27.100] and Sundararajan and Bhushan [27.101]. In order to elegantly show any correlation between local values of friction and surface roughness, surface roughness and friction force maps of a gold-coated ruler with somewhat rectangular grids and a silicon grid with square pits were obtained (Fig. 27.18). Figures 27.17 and 27.18 show the surface roughness map, the slopes of the roughness map taken along the sliding direction (surface slope map), and the friction force map for various samples. There is a strong correlation between the surface slopes and friction forces. For example, in Fig. 27.18, the friction force is high locally at the edge of the grids and pits with a positive slope and is low at the edges with a negative slope.

We now examine the mechanism of microscale friction, which may explain the resemblance between the slope of surface roughness maps and the corresponding friction force maps [27.2, 7, 13, 14, 24, 26–28, 101, 102]. There are three dominant mechanisms of friction; adhesive, ratchet, and plowing [27.103, 104]. As a first order, we may assume these to be additive. The adhesive mechanism cannot explain the local variation in friction. Next, we consider the ratchet mechanism. We consider a small tip sliding over an asperity making an angle θ with the horizontal plane (Fig. 27.19). The normal force W (normal to the general surface) applied by the tip to the sample surface is constant. The friction force F on the sample would be a constant for a smooth surface if the friction mechanism does not change. For the rough surface shown in Fig. 27.19, if the adhesive mechanism does not change during sliding, the local value of the coefficient of friction remains constant,

$$\mu_0 = \frac{S}{N} \, , \tag{27.1}$$

where S is the local friction force and N is the local normal force. However, the friction and normal forces are measured with respect to global horizontal and normal axes, respectively. The measured local coefficient of friction μ_1 in the ascending part is

$$\mu_1 = \frac{F}{W} = \frac{\mu_0 + \tan\theta}{1 - \mu_0\tan\theta} \approx \mu_0 + \tan\theta,$$
$$\text{for small } \mu_0\tan\theta \tag{27.2}$$

indicating that in the ascending part of the asperity one may simply add the friction force and the asperity slope to one another. Similarly, on the right-hand side (de-

scending part) of the asperity,

$$\mu_2 = \frac{\mu_0 - \tan\theta}{1 + \mu_0\tan\theta} \approx \mu_0 - \tan\theta,$$
$$\text{for small } \mu_0\tan\theta \, . \tag{27.3}$$

For a symmetrical asperity, the average coefficient of friction experienced by the FFM tip traveling across the whole asperity is

$$\mu_{\mathrm{ave}} = \frac{\mu_1 + \mu_2}{2}$$
$$= \mu_0\frac{1 + \tan^2\theta}{1 - \mu_0^2\tan^2\theta}$$
$$\approx \mu_0(1 + \tan^2\theta), \text{ for small } \mu_0\tan\theta \, . \tag{27.4}$$

Finally, we consider the plowing component of friction with the tip sliding in either direction, which is [27.14, 79]

$$\mu_{\mathrm{p}} \approx \tan\theta \, . \tag{27.5}$$

Because in FFM measurements we notice little damage of the sample surface, the contribution from plowing is expected to be small, and the ratchet mechanism is believed to be the dominant mechanism for the local variations in the friction force map. With the tip sliding over the leading (ascending) edge of an asperity, the surface slope is positive; it is negative during sliding over the trailing (descending) edge of an asperity. Thus, measured friction is high at the leading edge of asperities and low at the trailing edge. In addition to the slope effect, the collision of the tip when encountering an asperity with a positive slope produces additional torsion of the cantilever beam leading to higher measured friction force. When encountering an asperity with the same negative slope, however, there is no collision effect and hence no effect on torsion. This effect also contributes to the difference in friction forces when the tip scans up and down on the same topography feature. The ratchet mechanism and the collision effects thus semiquantitatively explain the correlation between the slopes of the roughness maps and friction force maps observed in Figs. 27.17 and 27.18. We note that in the ratchet mechanism, the FFM tip is assumed to be small compared to the size of asperities. This is valid since the typical radius of curvature of the tips is about 10−50 nm. The radii of curvature of the asperities of the samples measured here (the asperities that produce most of the friction variation) are found to typically be about 100−200 nm, which is larger than that of the FFM tip [27.105]. It is important to note that the measured local values

a)

Surface height


Surface slope

Friction force

b)
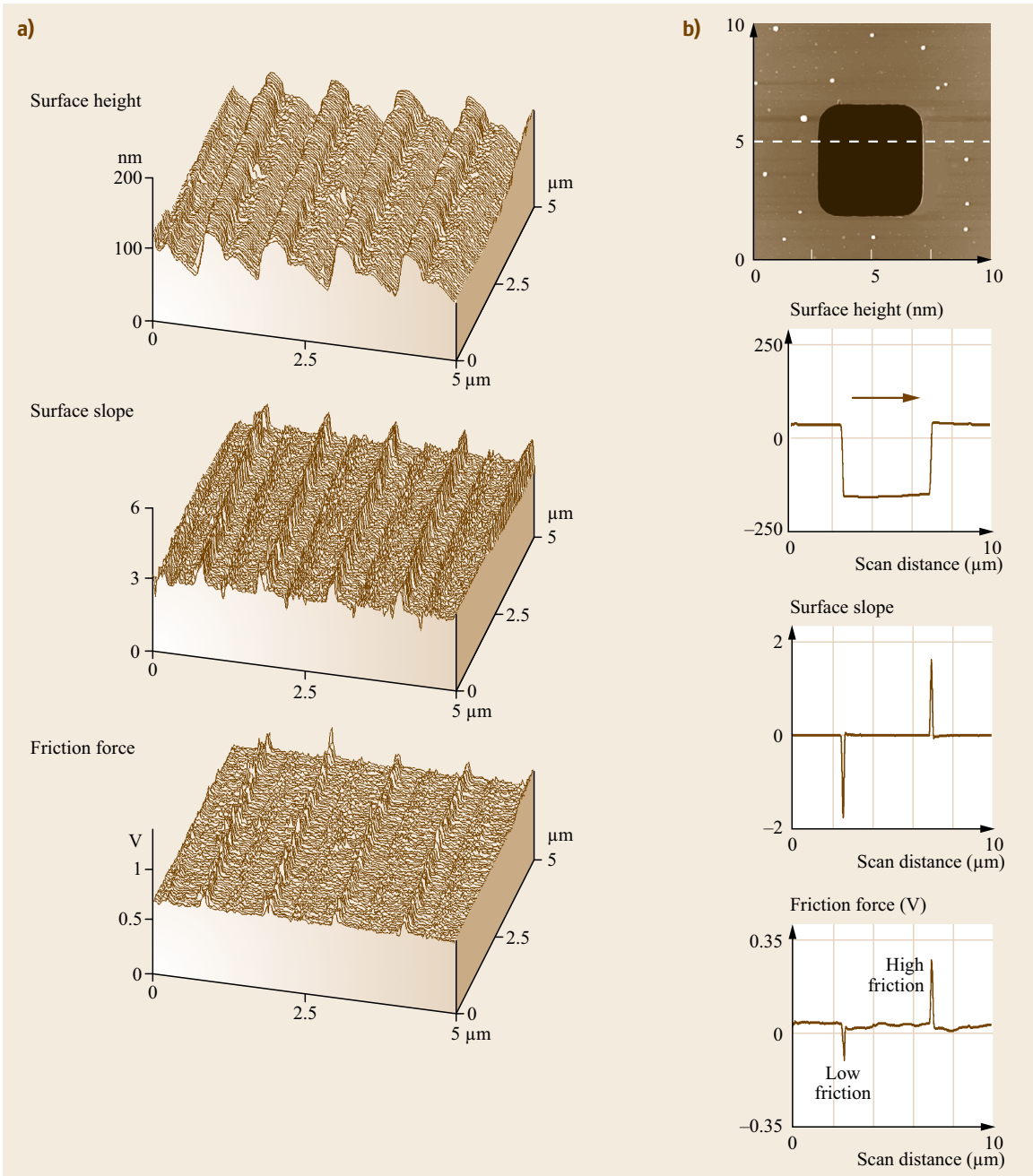
Fig. 27.18a,b Surface roughness map, surface slope map taken in the sample-sliding direction (*the horizontal axis*), and friction force map for **(a)** a gold-coated ruler (with somewhat rectangular grids with a pitch of $1\,\mu m$ and a ruling step height of about $70\,nm$) at a normal load of $25\,nN$ and **(b)** a silicon grid (with $5\,\mu m$ square pits of depth $180\,nm$ and a pitch of $10\,\mu m$) (after [27.101])

of friction and normal forces are measured with respect to global (and not local) horizontal and vertical axes, which are believed to be relevant in applications.

27.2.3 Directionality Effect on Microfriction

During friction measurements, the friction force data from both the forward (trace) and backward (re-
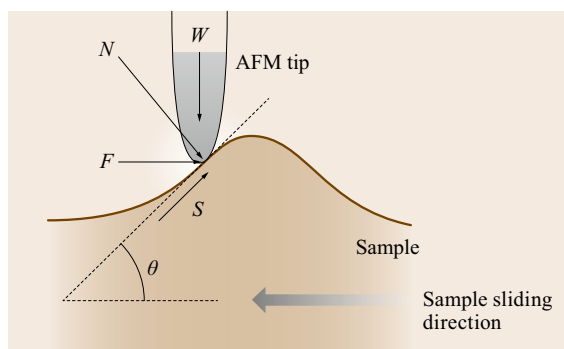
Fig. 27.19 Schematic illustration showing the effect of an asperity (making an angle θ with the horizontal plane) on the surface in contact with the tip on local friction in the presence of an adhesive friction mechanism. W and F are the normal and friction forces, respectively, and S and N are the force components along and perpendicular to the local surface of the sample at the contact point, respectively

trace) scans are useful in understanding the origins of the observed friction forces. Magnitudes of material-induced effects are independent of the scanning direction whereas topography-induced effects are different between forward and backward scanning directions. Since the sign of the friction force changes as the scanning direction is reversed (because of the reversal of torque applied to the end of the tip), addition of the friction force data of the forward and backward scan eliminates the material-induced effects while topography-induced effects still remain. Subtraction of the data between forward and backward scans does not eliminate either effect (Fig. 27.20) [27.101].

Owing to the reversal of the sign of the retrace (R) friction force with respect to the trace (T) data, the friction force variations due to topography are in the same direction (peaks in trace correspond to peaks in retrace). However, the magnitudes of the peaks in trace and retrace at a given location are different. An increase in the friction force experienced by the tip when scanning up a sharp change in topography is more than the decrease in the friction force experienced when scanning down the same topography change, partly because of collision effects discussed earlier. Asperities on engineering surfaces are asymmetrical, which also affect the magnitude of friction force in the two directions. Asymmetry in tip shape may also have an effect on the directionality effect of friction. We will note later that the magnitude of surface slopes are virtually identical, therefore, the tip shape asymmetry should not have much effect.

Figure 27.21 shows the surface height and friction force data for a gold ruler and a silicon grid in the trace and retrace directions. Subtraction of two friction data
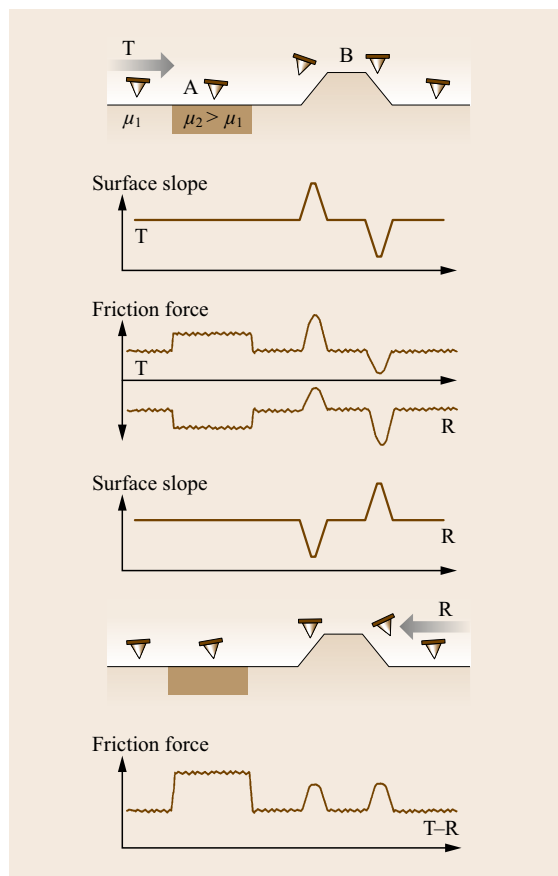
Fig. 27.20 Schematic of friction forces expected when a tip traverses a sample that is composed of different materials and sharp changes in topography. A schematic of surface slope is also shown

yields a residual peak because of the differences in the magnitudes of friction forces in the two directions. This effect is observed at all locations of significant changes in topography.

In order to facilitate comparison of the directionality effect on friction, it is important to take into account the sign change of the surface slope and friction force in the trace and retrace directions. Figure 27.22 shows surface height, surface slope, and friction force data for the two samples in the trace and retrace directions. The correlations between surface slope and friction forces are clear. The third column in the figures shows retrace slope and friction data with an inverted sign (-retrace). Now we can compare trace data with -retrace data. It is clear that the friction experienced by the tip is dependent upon the scanning direction because of surface topography. In addition to the effect of topographical changes discussed earlier, during surface-finishing processes, material can be transferred preferentially onto
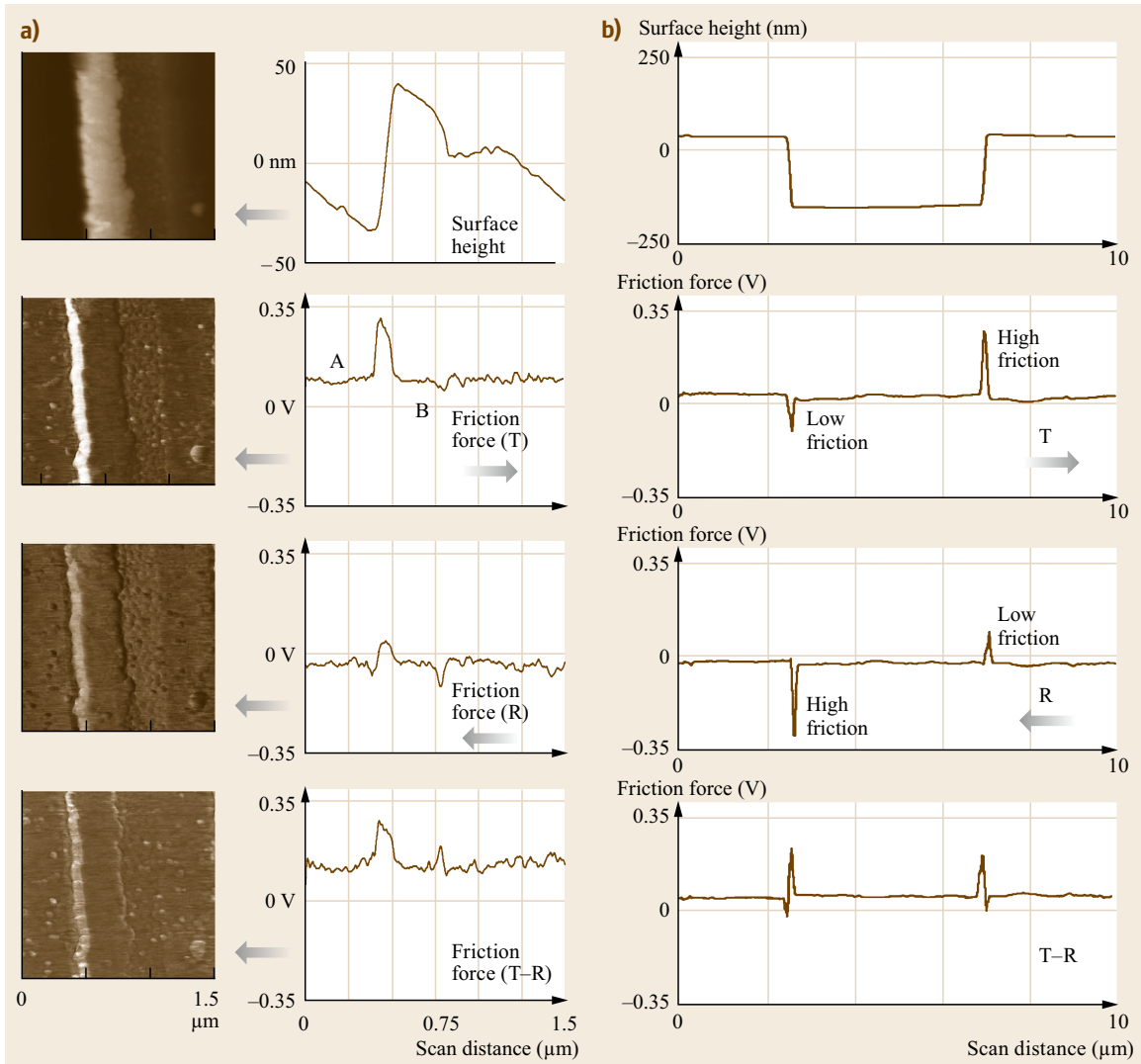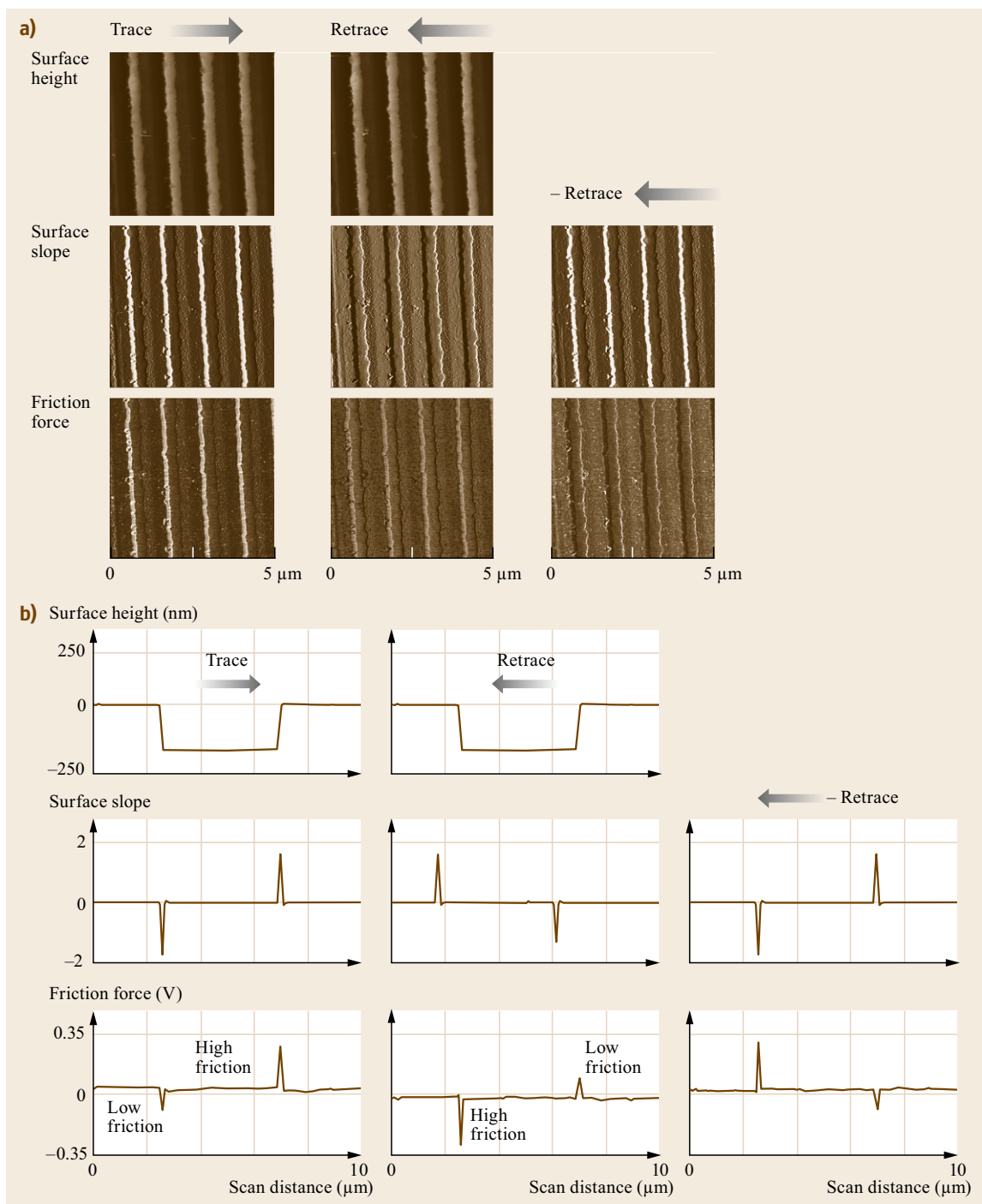
Fig. 27.21 (a) Gray-scale images and two-dimensional profiles of surface height and friction forces across a single ruling of the gold-coated ruling, and **(b)** two-dimensional profiles of surface height and friction forces across a silicon grid pit. Friction force data in trace and retrace directions, and subtracted force data are presented (after [27.101])

one side of the asperities, which also causes asymmetry and direction dependence. Reduction in local variations and in the directionality of friction properties requires careful optimization of surface roughness distributions and of surface-finishing processes.

The directionality as a result of a surface asperities effect will be also manifested in macroscopic friction data, i. e., the coefficient of friction may be different in one sliding direction than that in the other direction. The asymmetrical shape of the asperities accentuates this effect. The frictional directionality can also exist in materials with particles having a preferred orientation. The directionality effect in friction on a macroscale is observed in some magnetic tapes. In a macroscale test, a 12.7 mm wide polymeric magnetic tape was wrapped over an aluminum drum and slid in a reciprocating motion with a normal load of 0.5 N and a sliding speed of about 60 mm/s [27.79]. The coefficient of friction as a function of sliding distance in either direction is shown in Fig. 27.23. We note that the coefficient of friction on a macroscale for this tape is different in different directions. Directionality in friction is sometimes observed on the macroscale; on the microscale this is the norm [27.2, 16]. On the macroscale, the effect of surface asperities normally is averaged out over a large number of contacting asperities.

Fig. 27.22 **(a)** Gray-scale images of surface heights, surface slopes, and friction forces for scans across a gold-coated ruling, and **(b)** two-dimensional profiles of surface heights, surface slopes, and friction forces for scans across the silicon grid pit. *Arrows* indicate the tip sliding direction (after [27.101])
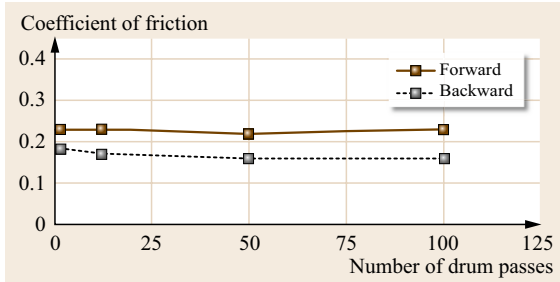
Fig. 27.23 Coefficient of macroscale friction as a function of drum passes for a polymeric magnetic tape sliding over an aluminum drum in a reciprocating mode in both directions. Normal load $= 0.5\,\mathrm{N}$ over $12.7\,\mathrm{mm}$ wide tape, sliding speed $= 60\,\mathrm{mm/s}$ (after [27.79])

27.2.4 Surface Roughness–Independent Microscale Friction

As just reported, the friction contrast in conventional friction measurements is based on interactions dependent upon interfacial material properties superimposed by roughness-induced lateral forces, and the cantilever twist is dependent on the sliding direction because of the local surface slope. Hence it is difficult to separate the friction-induced from the roughness-induced cantilever twist in the image. To obtain the roughness-independent friction, lateral or torsional modulation techniques are used in which the tip is oscillated in-plane with a small amplitude at a constant normal load, and change in shape and magnitude of cantilever resonance is used as a measure of friction force [27.4, 34–37, 106, 107]. These techniques also allow measurements over a very small area (few nm to few μm).

Scherer et al. [27.33] and *Reinstaedtler* et al. [27.34, 35] used lateral mode for friction measurements (Fig. 27.10b). *Bhushan* and *Kasai* [27.37] used the TR mode for these measurements (Fig. 27.11). Before engagement, the cantilever is driven into torsional motion of the cantilever/tip assembly with a given normal vibration amplitude (vibration amplitude in free air). After engagement, the vibration amplitude decreases due to the interaction between the tip and the sample, the vibration frequency increases, and phase shift occurs. During scanning, the normal load is kept constant, and the vibration amplitude of the cantilever is measured at the contact frequency.

As mentioned earlier, the shift in contact resonance frequency both in lateral and in TR modes is a measure of contact stiffness as shown schematically in Fig. 27.24. At an excitation voltage above a certain value, as a result of microslip at the interface, a flattening of the resonance frequency spectra occurs
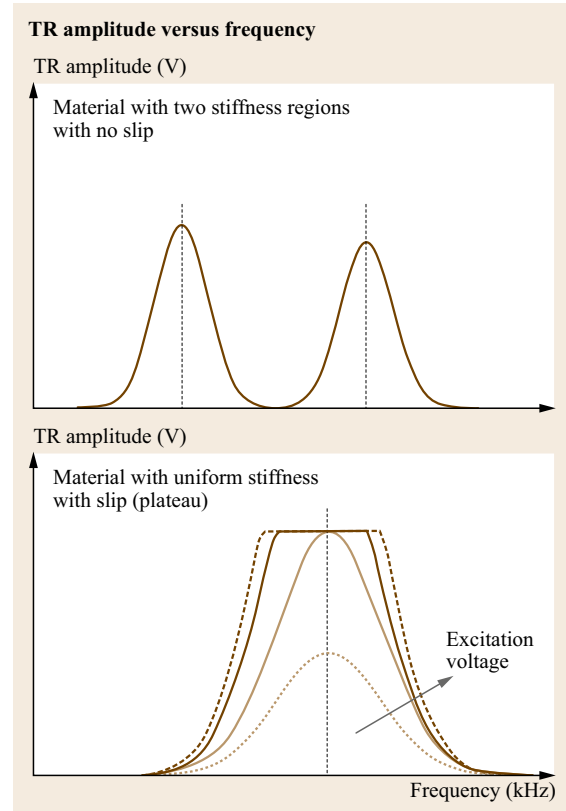
Fig. 27.24 Schematic showing frequency profiles of the TR amplitude for materials with two phases and a single phase. The maximum TR amplitude at the contact resonance frequency of the resonance curve with a flattened top, resulting from slip, can be used for friction force measurement

(Fig. 27.22). At lowest excitation voltage, the AFM tip sticks to the sample surface and follows the motion like an elastic contact with viscous damping, and the resonance curve is Lorentzian with a well-defined maximum. The excitation voltage should be high enough to initiate microslip. The maximum torsional amplitude at a given resonance frequency is a function of friction force and sample stiffness, so the technique is not valid for inhomogeneous samples. If the torsional stiffness of the cantilever is very high compared to the sample stiffness, the technique should work.

Reinstaedtler et al. [27.34] performed lateral mode experiments on bare Si and Si lubricated with 5 nm thick chemically bonded perfluoropolyether (Z-DOL) lubricant film. Figure 27.25a shows the amplitude of the cantilever torsional vibration as a function of frequency on a bare silicon sample. The frequency sweep was adjusted such that a contact resonance frequency was covered. The different curves correspond to dif-
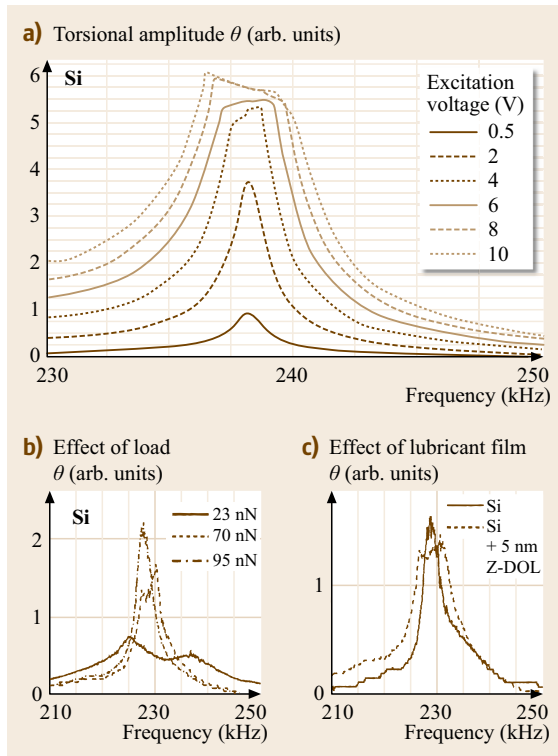
Fig. 27.25a–c Torsional vibration amplitude of the cantilever as a function of excitation frequency. (**a**) Measurement on bare silicon. The *different curves* correspond to increasing excitation voltages applied to the transducer and, hence, increasing surface amplitudes. (**b**) Measurement on silicon lubricated with a 5 nm thick Z-DOL layer. *Curves* for three different static loads are shown. The transducer was excited with 5 V of amplitude. (**c**) Measurement with a static load of 70 nN and 7 V excitation amplitude. The *two curves* correspond to bare silicon and lubricated silicon, respectively (after [27.34])

ferent excitation voltages applied to the shear wave transducer. At low amplitudes, the shape of the resonance curve is Lorentzian. Above a critical excitation amplitude of the transducer (excitation voltage $= 4\,\mathrm{V}$ corresponding to $\approx 0.2\,\mathrm{nm}$ lateral surface amplitude as measured by interferometry), the resonance curve flattens out, and the frequency span of the flattened part increases further with the excitation amplitude. Here, the static force applied was $47\,\mathrm{nN}$ and the adhesion force was $15\,\mathrm{nN}$. The resonance behavior of the tip-cantilever system in contact with the lubricated silicon sample (Fig. 27.25b) was similar to that of the bare silicon sample. By increasing the static load, the critical amplitude for the appearance of the flattening increases. The deviations from the Lorentzian resonance curve became visible at static loads lower

than 95 nN. As shown in Fig. 27.25c, the resonance curve obtained at the same normal load of 70 nN and at the same excitation voltage (7 V) is more flattened on the lubricated sample than on the bare silicon which led us to conclude that the critical amplitude is lower on the lubricated sample than on the bare sample. These experiments clearly demonstrate that torsional vibration of an AFM cantilever at ultrasonic frequencies leads to stick-slip phenomena and sliding friction. Above a critical vibration amplitude, sliding friction sets in.

Bhushan and *Kasai* [27.37] performed friction measurements on a silicon ruler and demonstrated that friction data in TR mode is essentially independent of surface-roughness and sliding direction. Figure 27.26 shows surface height and friction force maps on a silicon ruler obtained using the TR mode and contact mode techniques. A comparison is made between the TR mode and contact mode friction force maps. For easy comparison, the line scan profiles near the central area are shown on top of the gray-scale maps. The vertical scales of the friction force profiles in the two graphs are selected to cover the same range of friction force so that direct comparison can be made, i. e., 0.25 V in full scale for the TR mode corresponds to 0.5 V for the contact mode in these measurements. As expected, for the trace scan, small downward peaks in the TR mode map and large upward and downward peaks in the contact mode map are observed. The positions of these peaks coincide with those of the surface slope. Therefore, the peaks in the friction signals are attributed to a topography-induced effect. For the retrace scan, the peak pattern for the TR mode remains similar, but for the contact mode, the pattern becomes reversed.

The subtraction image for the TR mode shows almost flat contrast, since the trace and retrace friction data profiles are almost identical. For the contact mode, the subtraction image shows that the topography-induced contribution still exists. As stated earlier, the addition image of the TR mode and the addition image of the contact mode enhance the topography-induced effect, which is observed in the figure.

A closer look at the silicon ruler images at one pitch was taken, and the associated images are shown in Fig. 27.27. The surface height profiles in the TR mode and contact mode are somewhat different. The TR mode shows sharper edges than those in contact mode. The ratios of the change in amplitude at the steps to the change in the mean amplitude in the TR mode and in the contact mode are a measure of topography effects. The ratio in the contact mode ($\approx 85\%$) is about seven times larger than that of the TR mode ($\approx 12\%$).
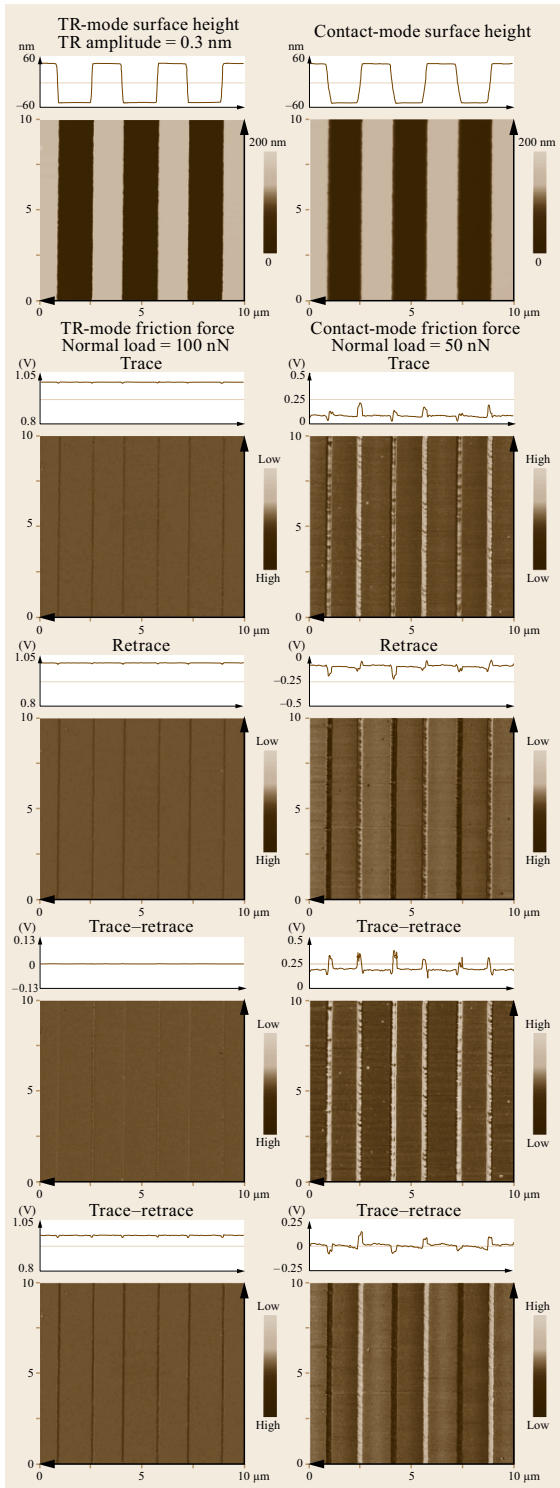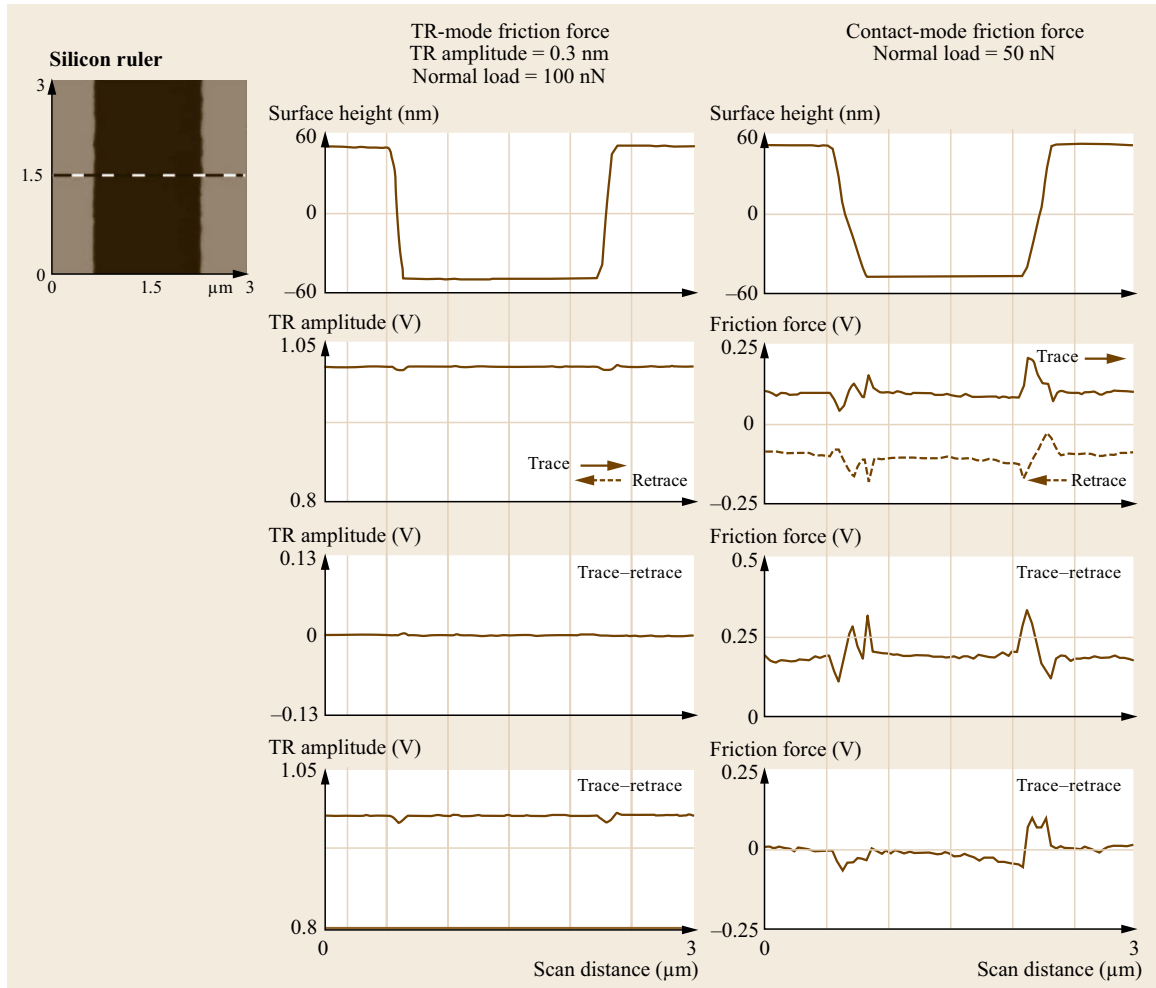
Fig. 27.26 A comparison between TR mode friction and contact mode friction maps together with line scans, on the silicon ruler. The TR mode surface height and contact mode surface height images are also shown (after [27.37])

27.2.5 Velocity Dependence on Micro/Nanoscale Friction

AFM/FFM experiments can be generally conducted at relative velocities as high as about $100-250\,\mu m/s$. To simulate applications, it is of interest to conduct friction experiments at higher velocities (up to 1 m/s). Furthermore, high-velocity experiments would be useful to study velocity dependence on friction and wear. One approach has been to mount samples on a shear wave transducer (ultrasonic transducer) and then drive it at very high frequencies (in the MHz range) as reported earlier (Fig. 27.10) [27.32–36, 106, 108]. The coefficient of friction on the nanoscale is estimated based on the contact resonance frequency and requires the solution of the characteristic equations for the tip vibrating in contact with the sample surface. The approach is complex and is dependent upon various assumptions.

An alternative approach is to utilize piezo stages with large amplitude ($\approx 10-100\,\mu m$) and relatively low resonance frequency (few kHz) and directly measure the friction force on microscale using the FFM signal without any analysis with assumptions used in the previous approaches using shear wave transducers. The commercial AFM setup modified with this approach can yield sliding velocities up to 200 mm/s [27.38, 109]. In the high-velocity piezo stage shown in Fig. 27.28b, the single axis piezo stage is oriented such that the scanning axis is perpendicular to the long axis of the AFM cantilever (which corresponds to the $90\,°C$ scan angle mode of the commercial AFM). The displacement is monitored using an integrated capacitive feedback sensor, located diametrically opposite to the piezo crystal. The capacitive change, corresponding to the stage displacement, gives a measure of the amount of displacement and can be used as feedback to the piezo controller for better guiding and tracking accuracy during scanning. The closed loop position control of the piezoelectric driven stages using capacitive feedback sensors provides linearity of motion better than 0.01% with nanometer resolution and a stable drift-free motion [27.38]. In the ultrahigh-velocity piezo stage shown in Fig. 27.28a, a rectangular monolithic piezoceramic plate (the stator) with two excitation electrodes is resonated using a 12 V power supply. Depending on the desired direction of the motion, the left or right electrode is excited to produce high-frequency eigenmode oscillations up to 200 kHz. Simultaneous eigenmodes result in quasielliptical motion. An alumina friction tip (pusher) attached to the plate pushes a slider with a glued friction bar which rests on a set of bearings. Through its contact with the friction bar, the piezoceramic plate provides microimpulses and drives the slider forward or backward.

Fig. 27.27 A comparison of the line scans of TR mode friction and contact mode friction on a selected pitch of the silicon ruler (after [27.37])

While the longitudinal oscillation component provides energy as the driving force, the transverse component serves to change the pressure of the friction tip against the friction bar. The transverse oscillation energy determines the maximum frictional force and hence the holding and driving force of the stage. An optical position reference photosensor is located approximately in the middle of the travel range and is used to reference the absolute position of the stage within $1\,\mu m$ repeatability. During motion, the increments of the linear scale from a home (reference) position point are converted to determine the position using a linear optical encoder.

The block diagram of the high-speed data collection and processing system used for the friction force measurement is shown in Fig. 27.28c. During the experiments, the AFM cantilever is held stationary by maintaining a scan size of zero. The mounted sample is scanned below the AFM tip by moving stages, and the normal and torsional deflections of the tip are recorded by a photodiode detector. The raw deflection signals from the optical detection system are directly routed to a high speed data acquisition A/D board. Raw friction data is acquired at a high sampling rate up to 80 kilosample/s.

Velocity dependence on friction for Si(100), diamond-like carbon (DLC), self-assembled monolayer, and perfluoropolyether lubricant films were studied by *Tambe* and *Bhushan* [27.38, 110–113] and *Tao* and *Bhushan* [27.109, 114]. The friction force as a function of velocity for Si(100) and DLC (deposited by filtered cathodic arc) is shown in Fig. 27.29 on a logarithm velocity scale (middle column). The solid lines in the figure represent the results for a scan length of $1000\,\mu m$

with velocity ranging from 1000 to $2 \times 10^5 \, \mu\text{m/s}$ using the ultrahigh-velocity stage. The dotted lines represent results for a $25 \, \mu\text{m}$ scan length with velocity ranging from 5 to $500 \, \mu\text{m/s}$ using the high-velocity stage. To clearly show the friction force dependence on velocity in the lower range, the test results with velocity varying from 5 to $500 \, \mu\text{m/s}$ for $25 \, \mu\text{m}$ are shown on a magnified scale in the left column of Fig. 27.29.

For the Si(100) sample, the friction force decreased with velocity at low velocities ($v < 10 \, \mu\text{m/s}$) and then increased linearly with $\log(v)$ for a $25 \, \mu\text{m}$ scan length. For the $1000 \, \mu\text{m}$ scan length, the friction force increased linearly with $\log(v)$ when velocity was lower than $2 \times 10^4 \, \mu\text{m/s}$. When velocities were higher than $2 \times 10^4 \, \mu\text{m/s}$, the friction force increased linearly with velocity. For DLC, the friction force increased linearly with $\log(v)$ from 5 to $500 \, \mu\text{m/s}$ for the $25 \, \mu\text{m}$ scan length. For the $1000 \, \mu\text{m}$ scan length, the friction force increases with velocity until about $2 \times 10^4 \, \mu\text{m/s}$ where the friction force reaches a maximum, then the friction force decreased with velocity.

For different samples, the change in the friction force with velocity involves different mechanisms in relation to sample surface conditions. The silicon surface is hydrophilic, while the DLC surface is nearly hydrophobic. Under the ambient condition, a thin layer of water film is condensed on a hydrophilic sample surface. On a hydrophobic surface with high contact angle, the water film would be difficult to form on the sample surface, and the effect of the water film on the adhesive force and friction force could be neglected.

On the silicon surface, when the velocity is lower than $10 \, \mu\text{m/s}$, the friction force decreased with velocity. This can be explained as follows. The water meniscus bridges develop as a function of time around the tip until reaching the equilibrium condition and are the dominant contributor to the friction force [27.2, 14, 103, 104]. The motion of the tip results in continuous breaking and reforming of the meniscus bridges. As the tip sliding velocity exceeds a critical velocity ($10 \, \mu\text{m/s}$), the menisci cannot reform due to insufficient time, and the meniscus force no longer plays a dominant role. Between 10 and $2 \times 10^4 \, \mu\text{m/s}$, the friction increases linearly with $\log(v)$ for both 25 and $1000 \, \mu\text{m}$ scan lengths. This logarithmic dependence can be explained by the atomic-scale stick-slip phenomenon [27.111, 114]. At a velocity larger than $2 \times 10^4 \, \mu\text{m/s}$, the friction increases linearly with velocity, and this trend can be explained by viscous shear; see the friction force plotted as a function of velocity on a linear scale at a magnified scale in the right column of Fig. 27.29.

To explain the atomic-scale stick-slip mechanism of friction, the motion for the tip is expressed by a spring
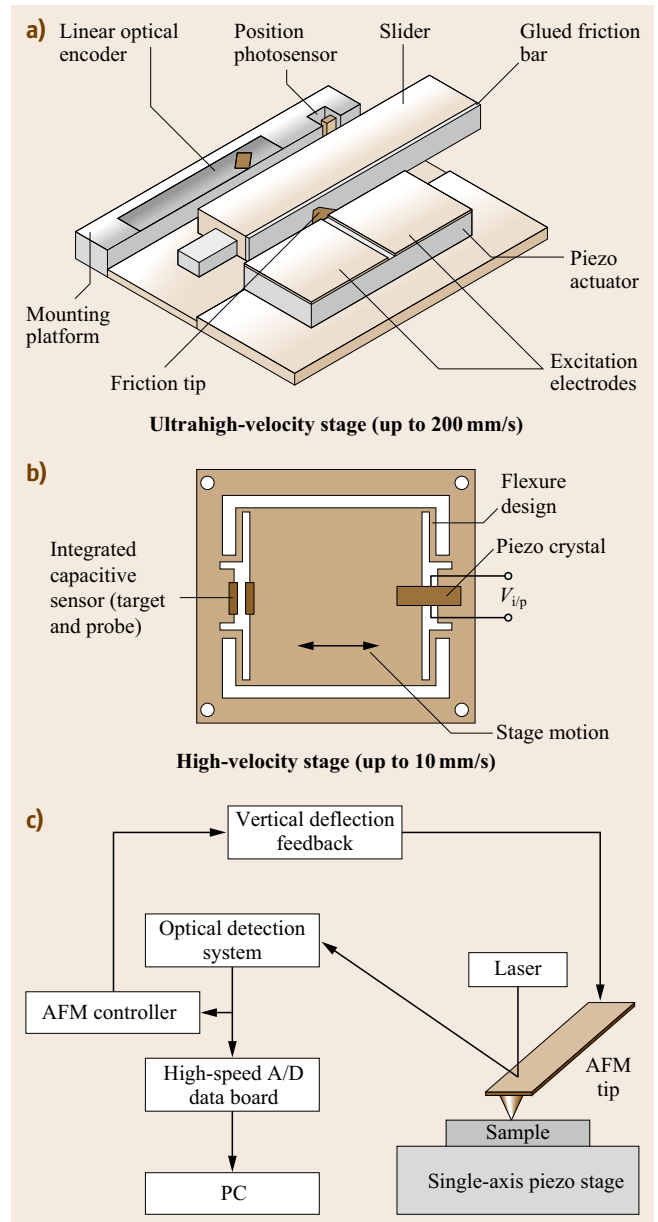

Fig. 27.28a−c Schematics of (**a**) an ultrahigh-velocity piezo stage, (**b**) high-velocity piezo stage, and (**c**) a block diagram of the high-speed data collection and processing system used for friction force measurement (after [27.38, 109])

mass model [27.115] as follows

$$m\ddot{x}_t = -\eta \dot{x}_t - k(x_\text{M} - x_\text{t}) - F, \tag{27.6}$$

where m is the effective mass of the system, η the viscous damping coefficient, k the spring constant of the cantilever, $x_\text{M} = v_\text{M}t$ the equilibrium position of the
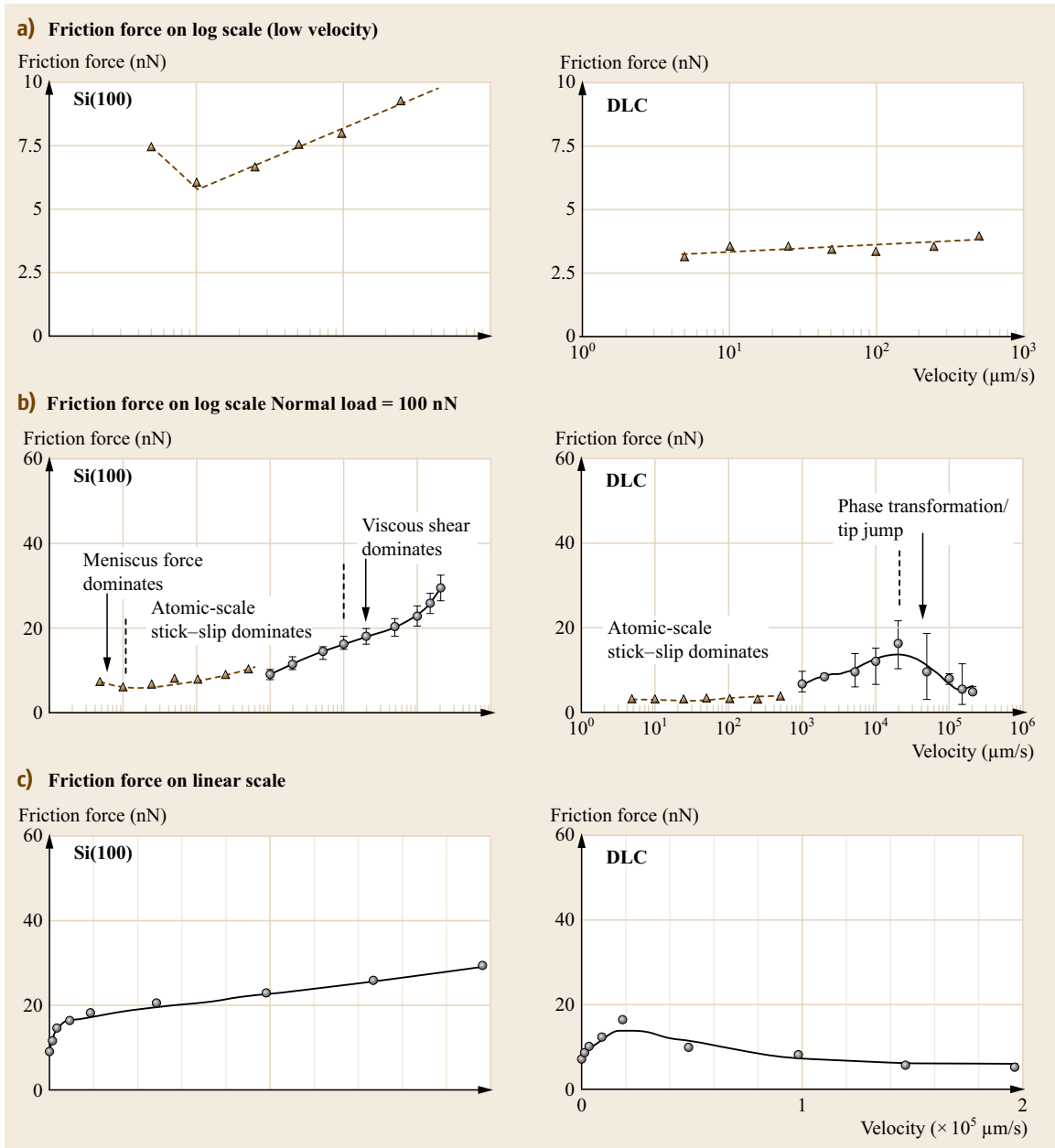
Fig. 27.29a–c Friction force as a function of sliding velocity obtained for a 25 μm scan length using a high-velocity stage (*dotted line*) and a 1000 μm scan length using an ultrahigh-velocity stage (*solid line*). In the *top two rows* (**a,b**), velocity is plotted on a log scale. (**a**) shows a lower velocity range – between 1 and 500 μm/s. (**c**) shows the data at a higher range of velocity on the linear scale (after [27.114])

cantilever, x_t the position of the tip, and F the external force. The lateral force is expressed as $F_l = k(x_M - x_t)$, and the friction force F_{fric} is the lateral force averaged over time.

For velocities lower than 2×10^4 μm/s, the damping part ($\eta \dot{x}_t$) in (27.6) is comparatively low, and atomic-

scale stick-slip dominates. To investigate the stick-slip, *Tomlinson* [27.96] assumed a periodic surface with potential

$$V(x) = V_0 \left[1 - \cos\left(\frac{2\pi x}{a} \right) \right] , \tag{27.7}$$

where V_0 is surface barrier potential height, and a is the lattice constant of the surface. Then the force (F) in (27.6) is expressed as

$$F = V'(x) = \frac{2\pi V_0}{a} \sin\left(\frac{2\pi x}{a}\right) . \qquad (27.8)$$

On the basis of the Tomlinson model, and taking into account the effect of thermal activation, or the elastic energy stored in the cantilever during sliding, *Gnecco* et al. [27.116] derived the relationship between the friction force and velocity, which is expressed as

$$F_{\text{stick-slip}} = F_0 + c \ln v , \qquad (27.9)$$

where F_0 and c are constants.

When the tip slides on a solid surface covered by a viscous film such as a water film at high velocities, the friction force (F_{fric}) is related to the velocity and viscosity of the film given by [27.103, 104]

$$F_{\text{fric}} = \mu N + \eta \dot{\gamma} A \approx \mu N + \frac{\eta v A}{d} , \qquad (27.10)$$

where μ is the coefficient of friction between the dry sliding bodies, N is the applied load, τ is the shear stress, A is the real contact area, η is the viscosity of the film, $\dot{\gamma}$ is the velocity gradient, v is the sliding velocity, and d is the thickness of the film. From (27.10), the relationship between the friction force and the sliding velocity is linear when sliding on a viscous coating. The relationship is consistent with the conclusion by *Helman* et al. [27.117] about the linear relationship between the friction force and the sliding velocity ($F_{\text{fric}} \approx \eta v_M$) at high sliding velocities for a spring mass model in (27.6) which simulates the AFM tip sliding on a viscous liquid.

The sliding of the tip on a hydrophilic surface with water films at low velocities, middle velocities, and high velocities is schematically illustrated in Fig. 27.30a [27.114]. It should be noted that the stick-slip mechanism considered by *Gnecco* et al. [27.116] was based on investigations on a dry surface. In this study, although the water was condensed on the Si(100) surface, the water film on the surface would not have significant effect on the energy dissipation due to the surface variation at relatively low velocities. Thus, the linear relationship between friction and $\log(v)$ could be maintained. When the velocity increases above a certain value, the tip would lose direct contact with the sample surface and shear the water film. At velocities higher than $2 \times 10^4 \,\mu\text{m/s}$, the asperity deformation from the high velocity impact could be another mechanism as proposed by *Tambe* and *Bhushan* [27.111].
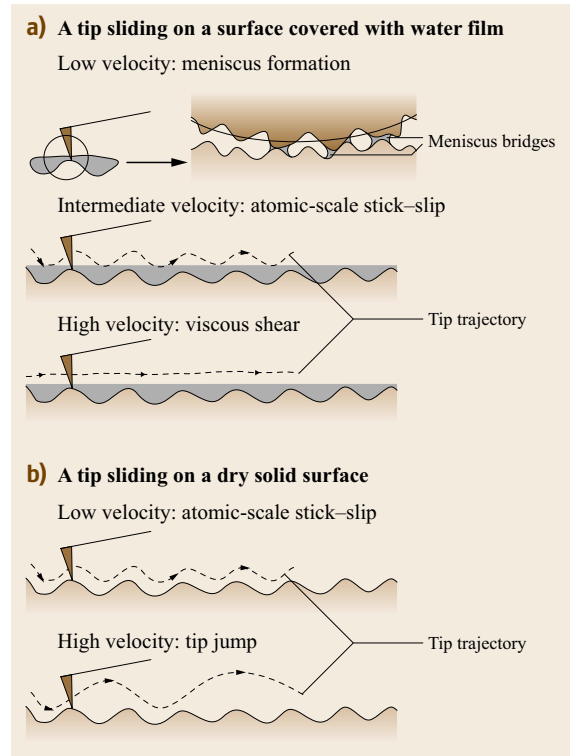
Fig. 27.30a,b Schematics of a tip sliding at different velocities on (a) a water-covered surface, and (b) a dry surface (after [27.114])

For the DLC film, since the surface is nearly hydrophobic, a uniform water film would not form on the surface. When sliding at a velocity lower than $1000 \,\mu\text{m/s}$, the friction force increased linearly with $\log(v)$, which could also be explained by atomic-scale stick-slip. At velocities higher than $1000 \,\mu\text{m/s}$, the friction force increased with velocity until the local maximum at the velocity of $2 \times 10^4 \,\mu\text{m/s}$, then decreased with velocity. The decreasing trend in friction at higher velocities could be due to tip jump during sliding. The tip jump is illustrated in Fig. 27.30b. The tip jump results in the reduction of lateral force during sliding. Variation of the friction force with distance, indicative of the tip jump, was observed from the lateral force signal (not shown). When damping is low and velocity is high, the tip could jump several periodical cycles or several peaks [27.118]. At a given low damping coefficient, the slip results in a low transient lateral force, as discussed by *Fusco* and *Fasolino* [27.118]. Thus, the average lateral force (friction force) over the scan length is low. The tip jump could also cause high velocity impact of asperities on the DLC surface, resulting in the phase transformation of DLC from sp^3 to sp^2, as explained by *Tambe* and *Bhushan* [27.111]. The

sp^2-phase layer can act as a lubricant and reduce the interfacial friction.

27.2.6 Nanoscale Friction and Wear Mapping

Contrary to the classical friction laws postulated by Amontons and Coulomb centuries ago, a nanoscale friction force is found to be strongly dependent on the normal load and sliding velocity. Many materials, coatings, and lubricants that have wide applications show reversals in friction behavior corresponding to transitions between different friction mechanisms [27.14, 38, 110, 111, 119]. Most of the analytical models developed to explain nanoscale friction behavior have remained limited in their focus and have left investigators at a loss when trying to explain friction behavior scaling multiple regimes. Nanoscale friction maps provide fundamental insights into friction behavior. They help identify and classify the dominant friction mechanisms, as well as determine the critical operating parameters that influence transitions between different mechanisms [27.111, 112]. Figure 27.31 shows a nanoscale friction map for DLC with the friction mapped as a function of the normal load and the sliding velocity [27.120]. The contours represent constant friction force lines. The friction force is seen to increase with the normal load as well as velocity. The increase in friction force with velocity is the result of atomic-scale stick-slip. This is a result of thermal activation of the irreversible jumps of the AFM tip that arise from overcoming of the energy barrier between the adjacent atomic positions, as described earlier. The concentric contour lines corresponding to the constant friction

Fig. 27.31 Contour map showing friction force dependence on normal load and sliding velocity for DLC (after [27.97])

force predicts a peak point, a point where the friction force reaches maxima and beyond which point any further increase in the normal load or the sliding velocity results in a decrease in friction force. This characteristic behavior for DLC is the result of phase transformation of DLC into a graphite-like phase by sp^3 to sp^2 phase transition, as described earlier. During the AFM experiments, the Si_3N_4 tip gives rise to contact pressures in the range of $1.8-4.4\,GPa$ for DLC for normal loads of $10-150\,nN$ [27.121]. A combination of the high contact pressures that are encountered on the nanoscale and the high frictional energy dissipation arising from the asperity impacts at the tip–sample interface due to the high sliding velocities accelerates a phase transition process whereby a low shear strength graphite-like layer is formed at the sliding interface.

Similar to friction mapping, one way of exploring the broader wear patterns is to construct wear mechanism maps that summarize data and models for wear, thereby showing mechanisms for any given set of conditions to be identified [27.119, 122–124]. Wear of sliding surfaces can occur through one or more wear mechanisms, including adhesive, abrasive, fatigue, impact, corrosive, and fretting [27.103, 104]. *Tambe* and *Bhushan* [27.121, 124] performed AFM experiments to develop nanoscale wear maps. Figure 27.32 shows a nanowear map generated for a DLC sample by simultaneously varying the normal load and the sliding velocity over the entire scan area. The wear map was generated for a normal load range of $0-1000\,nN$ and sliding velocity range of $0-2.5\,mm/s$. Wear debris, believed to result from phase transformation of DLC by sp^3 to sp^2 phase transition, was seen to form only for a high value of sliding velocities times normal loads, i.e., only beyond a certain threshold of friction energy dissipation [27.121, 124]. Hence the wear region exhibits a transition line indicating that for low velocities and low normal loads there is no phase transformation. For clarity, the wear mark corners are indicated by white dots in the AFM image (top) and the two zones of interest over the entire wear mark are schematically illustrated in Fig. 27.32 (top).

Nanoscale friction and wear mapping are novel techniques for investigating friction and wear behavior on the nanoscale over a range of operating parameters. By simultaneously varying the sliding velocity and normal load over a large range of values, nanoscale friction and wear behavior can be mapped, and the transitions between different wear mechanisms can be investigated. These maps help identify and demarcate critical operating parameters for different wear mechanisms and are very important tools in the process of design and selection of materials/coatings.
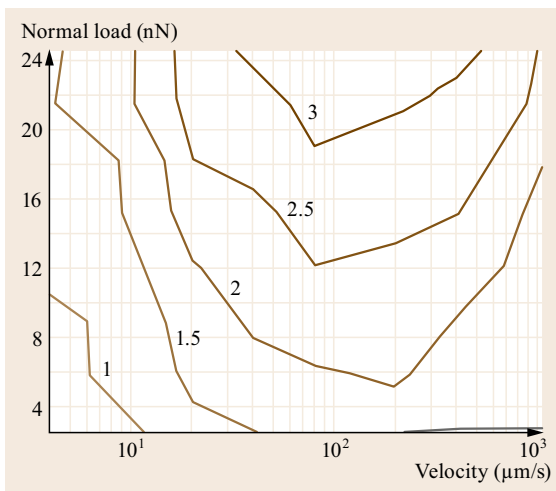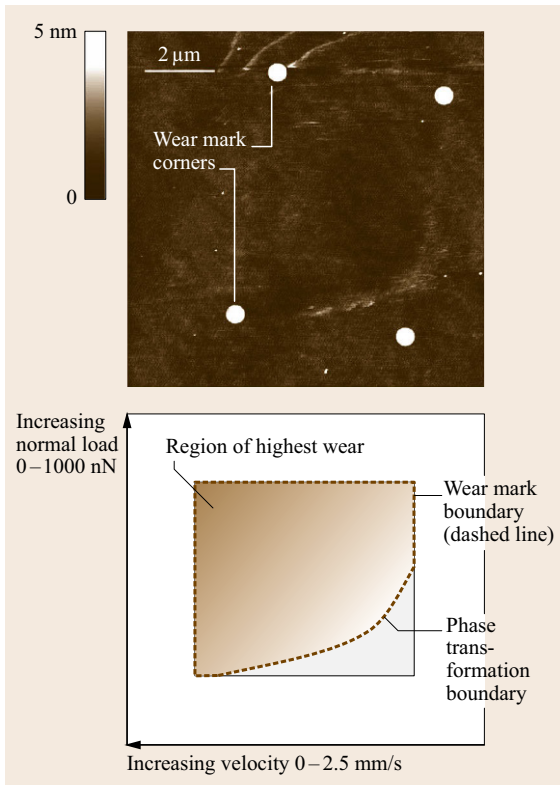
Fig. 27.32 Nanowear map (AFM image and schematic) illustrating the effect of sliding velocity and normal load on the wear of DLC resulting from phase transformation. The *curved area* shows debris lining and is indicative of the minimum frictional energy needed for phase transformation. For clarity, the wear mark corners are indicated by *white dots* in the AFM image and the various zones of interest over the entire wear mark are schematically illustrated (after [27.124])

27.2.7 Adhesion and Friction in Wet Environments

Experimental Observations

Relative humidity affects adhesion and friction for dry and lubricated surfaces [27.19, 31, 125]. Figure 27.33 shows the variation of single point adhesive force measurements as a function of tip radius on an Si(100) sample for several humidities. The adhesive force data are also plotted as a function of relative humidity for several tip radii. The general trend at humidities up to the ambient is that a 50 nm radius Si_3N_4 tip exhibits a lower adhesive force as compared to the other microtips of larger radii. However, in the latter case, values are similar. Thus, for the microtips there is no appreciable variation in adhesive force with tip radius at a given humidity up to the ambient. The adhesive

force increases as relative humidity increases for all tips.

The sources of adhesive force between a tip and a sample surface are van der Waals attraction and meniscus formation [27.19, 103, 104]. The relative magnitudes of the forces from the two sources are dependent upon various factors including the distance between the tip and the sample surface, their surface roughness, their hydrophobicity, and the relative humidity [27.126]. For most rough surfaces, the meniscus contribution dominates at moderate to high humidities which arise from the capillary condensation of water vapor from the environment. If enough liquid is present to form a meniscus bridge, the meniscus force should increase with an increase in tip radius (proportional to tip radius for a spherical tip). In addition, an increase in the tip radius results in an increased contact area leading to higher values of van der Waals forces. However, if nanoasperities on the tip and the sample are considered then the number of contacting and near-contacting asperities forming meniscus bridges increases with an increase of humidity leading to an increase in meniscus forces. These explain the trends observed in Fig. 27.33. From the data, the tip radius has little effect on the adhesive forces at low humidities but increases with tip radius at high humidity. Adhesive force also increases with an increase in humidity for all tips. This observation suggests that thickness of the liquid film at low humidities is insufficient to form continuous meniscus bridges to affect adhesive forces in the case of all tips.

Figure 27.33 also shows the variation in the coefficient of friction as a function of the tip radius at a given humidity, and as a function of the relative humidity for a given tip radius for Si(100). It can be observed that for 0% RH (relative humidity), the coefficient of friction is about the same for the tip radii except for the largest tip, which shows a higher value. At all other humidities, the trend consistently shows that the coefficient of friction increases with the tip radius. An increase in friction with tip radius at low to moderate humidities arises from the increased contact area (due to higher van der Waals forces) and higher values of the shear forces required for a larger contact area. At high humidities, similar to adhesive force data, an increase with tip radius occurs because of both contact area and meniscus effects. Although the AFM/FFM measurements are able to measure the combined effect of the contribution of van der Waals and meniscus forces towards the friction force or adhesive force, it is difficult to measure their individual contributions separately. It can be seen that for all tips, the coefficient of friction increases with humidity to about ambient, beyond which it starts to decrease. The initial increase in the coefficient of friction with humidity arises from the fact that the thickness of
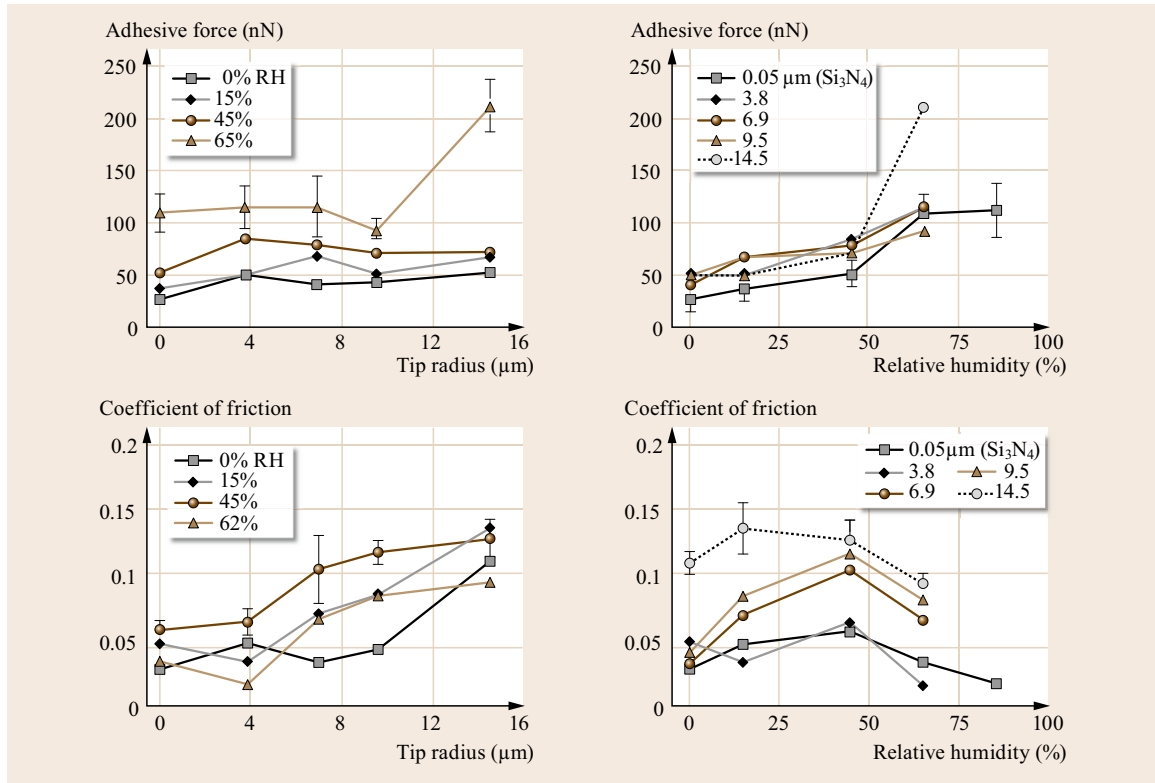
Fig. 27.33 Adhesive force and coefficient of friction as a function of tip radius at several humidities and as a function of relative humidity at several tip radii on Si(100) (after [27.31])

the water film increases with an increase in the humidity, which results in a larger number of nanoasperities forming meniscus bridges and leads to higher friction (larger shear force). The same trend is expected with the microtips beyond 65% RH. This is attributed to the fact that at higher humidities, the adsorbed water film on the surface acts as a lubricant between the two surfaces. Thus, the interface is changed at higher humidities, resulting in lower shear strength and hence lower friction force and coefficient of friction.

Adhesion and Friction Force Expressions for a Single-Asperity Contact

We now obtain the expressions for the adhesive force and coefficient of friction for a single-asperity contact with a meniscus formed at the interface (Fig. 27.34). For a spherical asperity of radius R in contact with a flat and smooth surface with the composite modulus of elasticity E^* and in the presence of liquid with a concave meniscus, the attractive meniscus force (adhesive force), designated as F_m or W_{ad}, is given as [27.19, 103, 104]

$$W_{ad} = 2\pi R\gamma(\cos\theta_1 + \cos\theta_2), \qquad (27.11)$$

where γ is the surface tension of the liquid, and θ_1 and θ_2 are the contact angles of the liquid with surfaces 1 and 2, respectively. For an elastic contact for both extrinsic (W) and intrinsic (W_{ad}) normal load, the friction force is given as,

$$F_e = \pi\tau\left[\frac{3(W + W_{ad})R}{4E^*}\right]^{2/3}, \qquad (27.12)$$

where W is the external load, and τ is the average shear strength of the contacts. (The surface energy effects are not considered here.) Note that adhesive force increases linearly with an increase in the tip radius, and the friction force increases with an increase in the tip radius as $R^{2/3}$ and with normal load as $(W + W_{ad})^{2/3}$. The experimental data in support of $W^{2/3}$ dependence on the friction force can be found in various references [27.67]. The coefficient of friction μ_e is obtained from (27.12) as

$$\mu_e = \frac{F_e}{(W + W_{ad})} = \pi\tau\left(\frac{3R}{4E^*}\right)^{2/3}\frac{1}{(W + W_{ad})^{1/3}}. \qquad (27.13)$$
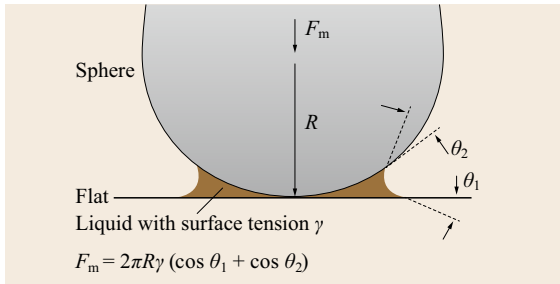
Fig. 27.34 Meniscus formation from a liquid condensate at the interface for a sphere in contact with a plane surface

In the plastic contact regime [27.103, 104], the coefficient of friction μ_p is obtained as

$$\mu_p = \frac{F_p}{W + W_{ad}} = \frac{\tau}{H_s} , \qquad (27.14)$$

where H_s is the hardness of the softer material. Note that in the plastic contact regime, the coefficient of friction is independent of external load, adhesive contributions, and surface geometry.

For comparisons, for multiple-asperity contacts in the elastic contact regime the total adhesive force W_{ad} is the summation of adhesive forces at n individual contacts,

$$W_{ad} = \sum_{i=1}^{n} (W_{ad})_i \qquad (27.15)$$

and

$$\mu_e \approx \frac{3.2\tau}{E^*(\sigma_p/R_p)^{1/2} + (W_{ad}/W)} ,$$

where σ_p and R_p are the standard deviation of summit heights and average summit radius, respectively. Note that the coefficient of friction depends upon the surface roughness. In the plastic contact regime, the expression for μ_p in (27.14) does not change.

The source of the adhesive force in a wet contact in the AFM experiments being performed in an ambient environment includes mainly attractive meniscus force due to capillary condensation of water vapor from the environment. The meniscus force for a single contact increases with an increase in the tip radius. A sharp AFM tip in contact with a smooth surface at low loads (on the order of a few nN) for most materials can be simulated as a single-asperity contact. At higher loads, for rough and soft surfaces, multiple contacts would occur. Furthermore, at low loads (nN range) for most materials, the local deformation would be primarily elastic. Assuming that the shear strength of

contacts does not change, the adhesive force for smooth and hard surfaces at low normal load (on the order of a few nN) (for a single-asperity contact in the elastic contact regime) would increase with an increase in tip radius, and the coefficient of friction would decrease with an increase in total normal load as $(W + W_{ad})^{-1/3}$ and would increase with an increase of tip radius as $R^{2/3}$. In this case, Amontons' law of friction which states that the coefficient of friction is independent of the normal load and is independent of the apparent area of contact does not hold. For a single-asperity plastic contact and multiple-asperity plastic contacts, neither the normal load nor tip radius comes into play in the calculation of the coefficient of friction. In the case of multiple-asperity contacts, the number of contacts increase with an increase of normal load, therefore the adhesive force increases with an increase in load.

In the data presented earlier in this section, the effect of tip radius and humidity on the adhesive forces and the coefficient of friction is investigated for experiments with the Si(100) surface at loads in the range of $10-100$ nN. The multiple-asperity elastic-contact regime is relevant for this study involving large tip radii. An increase in humidity generally results in an increase in the number of meniscus bridges, which would increase the adhesive force. As was suggested earlier, that increase in humidity also may decrease the shear strength of contacts. A combination of an increase in adhesive force and a decrease in shear strength would affect the coefficient of friction. An increase in the tip radius would increase the meniscus force (adhesive force). A substantial increase in the tip radius may also increase interatomic forces. These effects influence the coefficient of friction with an increase in the tip radius.

27.2.8 Separation Distance Dependence of Meniscus and van der Waals Forces

When two surfaces are in close proximity, sources of adhesive forces are weak van der Waals attraction and meniscus formation. Relative magnitudes of the forces from the two sources are dependent upon various factors including the interplanar separation, their surface roughness, their hydrophobicity, and relative humidity (liquid volume) [27.126]. Meniscus contribution dominates at moderate to high humidities, and van der Waals forces dominate at asperities a few nm apart. In some micro/nanocomponents, it is important to know the relative contribution of two sources as a function of given interplanar separation so as to design an interface for low adhesion. For example, if two ultrasmooth surfaces come in close proximity with interplanar separation on

the order of a nm, van der Waals forces may dominate, and their magnitude may be reduced by creating bumps on one of the interfaces. This analysis is also of interest in AFM studies to understand distance dependence of adhesive forces as the tip goes in and out of contact.

Stifter et al. [27.126] modeled the contact of a parabolic-shaped tip and a flat, smooth sample surface. The tip may represent a surface asperity on an interface or an AFM tip in an AFM experiment. They calculated van der Waals and meniscus forces as a function of different parameters, namely, tip geometry, tip–sample starting distance, relative humidity, surface tension, and contact angles. They compared the meniscus forces with van der Waals forces to understand their relative importance in various operating conditions.

The interacting force between tip and sample in dry conditions is the Lennard-Jones force derived from the Lennard-Jones potential. The Lennard-Jones potential is composed of two interactions – the van der Waals attraction and the Pauli repulsion. Van der Waals forces are significant because they are always present. For a parabolic tip above a half-plane with a distance D between tip and plane, the Lennard-Jones potential is obtained by integrating the atomic potential over the volume of the tip and sample. It is given as [27.126]

$$V(D) = \frac{c}{12}\left(-\frac{A}{D} + \frac{B}{210 D^7}\right), \qquad (27.16)$$

where c is the width of the parabolic tip ($=$ diameter in the case of a spherical tip), and A and B are two potential parameters, where A is the Hamaker constant. This equation provides expressions for attractive and repulsive parts. The calculations were made for Lennard-Jones force (total) and van der Waals force (attractive part) for two Hamaker constants: 0.04×10^{-19} J (representative of polymers) and 3×10^{-19} J (representative of ceramics), and meniscus force for a water film ($\gamma_\ell = 72.5$ N/m). Figure 27.35 shows various forces as a function of separation distance. The effect of two relative humidities and three tip radii was also studied as to their effect on meniscus forces. The two dashed curves indicate the spread of possible van der Waals forces for two Hamaker constants. The figure shows that meniscus forces exhibit weaker distance dependence. The meniscus forces can be stronger or weaker than van der Waals forces for distances smaller than about 0.5 nm. For longer distances, the meniscus forces are stronger than the van der Waals forces. Van der Waals forces must be considered for a tip–sample distance up to a few nm ($D < 5$ nm). The meniscus forces operate up to the break of the meniscus in the range from 5 to 20 nm [27.126].
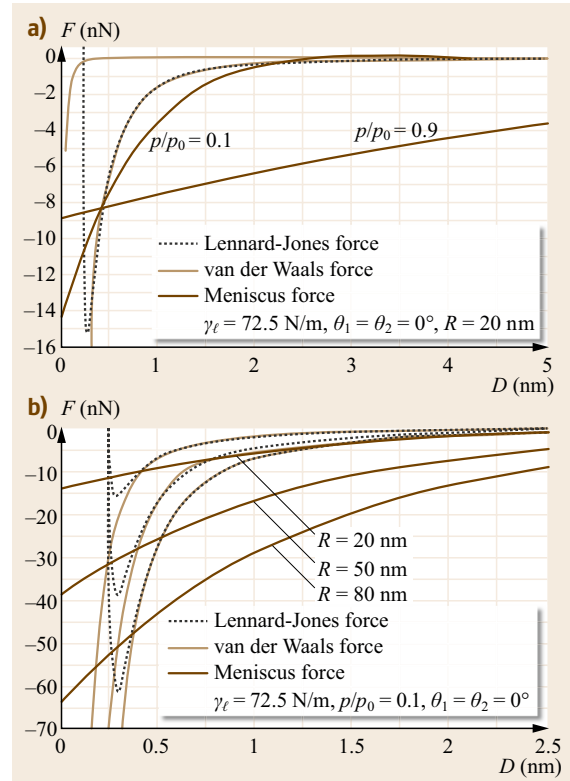
Fig. 27.35a,b Relative contribution of meniscus, van der Waals and Lennard-Jones forces (F) as a function of separation distance (D) and at **(a)** two values of relative humidity (p/p_o) for tip radius of 20 nm and Hamaker constants of 0.04×10^{-19} and 3.0×10^{-19} J, and **(b)** three tip radii (R) and a Hamaker constant of 3.0×10^{-19} J (after [27.126])

27.2.9 Scale Dependence in Friction

Table 27.3 presents the adhesive force and the coefficient of friction data obtained on the nanoscale and microscale [27.25, 110, 127, 128]. Adhesive force and coefficient of friction values on the nanoscale are about half to one order of magnitude lower than that on the microscale. Scale dependence is clearly observed in this data. As a further evidence of scale dependence, Table 27.4 shows the coefficient of friction measured for Si(100), HOPG, natural diamond, and DLC on the nanoscale and microscales. It is clearly observed that friction values are scale-dependent.

To estimate the scale length, the apparent contact radius at test loads is calculated and presented in Table 27.3. Mean apparent pressures are also calculated and presented. For nanoscale AFM experiments, it is assumed that an AFM tip coming in contact with a flat surface represents a single-asperity and elastic contact,

Table 27.3 Micro- and nanoscale values of adhesive force and coefficient of friction in micro- and nanoscale measurements (after [27.127])

Sample	Adhesive force		Coefficient of friction	
	Microscale[a] (μN)	Nanoscale[b] (nN)	Microscale[a]	Nanoscale[b]
Si(100)	685	52	0.47	0.06
DLC	325	44	0.19	0.03
Z-DOL	315	35	0.23	0.04
HDT	180	14	0.15	0.006

[a] Versus 500 μm radius Si(100) ball.
[b] Versus 50 nm radius Si_3N_4 tip.

Table 27.4 Micro- and nanoscale values of the coefficient of friction, typical physical properties of specimen, and calculated apparent contact radii and apparent contact pressures at loads used in micro- and nanoscale measurements. For calculation purposes it is assumed that contacts on micro- and nanoscale are single-asperity elastic contacts (after [27.134])

Sample	Coefficient of friction		Elastic modulus (GPa)	Poisson's ratio	Hardness (GPa)	Apparent contact radius at test load for		Mean apparent pressure at test load for	
	microscale	nanoscale				microscale (μm) (upper limit)	nanoscale (nm)	microscale (GPa) (lower limit)	nanoscale (GPa)
Si(100) wafer	0.47[a]	0.06[c]	130[e,f]	0.28[f]	9−10[e,f]	0.8−2.2[a]	1.6−3.4[c]	0.05−0.13[a]	1.3−2.8[c]
Graphite (HOPG)	0.1[b]	0.006[c]	9−15[g] (9)	– (0.25)	0.01[j]	62[b]	3.4−7.4[c]	0.082[b]	0.27−0.58[c]
Natural diamond	0.2[b]	0.05[c]	1140[h]	0.07[h]	80−104[g,h]	21[b]	1.1−2.5[c]	0.74[b]	2.5−5.3[c]
DLC film	0.19[a]	0.03[d]	280[i]	0.25[i]	20−30[i]	0.7−2.0[a]	1.3−2.9[d]	0.06−0.16[a]	1.8−3.8[d]

[a] 500 μm radius Si(100) ball at 100−2000 μN and 720 μm/s in dry air, *Bhushan* et al. [27.127]
[b] 3 mm radius Si_3N_4 ball (elastic modulus 310 GPa, Poisson's ratio 0.22 (*Bhushan* and *Gupta* [27.129])), at 1 N and 800 μm/s, *Ruan* and *Bhushan* [27.25]
[c] 50 nm radius Si_3N_4 tip at load range from 10−100 nN and 0.5 nm/s in dry air, *Ruan* and *Bhushan* [27.25]
[d] 50 nm radius Si_3N_4 tip at load range from 10−100 nN in dry air, *Bhushan* et al. [27.127]
[e] *Bhushan* and *Venkatesan* [27.130]
[f] *Properties of Silicon* [27.131]
[g] *Bhushan* and *Gupta* [27.129]
[h] *Field* [27.132]
[i] *Bhushan* [27.18]
[j] *National Carbon Company* [27.133]

and Hertz analysis was used for the calculations. In the microscale experiments, a ball coming in contact with a flat surface represents multiple-asperity contacts due to the roughness, and the contact pressure of the asperity contacts is higher than the apparent pressure. For calculation of a characteristic scale length for multiple asperity contacts, which is equal to the apparent length of contact, Hertz analysis was also used. This analysis provides an upper limit on apparent radius and lower limit on the mean contact pressure.

There are several factors responsible for the differences in the coefficients of friction at the micro- and nanoscale. Among them are the contributions from wear and contaminant particles, transition from elasticity to plasticity, and the meniscus effect [27.134–137].

The contribution of wear and contaminant particles is more significant at the macro/microscale because of the larger number of trapped particles, referred to as third-body contribution. It can be argued that for the nanoscale AFM experiments the asperity contacts are predominantly elastic (with average real pressure being less than the hardness of the softer material), and adhesion is the main contribution to the friction, whereas for the microscale experiments the asperity contacts are predominantly plastic, and deformation is an important factor. It will be shown later that hardness has a scale effect; it increases with decreasing scale and is responsible for less deformation on a smaller scale. The meniscus effect results in an increase of friction with increasing tip radius (Fig. 27.33). Therefore, third-

body contribution, scale-dependent hardness, and other properties transition from elastic contacts in nanoscale contacts to plastic deformation in microscale contacts, and meniscus contribution plays an important role.

Friction is a complex phenomenon, which involves asperity interactions involving adhesion and deformation (plowing). Adhesion and plastic deformation imply energy dissipation, which is responsible for friction (Fig. 27.36) [27.103, 104]. A contact between two bodies takes place on high asperities, and the real area of contact (A_r) is a small fraction of the apparent area of contact. During contact of two asperities, a lateral force may be required for asperities of a given slope to climb against each other. This mechanism is known as the ratchet mechanism, and it also contributes to the friction. Wear and contaminant particles present at the interface, referred as the *third body*, also contribute to the friction (Fig. 27.36). In addition, during contact even at low humidity, a meniscus is formed (Fig. 27.34). Generally, any liquid that wets or has a small contact angle on surfaces will condense from vapor into cracks and pores on surfaces as bulk liquid and in the form of annular-shaped capillary condensate in the contact zone. A quantitative theory of scale effects in friction should consider the scale effect on physical properties relevant to various contributions.

According to the adhesion and deformation model of friction, the coefficient of dry friction μ is a sum of the adhesion component μ_a and the deformation (plowing) component μ_d. The latter, in the presence of particles, is a sum of the asperity summits deformation component μ_{ds} and particles deformation component μ_{dp}, so that the total coefficient of friction is [27.136]

$$\begin{aligned} \mu &= \mu_a + \mu_{ds} + \mu_{dp} \\ &= \frac{F_a + F_{ds} + F_{dp}}{W} \\ &= \frac{A_{ra}\tau_a + A_{ds}\tau_{ds} + A_{dp}\tau_{dp}}{W} \;, \end{aligned}$$

(27.17)

where W is the normal load, F is the friction force, A_{ra}, A_{ds}, A_{dp} are the real areas of contact during adhesion, two-body deformation and with particles, respectively, and τ is the shear strength. The subscripts a, ds, and dp correspond to adhesion, summit deformation, and particle deformation, respectively.

The adhesional component of friction depends on the real area of contact and adhesion shear strength. The real area of contact is scale-dependent due to the scale dependence of the surface roughness (for elastic and plastic contact) and due to the scale dependence of hardness (for plastic contact) [27.136]. We limit the analysis here to the multiple-asperity contact. For this case, scale L is defined as appar-
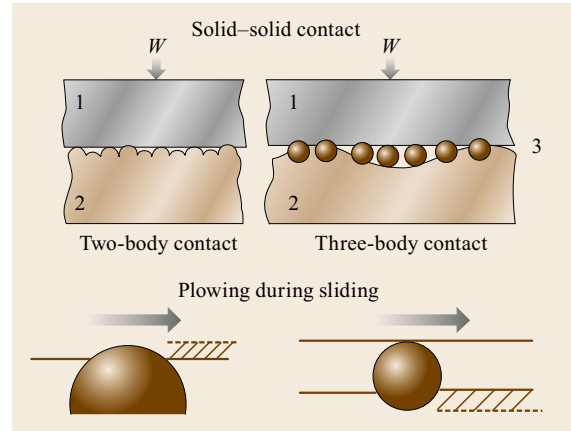

Fig. 27.36 Schematic of two- and three-body dry rough surface contacts

ent size of contact between two bodies. (For completeness, for a single-asperity contact, scale is defined as the contact diameter.) It is suggested by *Bhushan* and *Nosonovsky* [27.135] that for many materials, dislocation-assisted sliding (microslip) is the main mechanism responsible for shear strength. They considered dislocation-assisted sliding based on the assumption that contributing dislocations are located in a subsurface volume. The thickness of this volume is limited by the distance which dislocations can climb ℓ_s (material parameter) and by the radius of contact a. They showed that τ_a is scale-dependent. Based on this, the adhesional components of the coefficient of friction in the case of elastic contact μ_{ae} and in the case of plastic contact μ_{ap} are given as [27.135]

$$\mu_{ae} = \frac{\mu_{ae0}}{\sqrt{\ell + (\ell_s\sqrt{a_0})}}\left(\frac{L}{L_{\ell c}}\right)^{m-n}$$
$$\sqrt{1 + \left(\frac{L_s}{L}\right)^m}\,, \quad L < L_{\ell c}$$

(27.18)

$$\mu_{ap} = \mu_{ap0}\sqrt{\frac{1 + (\ell_d\sqrt{a_0})}{1 + (\ell_s\sqrt{a_0})}}\sqrt{\frac{1 + (L_s/L)^m}{1 + (L_d/L)^m}}\,,$$
$$L < L_{\ell c}\,,$$

(27.19)

where μ_{ae0} and μ_{ap0} are values of the coefficient of friction at the macroscale ($L \geq L_{\ell c}$), m and n are indices which characterize the scale dependence of surface parameters, $\bar{a}_0$ is the macroscale value of mean contact radius, $L_{\ell c}$ is the long wavelength limit for scale dependence of the contact parameters, ℓ_s and ℓ_d are material-specific characteristic length parameters, and L_s and L_d are length parameters related to ℓ_s and ℓ_d. Scale dependence of the adhesional component of the

coefficient of friction is presented in Fig. 27.37, based on (27.18) and (27.19).
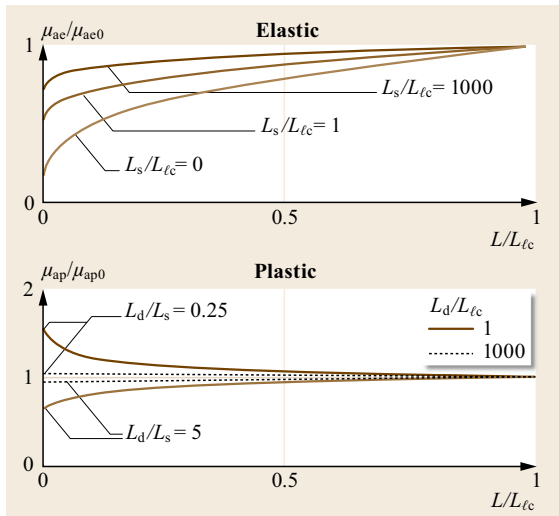
On the basis of the assumption that multiple asperities of two rough surfaces in contact have a conical shape, the two-body deformation component of friction can be determined as [27.103, 104]

$$\mu_{ds} = \frac{2 \tan \theta_r}{\pi} , \qquad (27.20)$$

where θ_r is the roughness angle (or attack angle) of a conical asperity. Mechanical properties affect the real area of contact and shear strength, and these cancel out in (27.16) [27.136]. On the basis of a statistical analysis of a random Gaussian surface [27.136]

$$\mu_{ds} = \frac{2\sigma_0}{\pi\beta_0*} \left(\frac{L}{L_{\ell c}} \right)^{n-m}$$
$$= \mu_{ds0} \left(\frac{L}{L_{\ell c}} \right)^{n-m} , \quad L < L_{\ell c} , \qquad (27.21)$$

where μ_{ds} is the value of the coefficient of summits deformation component of the coefficient of friction at macroscale ($L \geq L_{\ell c}$), and σ_0 and β_0^* are macroscale values of standard deviation of surface heights and correlation length, respectively, for a Gaussian surface. The scale dependence for the two-body deformation component of the coefficient of friction is presented in Fig. 27.38 (top curve) for $m = 0.5$, $n = 0.2$, based on (27.21). The coefficient of friction increases with

decreasing scale, according to (27.21). This effect is a consequence of increasing average slope or roughness angle.

For the three-body deformation, it is assumed that wear and contaminant particles at the borders of the contact region are likely to leave the contact region, while the particles in the center are likely to stay (Fig. 27.39). The plowing three-body deformation is plastic and, assuming that particles are harder than the bodies, the shear strength τ_{dp} is equal to the shear yield strength of the softer body τ_Y, the three-body deformation component of the coefficient of friction is given by [27.137]

$$\mu_{dp} = \mu_{dp0} n_{tr} \frac{\overline{d}^2}{\overline{d}_0^2} \frac{\sqrt{1 + 2\ell_d \sqrt{d}}}{\sqrt{1 + 2\ell_d \sqrt{d_0}}} , \qquad (27.22)$$

where $\overline{d}$ is the mean particle diameter, $\overline{d}_0$ is the macroscale value of mean particle diameter, n_{tr} is the number of trapped particles divided by total number of particles, and μ_{dp0} is the macroscale ($L \to \infty$, $n_{tr} \to 1$)

Fig. 27.38 Normalized results for the two-body deformation component of the coefficient of friction, and the number of trapped particles divided by the total number of particles and three-body deformation component of the coefficient of friction, normalized by the macroscale value for log-normal distribution of debris size, where α is the probability of a particle in the border zone to leave the contact region. Various constants given in the figure correspond to log-normal distribution (after [27.136])
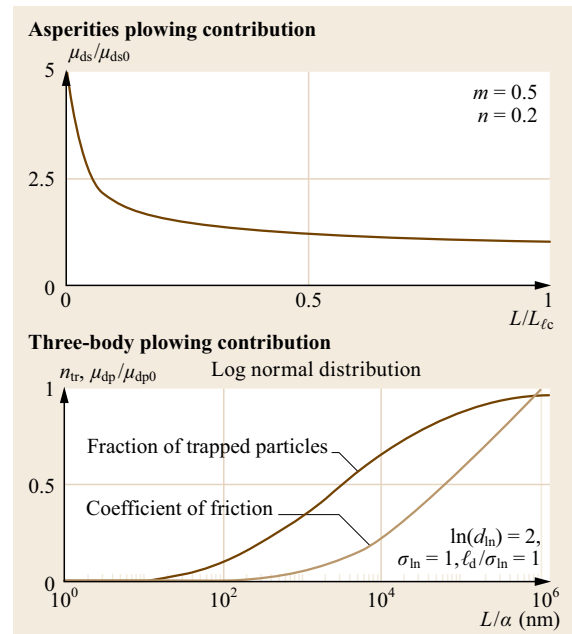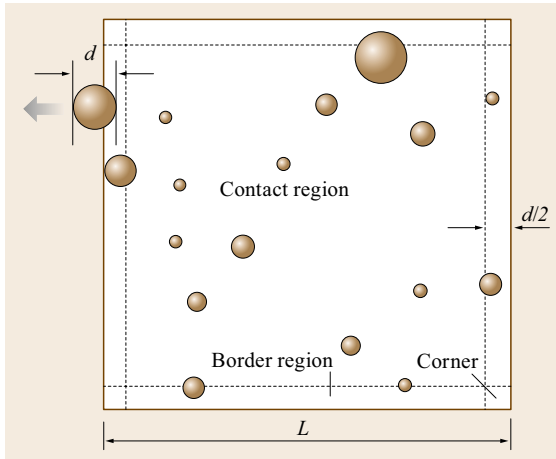

Fig. 27.37 Normalized results for the adhesional component of coefficient of friction, as a function of $L/L_{\ell c}$ for the multiple-asperity contact. Data are presented for $m = 0.5$, $n = 0.2$. For the multiple-asperity plastic contact, data are presented for two values of $L_d/L_{\ell c}$ (after [27.136])
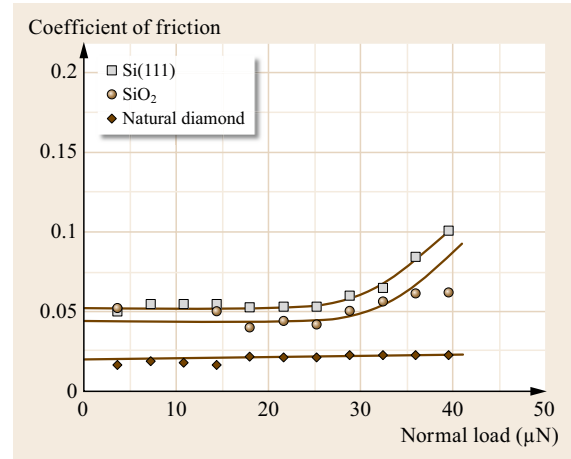
Fig. 27.39 Schematics of debris at the contact zone and at its border region. A particle of diameter d in the border region of $d/2$ is likely to leave the contact zone (after [27.136])

Fig. 27.40 Coefficient of friction as a function of normal load and for Si(111), SiO$_2$ coating and natural diamond. Inflections in the *curves* for Si and SiO$_2$ correspond to the contact stresses equal to the hardnesses of these materials (after [27.60])

value of the third-body deformation component of the coefficient of friction. Scale dependence of μ_{dp} is shown in Fig. 27.38 (bottom curve) based on (27.22). Based on the scale effect predictions presented in Figs. 27.37 and 27.38, trends in the experimental results in Table 27.3 can be explained.

Scale dependence of meniscus effects in friction, wear, and interface temperature can be analyzed in a similar way [27.137].

To demonstrate the load dependence of friction at the nano/microscale, the coefficient of friction as a function of normal load is presented in Fig. 27.40.

The coefficient of friction was measured by *Bhushan* and *Kulkarni* [27.60] for a Si$_3$N$_4$ tip versus Si, SiO$_2$, and natural diamond using an AFM. They reported that for low loads, the coefficient of friction is independent of load and increases with increasing load after a certain load. It is noted that the critical value of loads for Si and SiO$_2$ corresponds to stresses equal to their hardness values, which suggests that the transition to plasticity plays a role in this effect. The friction values at higher loads for Si and SiO$_2$ approach that of macroscale values.

27.3 Micro/Nanoscale Wear and Scratching, Local Deformation, and Nanofabrication/Nanomachining

27.3.1 Nanoscale Wear

Bhushan and *Ruan* [27.24] conducted nanoscale wear tests on polymeric magnetic tapes using conventional silicon nitride tips at two different loads of 10 and 100 nN (Fig. 27.41). For a low normal load of 10 nN, measurements were made twice. There was no discernible difference between consecutive measurements for this load. However, as the load was increased from 10 to 100 nN, topographical changes were observed during subsequent scanning at a normal load of 10 nN; material was pushed in the sliding direction of the AFM tip relative to the sample. The material movement is believed to occur as a result of plastic deformation of the tape surface. Thus, deformation and

movement of the soft materials on a nanoscale can be observed.

27.3.2 Microscale Scratching

The AFM can be used to investigate how surface materials can be moved or removed on micro- to nanoscales, for example, in scratching and wear [27.2, 7] (where these things are undesirable) and nanofabrication/nanomachining (where they are desirable). Figure 27.42a shows microscratches made on Si(111) at various loads and a scanning velocity of 2 μm/s after ten cycles [27.28]. As expected, the scratch depth increases linearly with load. Such microscratching measurements can be used to study failure mechanisms on
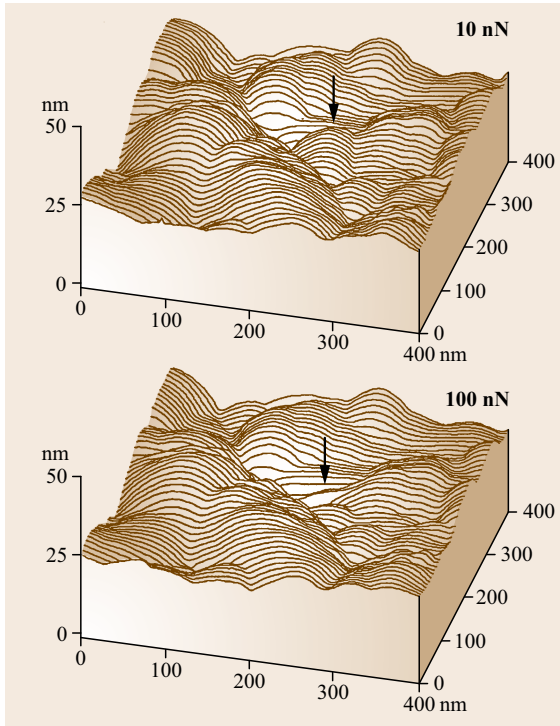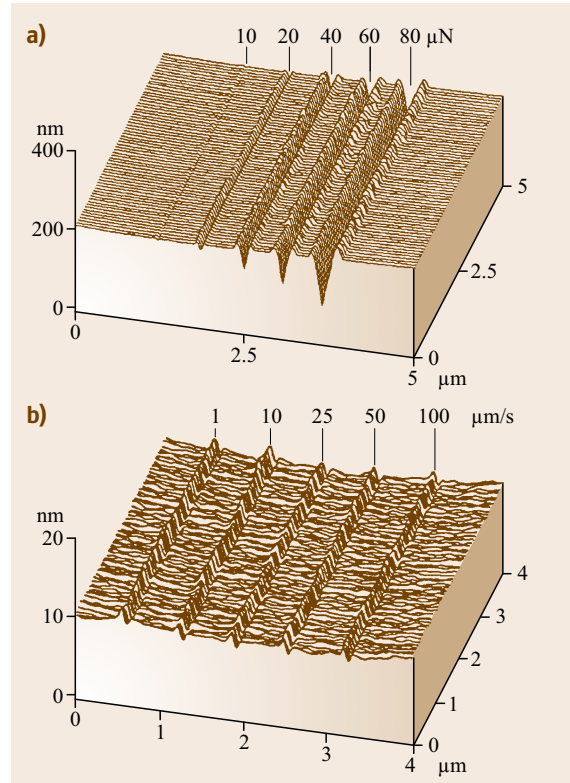
Fig. 27.41 Surface roughness maps of a polymeric magnetic tape at the applied normal load of 10 and 100 nN. Location of the change in surface topography as a result of nanowear is indicated by *arrows* (after [27.24])


Fig. 27.42a,b Surface plots of **(a)** Si(111) scratched for ten cycles at various loads and a scanning velocity of 2 μm/s (after [27.28]). Note that *x*- and *y*-axes are in μm and the *z*-axis is in nm, and **(b)** Si(100) scratched in one unidirectional scan cycle at a normal force of 80 μN and different scanning velocities (after [27.31])

the microscale and to evaluate the mechanical integrity (scratch resistance) of ultrathin films at low loads.

To study the effect of scanning velocity, unidirectional scratches 5 μm in length were generated at scanning velocities ranging from 1 to 100 μm/s at various normal loads ranging from 40 to 140 μN [27.31]. There is no effect of scanning velocity obtained at a given normal load. Representative scratch profiles at 80 μN are shown in Fig. 27.42b. This may be because of a small effect of frictional heating with the change in scanning velocity used here. Furthermore, for a small change in interface temperature, there is a large underlying volume to dissipate the heat generated during scratching.

Scratching can be performed under ramped loading to determine the scratch resistance of materials and coatings [27.58]. The coefficient of friction is measured during scratching, and the load at which the coefficient of friction increases rapidly is known as the *critical load*, which is a measure of scratch resistance. In addition, postscratch imaging can be performed in situ with the AFM in tapping mode to study failure mechanisms. Figure 27.43 shows data from a scratch test on Si(100) with a scratch length of 25 μm and a scratching velocity of 0.5 μm/s. At the beginning of the scratch, the

coefficient of friction is 0.04, which indicates a typical value for silicon. At about 35 μN (indicated by the arrow in the figure), there is a sharp increase in the coefficient of friction, which indicates the critical load. Beyond the critical load, the coefficient of friction continues to increase steadily. In the postscratch image, we note that at the critical load, a clear groove starts to form. This implies that Si(100) was damaged by plowing at the critical load, associated with the plastic flow of the material. At and after the critical load, small and uniform debris is observed, and the amount of debris increases with increasing normal load. *Sundararajan* and *Bhushan* [27.58] have also used this technique to measure the scratch resistance of diamond-like carbon coatings ranging in thickness from 3.5–20 nm.

27.3.3 Microscale Wear

By scanning the sample in two dimensions with the AFM, wear scars are generated on the surface. Fig-
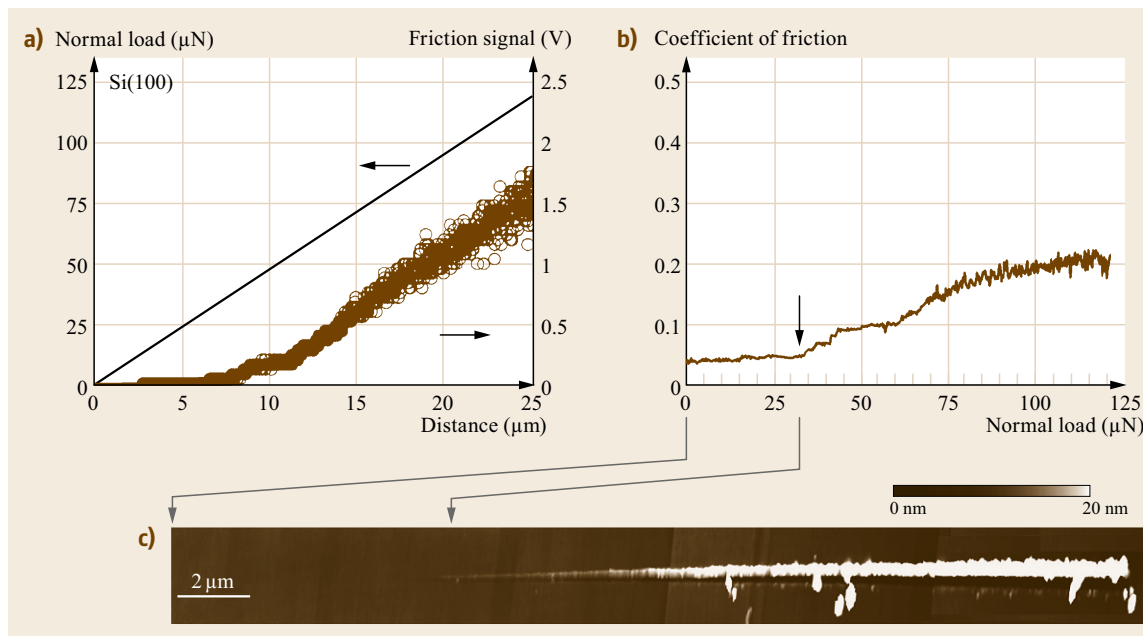
Fig. 27.43 (a) Applied normal load and friction signal measured during the microscratch experiment on Si(100) as a function of scratch distance, (b) friction data plotted in the form of coefficient of friction as a function of normal load, and (c) AFM surface height image of scratch obtained in tapping mode (after [27.58])
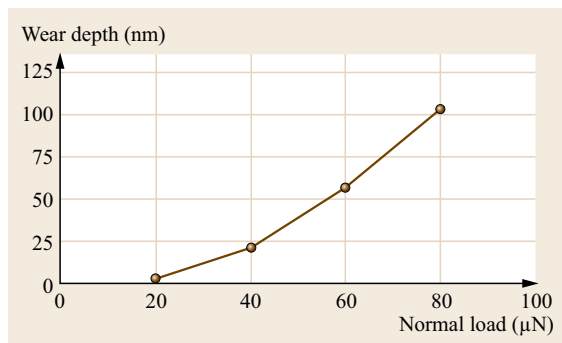
Fig. 27.44 Wear depth as a function of normal load for Si(100) after one cycle (after [27.138])

ure 27.44 shows the effect of normal load on wear depth on Si(100). We note that wear depth is very small below 20 µN of normal load [27.100, 138]. A normal load of 20 µN corresponds to contact stresses comparable to the hardness of silicon. Primarily, elastic deformation at loads below 20 µN is responsible for low wear [27.29, 30].

A typical wear mark of the size 2 µm × 2 µm generated at a normal load of 40 µN for one scan cycle and imaged using AFM with a scan size of 4 µm × 4 µm at 300 nN load is shown in Fig. 27.45a. The inverted map of wear marks shown in Fig. 27.45b indicates the uniform material removal at the bottom of the wear mark [27.100]. An AFM image of the wear mark shows debris at the edges, probably swiped during AFM scanning. This indicates that the debris is loose (not sticky) and can be removed during AFM scanning.

Next the mechanism of material removal on the microscale in AFM wear experiments is examined [27.31, 100, 138]. Figure 27.46 shows a secondary electron image of the wear mark and associated wear particles. The specimen used for the scanning electron microscope (SEM) was not scanned with the AFM after initial wear, in order to retain wear debris in the wear region. Wear debris is clearly observed. In the SEM micrographs, the wear debris appear to be agglomerated because of the high surface energy of the fine particles. Particles appear to be a mixture of rounded and so-called cutting type (feather-like or ribbon-like material). *Zhao* and *Bhushan* [27.138] reported an increase in the number and size of cutting-type particles with the normal load. The presence of cutting-type particles indicates that the material is removed primarily by plastic deformation.

To better understand the material removal mechanisms, *Zhao* and *Bhushan* [27.138] used transmission electron microscopy (TEM). The TEM micrograph of the worn region and associated diffraction pattern are shown in Fig. 27.47a,b. The bend contours are observed to pass through the wear mark in the micrograph. The bend contours around and inside the wear mark are indicative of a strain field, which in the absence of ap-
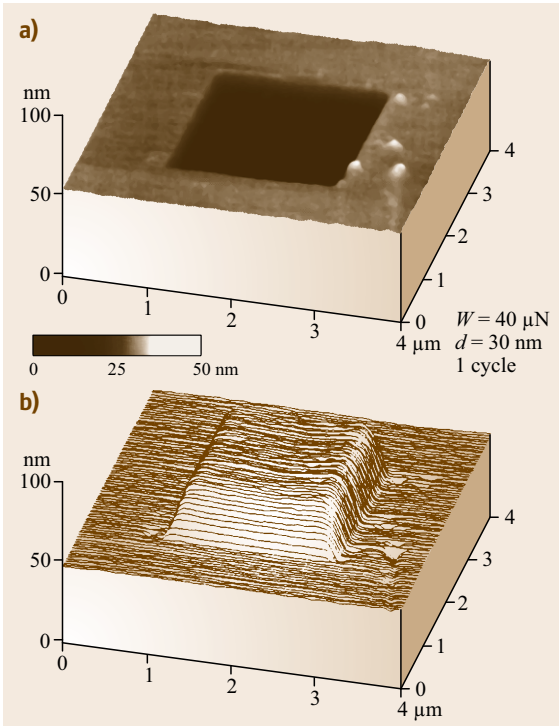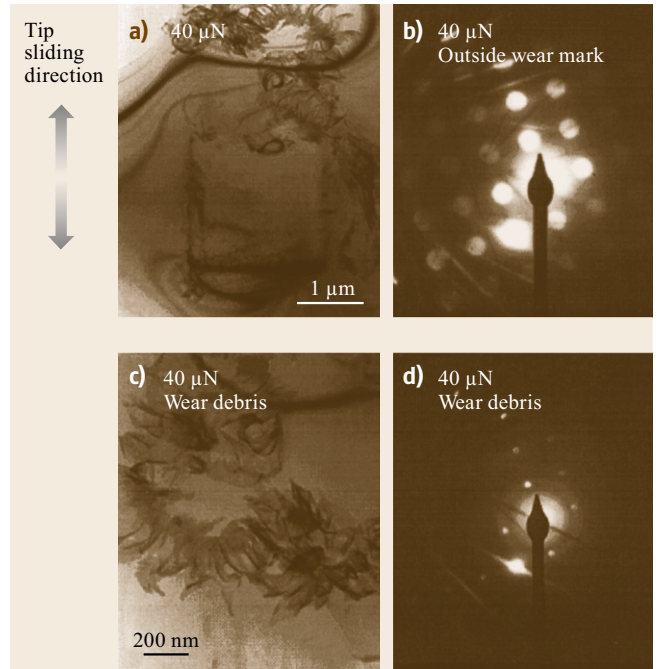
Fig. 27.45 (a) Typical gray-scale and **(b)** inverted AFM images of a wear mark created using a diamond tip at a normal load of 40 μN and one scan cycle on a Si(100) surface (after [27.100])
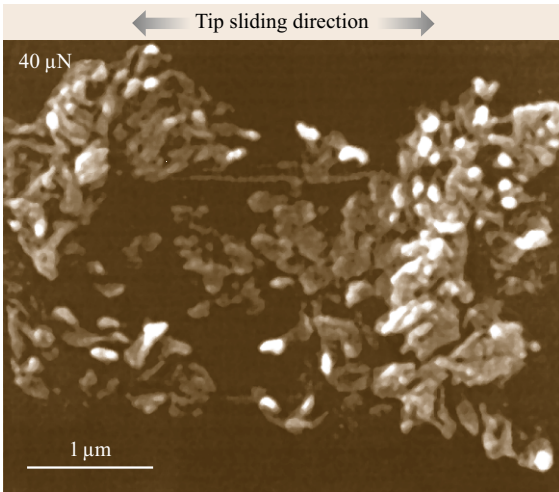
Fig. 27.46 Secondary electron image of wear mark and debris for Si(100) produced at a normal load of 40 μN and one scan cycle (after [27.138])

Fig. 27.47a–d Bright-field TEM micrographs **(a)** and diffraction patterns **(b)** of wear mark **(a,b)** and wear debris **(c,d)** in Si(100) produced at a normal load of 40 μN and one scan cycle. Bend contours around and inside wear mark are observed (after [27.138])

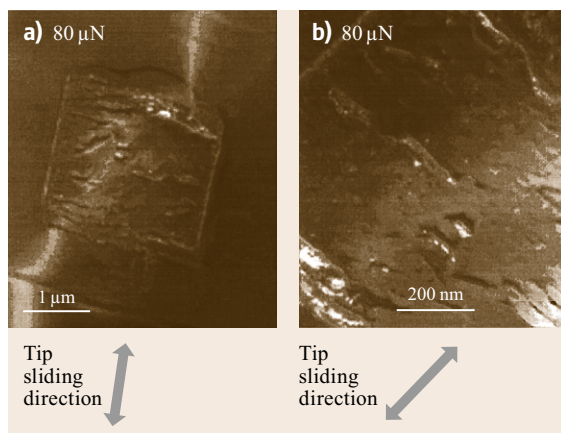plied stresses can be interpreted as plastic deformation and/or elastic residual stresses. Often, localized plastic deformation during loading would lead to residual stresses during unloading; therefore, bend contours reflect a mix of elastic and plastic strains. The wear debris is observed outside the wear mark. The enlarged view of the wear debris in Fig. 27.47c shows that much of the debris is ribbon like, indicating that material is removed by a cutting process via plastic deformation, which is consistent with the SEM observations. The diffraction pattern from inside the wear mark was reported to be similar to that of virgin silicon, indicating no evidence of any phase transformation (amorphization) during wear. A selected area diffraction pattern of the wear debris shows some diffuse rings, which indicates the existence of amorphous material in the wear debris, confirmed as silicon oxide products from chemical analysis. It is known that plastic deformation occurs by generation and propagation of dislocations. No dislocation activity or cracking was observed at 40 μN. However, dislocation arrays could be observed at 80 μN. Figure 27.48 shows the TEM micrographs of the worn region at 80 μN; for better observation of the worn surface, wear debris was moved out of the wear mark by using AFM with a large area scan at 300 nN after the wear test. The existence of dislocation arrays confirms that material removal occurs by plastic deformation. This corroborates the observations made in scratch tests at ramped load in the previous section. It

is concluded that the material on the microscale at high loads is removed by plastic deformation with a small contribution from elastic fracture [27.138].

To understand wear mechanisms, evolution of wear can be studied using AFM. Figure 27.49 shows the evolution of wear marks of a DLC-coated disk sample. The data illustrate how the microwear profile for a load of $20\,\mu N$ develops as a function of the number of scanning cycles [27.28]. Wear is not uniform, but is initiated at the nanoscratches. Surface defects (with high surface energy) present at the nanoscratches act as initiation sites for wear. Coating deposition also may not be uniform on and near nanoscratches which may lead to coating delamination. Thus, scratch-free surfaces will be relatively resistant to wear.

Wear precursors (precursors to measurable wear) can be studied by making surface potential measurements [27.81, 83, 84]. The contact potential difference, or simply the surface potential between two surfaces depends on a variety of parameters such as electronic work function, adsorption, and oxide layers. The surface potential map of an interface gives a measure of changes in the work function which is sensitive to both physical and chemical conditions of the surfaces including structural and chemical changes. Before material is actually removed in a wear process, the surface experiences stresses that result in surface and subsurface changes of structure and/or chemistry. These can cause changes in the measured potential of a surface. An AFM tip allows the mapping of the surface potential with nanoscale resolution. Surface height and change in surface potential maps of a polished single-crystal aluminum (100) sample, abraded using a diamond tip at loads of 1 and $9\,\mu N$, are shown in Fig. 27.50a. It is evident

that both abraded regions show a large potential contrast ($\approx 0.17\,V$), with respect to the nonabraded area. The black region in the lower right-hand part of the

Fig. 27.48 (a) Bright-field and **(b)** weak-beam TEM micrographs of wear mark in Si(100) produced at a normal load of $80\,\mu N$ and one scan cycle showing bend contours and dislocations (after [27.138])
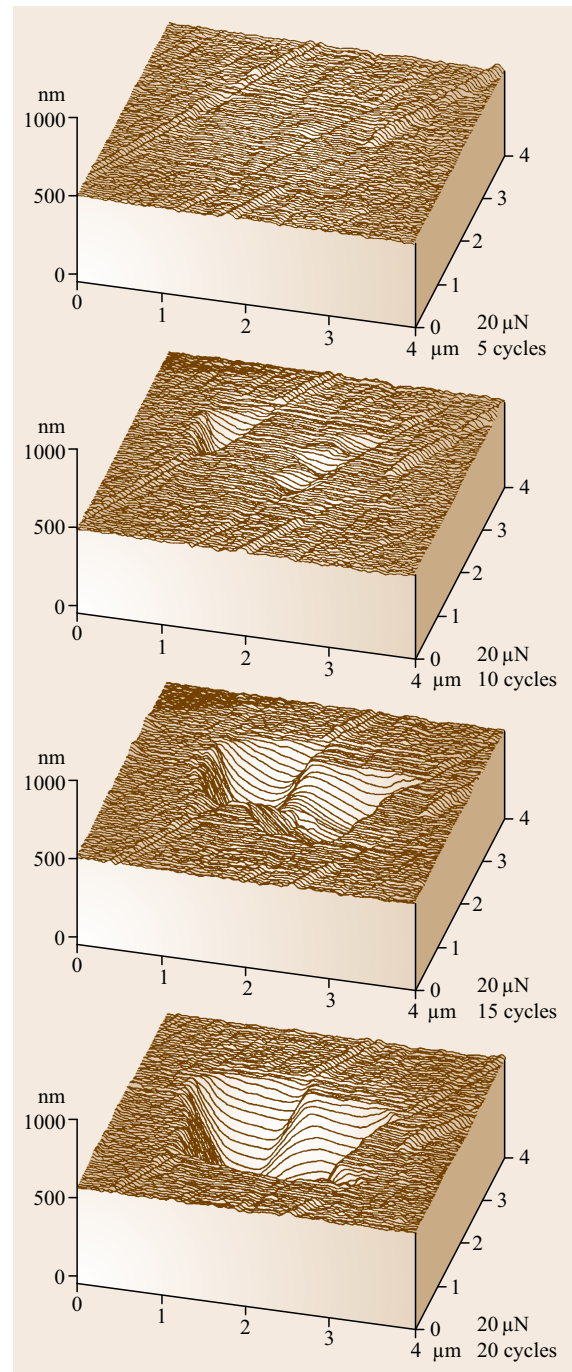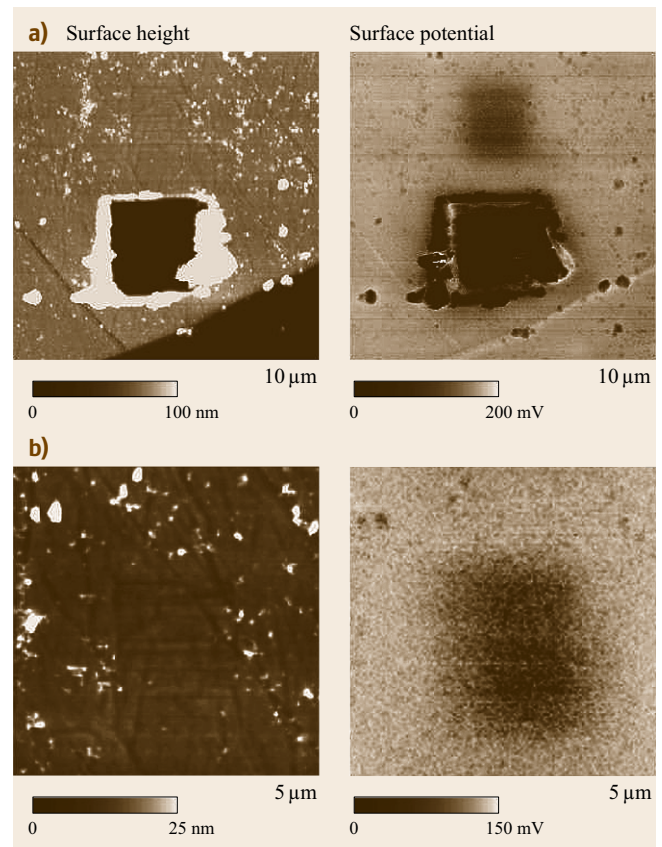

Fig. 27.49 Surface plots of a diamond-like carbon-coated thin-film disk showing the worn region; the normal load and number of test cycles are indicated (after [27.28])

topography scan shows a step that was created during the polishing phase. There is no potential contrast between the high region and the low region of the sample, indicating that the technique is independent of surface height. Figure 27.50b shows a close-up scan of the upper (low load) wear region in Fig. 27.50a. Notice that while there is no detectable change in the surface topography, there is nonetheless, a large change in the potential of the surface in the worn region. Indeed, the wear mark of Fig. 27.50b might not be visible at all in the topography map were it not for the noted absence of wear debris generated nearby and then swept off during the low load scan. Thus, even in the case of zero wear (no measurable deformation of the surface using AFM), there can be a significant change in the surface potential inside the wear mark which is useful for the study of wear precursors. It is believed that the removal of the thin contaminant layer including the natural oxide layer gives rise to the initial change in surface potential. The structural changes, which precede the generation of wear debris and/or measurable wear scars, occur under ultralow loads in the top few nanometers of the sample, and are primarily responsible for the subsequent changes in surface potential.

Surface potential measurements using the nano-Kelvin probe technique have been used to study wear and degradation for various applications such as for human skin [27.139], human hair [27.107, 140], Li-ion batteries [27.141] and MEMS switches [27.142].

### 27.3.4 In situ Characterization of Local Deformation

In situ surface characterization of local deformation of materials and thin films is carried out using a tensile stage inside an AFM [27.73–75, 85, 86]. As an example, failure mechanisms of coated polymeric thin films under tensile load were studied by *Bobji* and *Bhushan* [27.73, 74]. The specimens were strained at a rate of $4 \times 10^{-3}\%/s$, and AFM images were captured at different strains up to about 10% to monitor generation and propagation of cracks and deformation bands. *Bobji* and *Bhushan* [27.73, 74] studied three magnetic tapes of thickness ranging from 7 to 8.5 μm. One of these had an acicular-shaped metal particle (MP) coating while the other two had metal-evaporated (ME) coatings with and without a thin diamond-like carbon (DLC) overcoat both on a polymeric substrate; all had a particulate back coating [27.16]. They also studied a polyethylene terephthalate (PET) substrate with 6 μm thickness. They reported that cracking of the coatings started at about 1% strain for all tapes much before the substrate starts to yield at about 2% strain. Figure 27.51 shows the topographical images of the MP tape at dif-

a) Surface height   Surface potential

0   100 nm   10 μm   0   200 mV   10 μm

b)

0   25 nm   5 μm   0   150 mV   5 μm

Fig. 27.50 (a) Surface height and change in surface potential maps of wear regions generated at 1 μN (*left*) and 9 μN (*right*) on a single-crystal aluminum sample showing bright contrast in the surface potential map on the worn regions. **(b)** Close up of upper (low load) wear region (after [27.83])

ferent strains. At 0.83% strain, a crack can be seen, originating at the marked point. As the tape is further stretched along the direction, as shown in Fig. 27.51, the crack propagates along the shorter boundary of the ellipsoidal particle. However, the general direction of crack propagation remains perpendicular to the direction of stretching. The length, width, and depth of the cracks increase with strain, and at the same time newer cracks keep nucleating and propagating with reduced crack spacing. At 3.75% strain, another crack can be seen nucleating. This crack continues to grow parallel to the first one. When the tape is unloaded after stretching up to a strain of about 2%, i. e., within the elastic limit of the substrate, the cracks close perfectly, and it is impossible to determine the difference from the unstrained tape.

Figure 27.52 shows topographical images of the three magnetic tapes and the PET substrate after being strained to 3.75%, which is well beyond the elastic
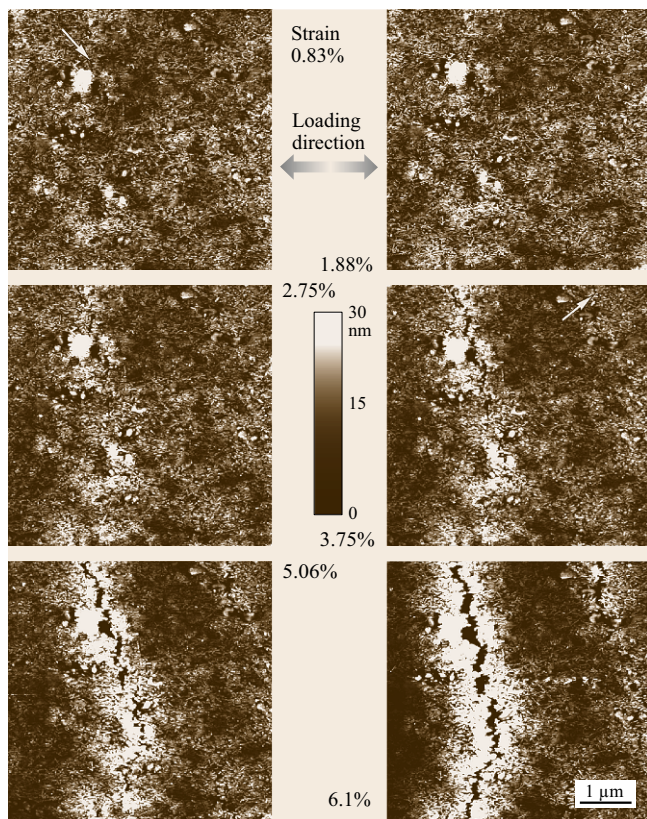
Fig. 27.51 Topographical images of the MP magnetic tape at different strains (after [27.73])
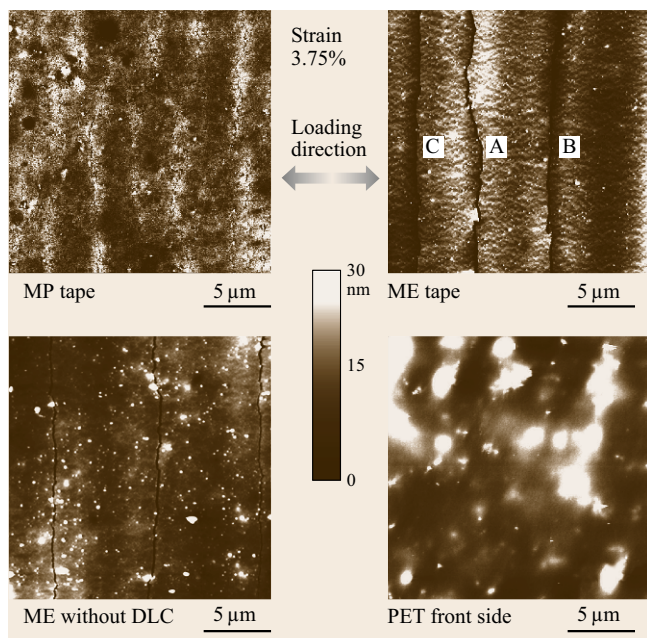
Fig. 27.52 Comparison of crack morphologies at 3.75% strain in three magnetic tapes and for a PET substrate. Cracks B and C, nucleated at higher strains, are more linear than crack A (after [27.74])

limit of the substrate. The MP tape develops short and numerous cracks perpendicular to the direction of loading. In tapes with metallic coating, the cracks extend throughout the tape width. In the ME tape with the DLC coating, there is a bulge in the coating around the primary cracks that are initiated when the substrate is still elastic, like crack A in the figure. The white band on the right-hand side of the figure is the bulge of another crack. The secondary cracks like B and C are generated at higher strains and are straighter compared to the primary cracks. In the ME tape which has a Co-O film on a PET substrate, with a thickness ratio of 0.03, both with and without DLC coating, no difference is observed in the rate of growth between primary and secondary cracks. The failure is cohesive with no bulging of the coating. This seems to suggest that the DLC coating has residual stresses that relax when the coating cracks, causing delamination. Since the stresses are already relaxed, the secondary crack does not result in delamination. The presence of the residual stress is confirmed by the fact that a free-standing ME tape curls up (in a cylindrical form with its axis perpendicular to the tape length) with a radius of curvature of about 6 mm, and the ME tape without the DLC does not curl. The magnetic coating side of the PET substrate is much smoother at smaller scan lengths. However, in the 20 μm scans it has a lot of bulging out, which appears as white spots in the figure. These spots change shape even when the samples are scanned in tapping mode at very low contact forces.

The variation of average crack width and average crack spacing with strain is plotted in Fig. 27.53. The crack width is measured at a spot along a given crack over a distance of 1 μm in the 5 μm scan image at different strains. The crack spacing is obtained by averaging the intercrack distance measured in five separate 50 μm scans at each strain. It can be seen that the cracks nucleate at a strain of about 0.7%–1.0%, well within the elastic limit of the substrate. There is a definite change in the slope of the load–displacement curve at the strain where cracks nucleate, and the slope after that is closer to the slope of the elastic portion of the substrate. This would mean that most of the load is supported by the substrate once the coating fails by cracking.

Fatigue experiments can be performed by applying a cyclic stress amplitude with a certain mean stress [27.75]. Fatigue life was determined by the first occurrence of cracks. Experiments were performed at various constant mean stresses and with a range of cyclic stress amplitudes for each mean stress value for various magnetic tapes. Number of cycles to failure was plotted as a function of stress state to obtain a so-called S–N (stress–life) diagram. As the stress is decreased,
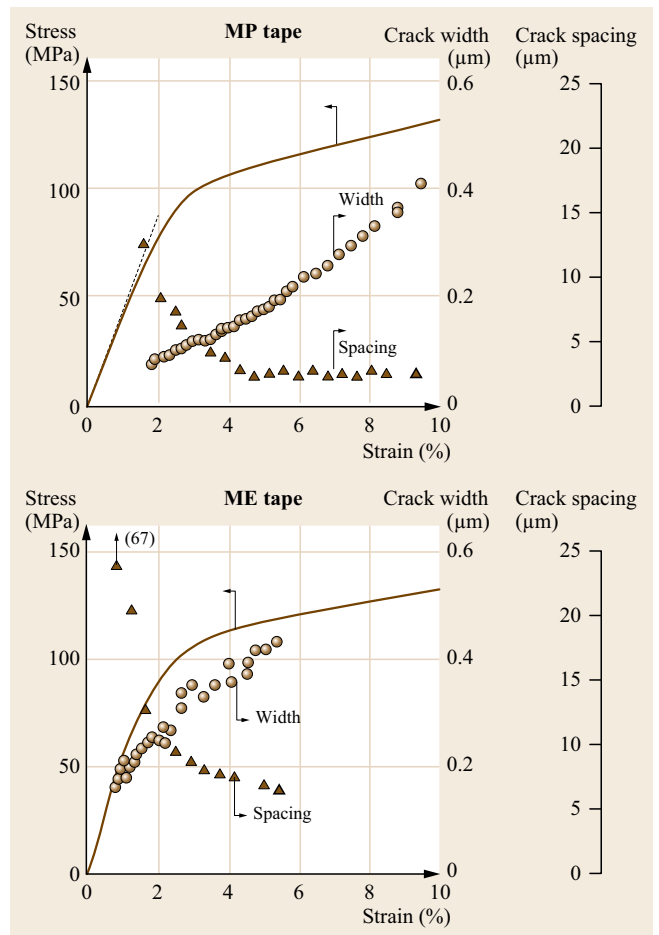

Fig. 27.53 Variation of stress, crack width, and crack spacing with strain in two magnetic tapes (after [27.73])

there is a stress value for which no failure occurs. This stress is termed the endurance limit or simply fatigue limit. Figure 27.54 shows the S–N curve for an ME tape and an ME tape without DLC. For the ME tape, the endurance limit is seen to go down with a decrease in mean stress. This is consistent with the literature, and is because at a lower mean stress the corresponding stress amplitude is relatively high and this causes failure. The endurance limit is found to be almost the same for all three mean stresses. In the case of the ME tape without DLC, the critical number of cycles is found to also be in the same range.

In situ surface characterization of unstretched and stretched films has been used to measure Poisson's ratio of polymeric thin films by *Bhushan* et al. [27.95]. Uniaxial tension is applied by the tensile stage. Surface height profiles obtained from the AFM images of unstretched and stretched samples are used to monitor the changes in displacements of the polymer films
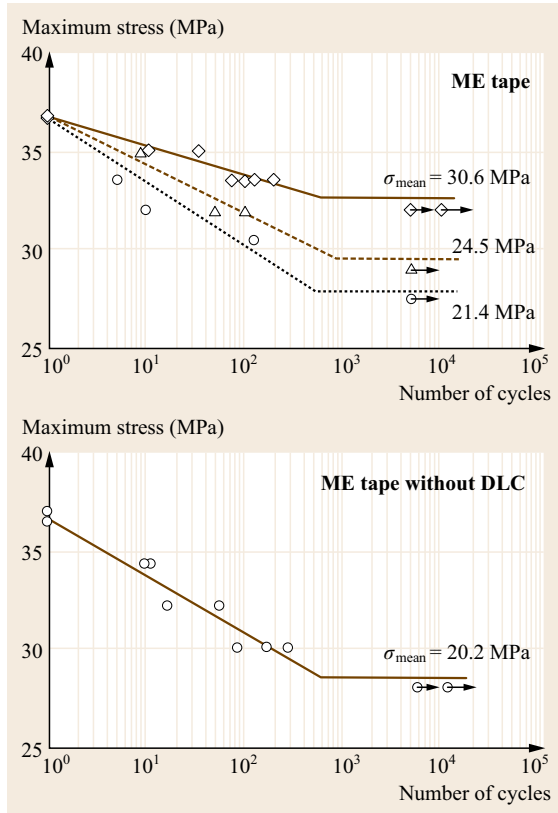
Fig. 27.54 *S–N* curve for two magnetic tapes with maximum stress plotted on the *ordinate* and number of cycles to failure on the *abscissa*. The data points marked with *arrows* indicate tests for which no failure (cracking) was observed in the scan area, even after a large number of cycles (10 000) (after [27.75])

in the longitudinal and lateral directions simultaneously.

27.3.5 Nanofabrication/Nanomachining

An AFM can be used for nanofabrication/nanomachining by extending the microscale scratching operation [27.2, 20, 28, 79]. Figure 27.55 shows two examples of nanofabrication. The patterns were created on a single-crystal silicon (100) wafer by scratching the sample surface with a diamond tip at specified locations and scratching angles. Each line is inscribed manually at a normal load of $15\,\mu$N and a writing speed of $0.5\,\mu$m/s. The separation between lines is about 50 nm, and the variation in line width is due to the tip asymmetry. Nanofabrication parameters – normal load, scanning speed, and tip geometry – can be controlled precisely to control the depth and length of the devices.
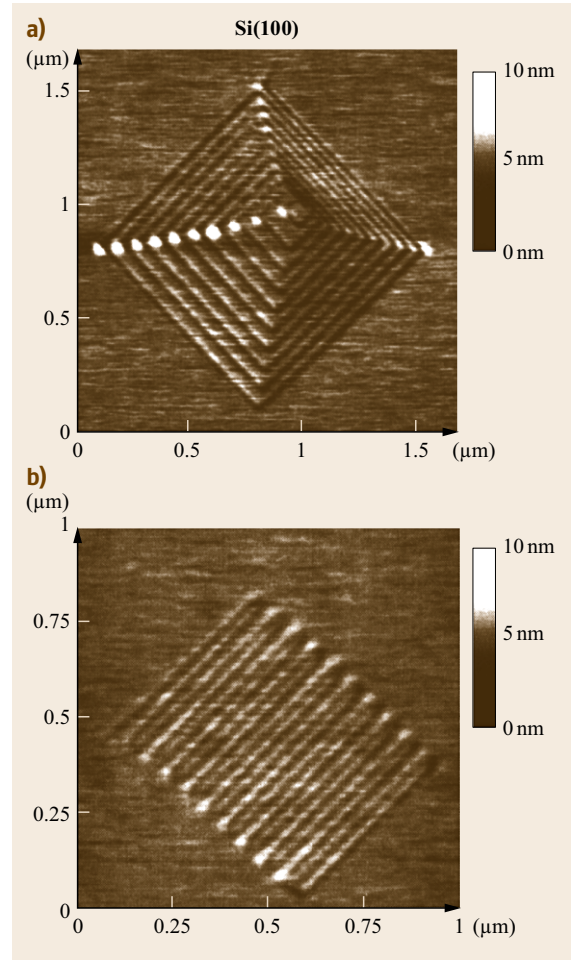
Fig. 27.55 **(a)** Trim and **(b)** spiral patterns generated by scratching an Si(100) surface using a diamond tip at a normal load of $15\,\mu$N and writing speed of $0.5\,\mu$m/s (after [27.2, 7])

Nanofabrication using mechanical scratching has several advantages over other techniques. Better control over the applied normal load, scan size, and scanning speed can be used for the nanofabrication of devices. Using the technique, nanofabrication can be performed on any engineering surface. Chemical etching or reactions is not required, and this dry nanofabrication process can be employed where the use of chemicals and electric field is prohibited. One disadvantage of this technique is the formation of debris during scratching. At light loads, debris formation is not a problem compared to high-load scratching. However, debris can be removed easily from the scan area at light loads during scanning.
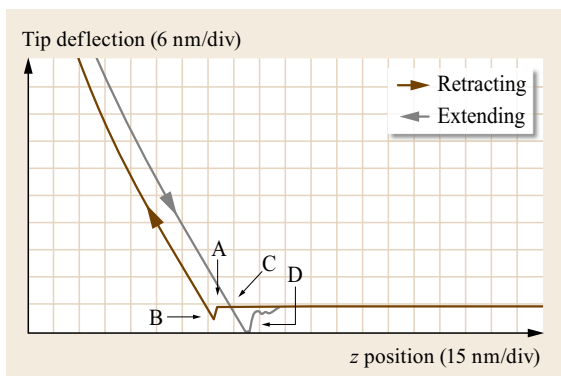
27.4 Indentation

Mechanical properties on the relevant scales are needed for the analysis of friction and wear mechanisms. Mechanical properties, such as hardness and Young's modulus of elasticity, can be determined on the micro- to picoscales using the AFM [27.24, 28, 55, 61] and a depth-sensing indentation system used in conjunction with an AFM [27.60, 143–145].

27.4.1 Picoindentation

Indentability on the scale of subnanometers of soft samples can be studied in the force calibration mode (Fig. 27.7) by monitoring the slope of cantilever deflection as a function of the sample traveling distance after the tip is engaged and the sample is pushed against the tip. For a rigid sample, the cantilever deflection equals the sample traveling distance, but the former quantity is smaller if the tip indents the sample. In an example for a polymeric magnetic tape shown in Fig. 27.56, the line in the left portion of the figure is curved with a slope of less than 1 shortly after the sample touches the tip, which suggests that the tip has indented the sample [27.24]. Later, the slope is equal to 1, suggesting that the tip no longer indents the sample. This observation indicates that the tape surface is soft locally (polymer rich) but hard (as a result of magnetic particles) underneath. Since the curves in extending and retracting modes are identical, the indentation is elastic up to a maximum load of about 22 nN used in the measurements.

Detection of the transfer of material on a nanoscale is possible with the AFM. Indentation of C_{60}-rich fullerene films with an AFM tip has been shown [27.59] to result in the transfer of fullerene molecules to the AFM tip, as indicated by discontinuities in the can-
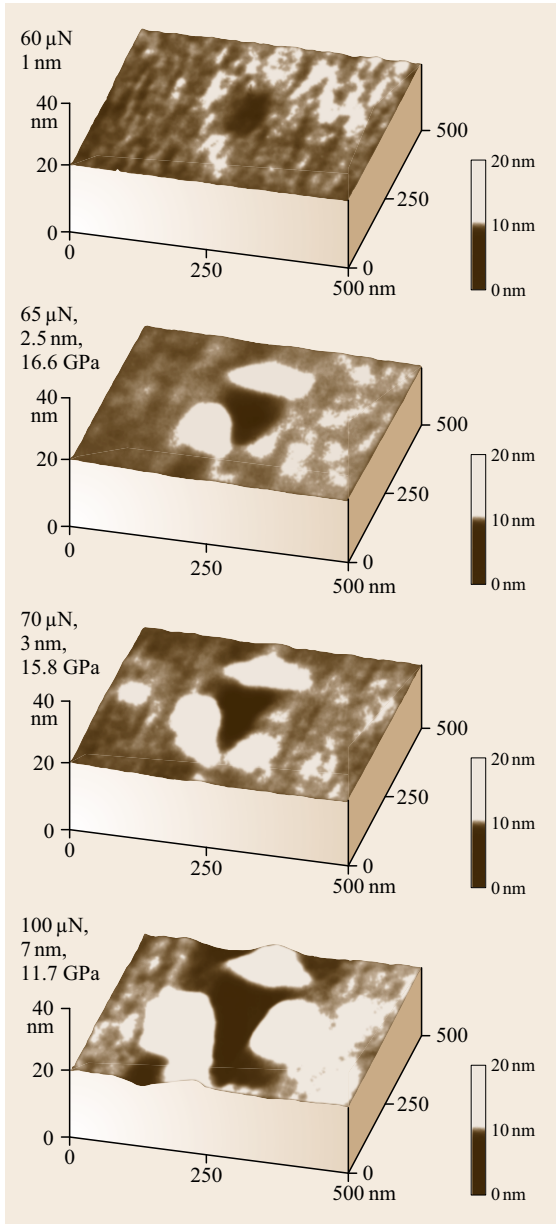
tilever deflection as a function of the sample traveling distance in subsequent indentation studies.

27.4.2 Nanoindentation

The indentation hardness of surface films with an indentation depth of as small as about 1 nm can be measured using an AFM [27.1, 16, 61]. Figure 27.57 shows the gray-scale plots of indentation marks made on Si(111) at normal loads of 60, 65, 70, and 100 μN. Triangular indents can be clearly observed with very shallow depths. At a normal load of 60 μN, indents are observed, and the depth of penetration is about 1 nm. As the normal load is increased, the indents become clearer, and indentation depth increases. For the case of hardness measurements at shallow depths on the same order as variations in surface roughness, it is desirable to subtract the original (unindented) map from the indent map for an accurate measurement of the indentation size and depth [27.28].
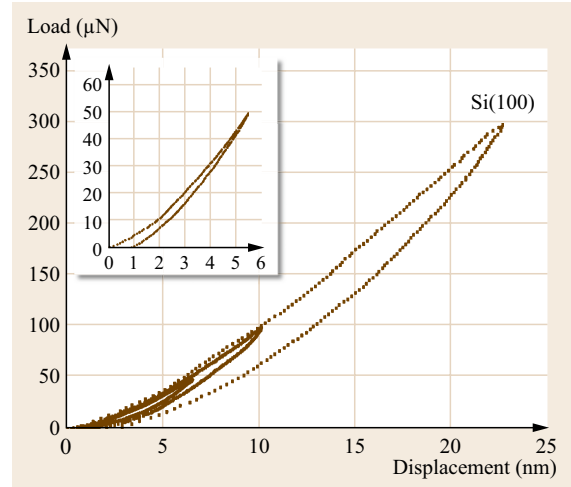
To make accurate measurements of hardness at shallow depths, a depth-sensing nano/picoindentation system (Fig. 27.9) is used [27.60]. Figure 27.58 shows the load–displacement curves at different peak loads for Si(100). Loading/unloading curves often exhibit sharp discontinuities, particularly at high loads. Discontinuities, also referred to as pop-ins, occurring during the initial loading part of the curve mark a sharp transition from pure elastic loading to a plastic deformation of the specimen surface, thus corresponding to an initial yield point. The sharp discontinuities in the unloading part of the curves are believed to be due to the formation of lateral cracks which form at the base of the median crack, which results in the surface of the specimen being thrust upward. Load–displacement data at residual depths as low as about 1 nm can be obtained. The indentation hardness of surface films has been measured for various materials at a range of loads including Si(100) up to a peak load of 500 μN and Al(100) up to a peak load of 2000 μN by *Bhushan* et al. [27.60] and *Kulkarni* and *Bhushan* [27.3, 16]. The hardnesses of single-crystal silicon and single-crystal aluminum at shallow depths on the order of a few nm (on a nanoscale) are found to be higher than at depths on the order of a few hundred nm (on a microscale) (Fig. 27.59). Microhardness has also been reported to be higher than that on the millimeter scale by several investigators. The data reported to date show that hardness exhibits a scale (size) effect.

During loading, the generation and propagation of dislocations are responsible for plastic deformation. A strain-gradient plasticity theory has been devel-

Fig. 27.56 Tip deflection (normal load) as a function of the z (separation distance) curve for a polymeric magnetic tape (after [27.24])
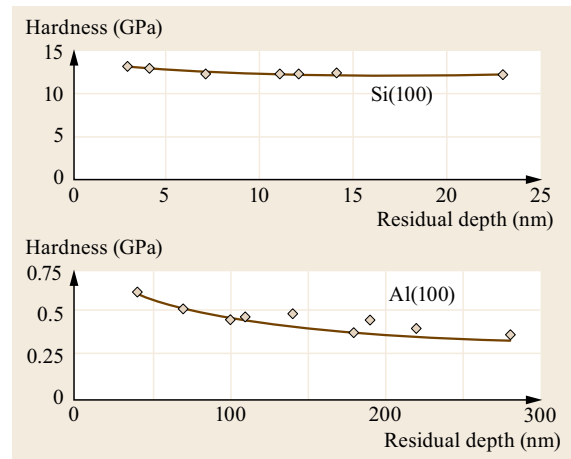
Fig. 27.57 Gray-scale plots of indentation marks on the Si(111) sample at various indentation loads. Loads, indentation depths and hardness values are listed in the figure (after [27.61])

Fig. 27.58 Load–displacement curves at various peak loads for Si(100); *inset* shows the magnified curve for a peak load of 50 μN (after [27.60])

Fig. 27.59 Indentation hardness as a function of residual indentation depth for Si(100) (after [27.60]), and Al(100) (after [27.143])

oped for micro/nanoscale deformations, and is based on randomly created statistically stored and geometrically necessary dislocations [27.146, 147]. Large strain gradients inherent in small indentations lead to the accumulation of geometrically necessary dislocations, located in a certain sub-surface volume, for strain compatibility reasons. The large strain gradients in small indentations require these dislocations to account for the large slope at the indented surface. These dislocations become obstacles to other dislocations that cause enhanced hardening. These are a function of strain gradient, whereas statistically, stored dislocations are a function of strain. Based on this theory, scale-dependent hardness is given as

$$H = H_0 \sqrt{1 + \frac{\ell_d}{a}}\,, \tag{27.23}$$

where H_0 is the hardness in the absence of strain gradient or macrohardness, ℓ_d is the material-specific

characteristic length parameter, and *a* is the contact radius. In addition to the role of the strain-gradient plasticity theory, an increase in hardness with a decrease in indentation depth can possibly be rationalized on the basis that as the volume of deformed material decreases, there is a lower probability of encountering material defects.

Bhushan and *Koinkar* [27.55] used AFM measurements to show that ion implantation of silicon surfaces increases their hardness and thus their wear resistance. Formation of surface alloy films with improved mechanical properties by ion implantation is of growing technological importance as a means of improving the mechanical properties of materials. Hardness of 20 nm thick DLC films have been measured by *Kulkarni* and *Bhushan* [27.145].

To measure variations in mechanical properties of layered materials and nonhomogeneous composites, a so-called continuous stiffness technique is used [27.62]. The technique offers a direct measurement of dynamic contact stiffness during the loading portion of an indentation test. This allows the measurement of contact stiffness, elastic modulus, hardness, and fatigue properties. For example, the technique has been used in layered and nonhomogeneous magnetic tapes.

The creep and strain rate effects (viscoelastic effects) of ceramics can be studied using a depth-sensing indentation system. *Bhushan* et al. [27.60] and *Kulkarni* and *Bhushan* [27.143–145] have reported that ceramics (single-crystal silicon and diamond-like carbon) exhibit significant plasticity and creep on a nanoscale. Figure 27.60a shows the load–displacement curves for single-crystal silicon at various peak loads held at 180 s.

To demonstrate the creep effects, the load–displacement curves for a 500 μN peak load held at 0 and 30 s are also shown as an inset. Note that significant creep occurs at room temperature. Nanoindenter experiments conducted by *Li* et al. [27.148] exhibited significant creep only at high temperatures (greater than or equal to 0.25 times the melting point of silicon). The mechanism of dislocation glide plasticity is believed to dominate the indentation creep process on the macroscale. To study the strain rate sensitivity of silicon, data at two different (constant) rates of loading are presented in Fig. 27.60b. Note that a change in the loading rate by a factor of about five results in a significant change in the load–displacement data. The viscoelastic effects observed here for silicon at ambient temperature could arise from the size effects mentioned earlier. Most likely, creep and strain rate experiments are being conducted on the hydrated films present on the silicon surface in an ambient environment, and these films are expected to be viscoelastic.

27.4.3 Localized Surface Elasticity and Viscoelasticity Mapping

The Young's modulus of elasticity can be calculated from the slope of the indentation curve during unloading. However, these measurements provide a single-point measurement. By using the force modulation technique, it is possible to obtain localized elasticity maps of soft and compliant materials of near-surface regions with nanoscale lateral resolution. This technique has been successfully used for polymeric magnetic tapes, which consist of magnetic and nonmagnetic ce-
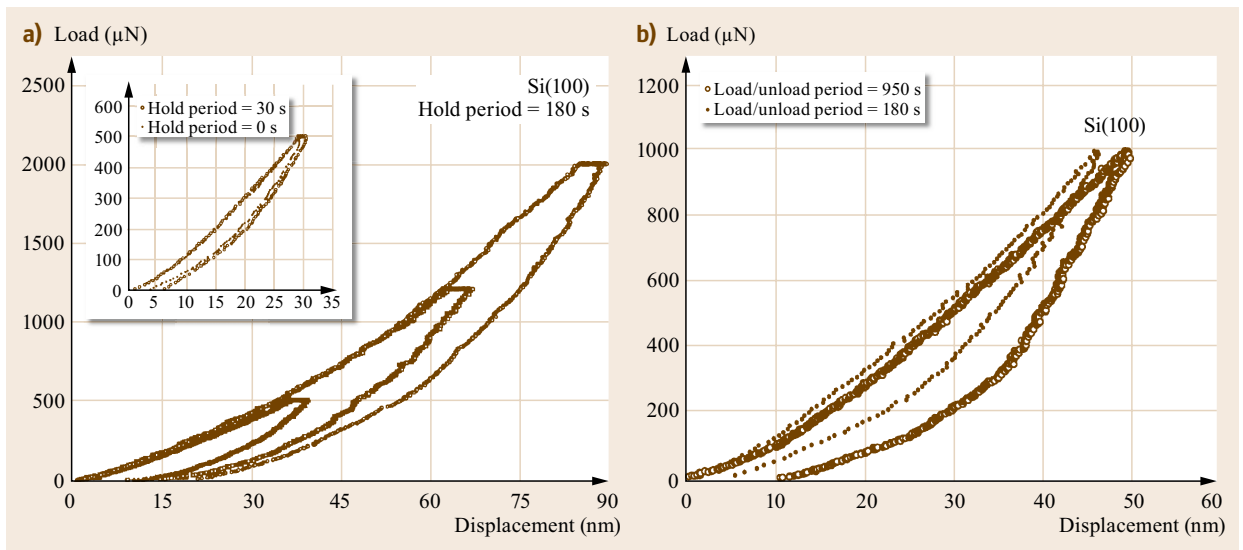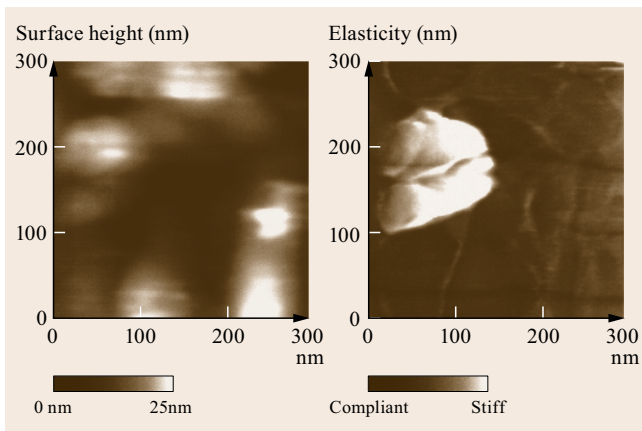

**Fig. 27.60 (a)** Creep behavior and **(b)** strain-rate sensitivity of Si(100) (after [27.60])

Fig. 27.61 Surface height and elasticity maps on a polymeric magnetic tape ($\sigma = 6.7$ nm and P–V $= 32$ nm; σ and P–V refer to standard deviation of surface heights and peak-to-valley distance, respectively). The gray scale on the elasticity map is arbitrary (after [27.66])

ramic particles in a polymeric matrix. Elasticity maps of a tape can be used to identify the relative distribution of the hard magnetic and nonmagnetic ceramic particles on the tape surface, which has an effect on friction and stiction at the head–tape interface [27.16]. Figure 27.61 shows the surface height and elasticity maps on a polymeric magnetic tape [27.66]. The elasticity image reveals sharp variations in the surface elasticity due to the composite nature of the film. As can be clearly seen, regions of high elasticity do not always correspond to high or low topography. On the basis of a Hertzian elastic-contact analysis, the static indentation depth of these samples during the force modulation scan is estimated to be about 1 nm. We con-

clude that the contrast seen is influenced most strongly by material properties in the top few nanometers, independent of the composite structure beneath the surface layer.

By using phase contrast microscopy, it is possible to obtain phase contrast maps or the contrast in viscoelastic properties of near surface regions with nanoscale lateral resolution. This technique has been successfully used for polymeric films and magnetic tapes which consist of ceramic particles in a polymeric matrix [27.69–72].

Figure 27.62 shows typical surface height, TR amplitude, and TR phase angle images for a MP tape using TR mode II, described earlier. The TR amplitude image provides contrast in lateral stiffness, and the TR phase angle image provides contrast in viscoelastic properties. In TR amplitude and phase angle images, the distribution of magnetic particles can be clearly seen and have better contrast than that in the TR surface height image. MP tape samples show a granular structure with elliptically shaped magnetic particle aggregates (50−100 nm in diameter). Studies by *Scott* and *Bhushan* [27.69], *Bhushan* and *Qi* [27.70], and *Kasai* et al. [27.71] have indicated that the phase shift can be related to the energy dissipation through the viscoelastic deformation process between the tip and the sample. Recent theoretical analysis has established a quantitative correlation between the lateral surface properties (stiffness and viscoelasticity) of materials and amplitude/phase angle shift in TR measurements [27.92]. The contrast in the TR amplitude and phase angle images is due to the in-plane (lateral) heterogeneity of the surface. The TR amplitude and phase angle images enable the lateral surface properties (lateral stiffness and viscoelasticity) of materials to be mapped.
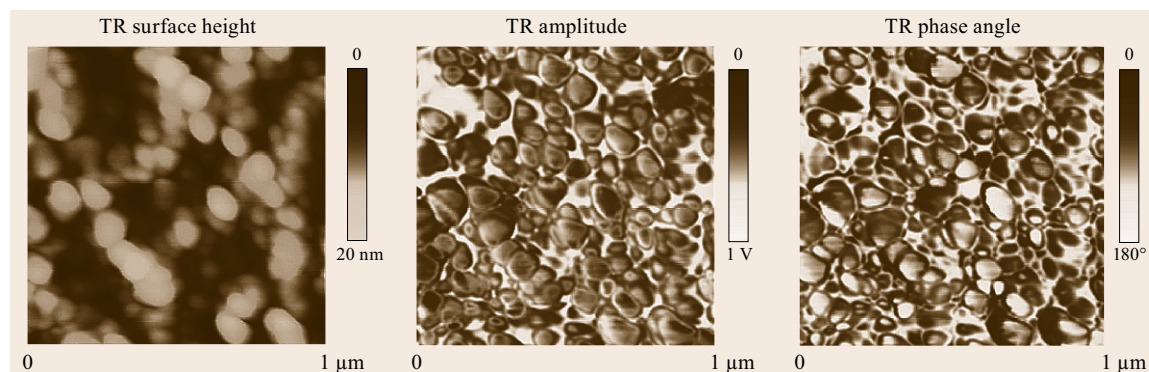

Fig. 27.62 Images of an MP tape obtained with TR mode II (constant deflection). TR mode II amplitude and phase angle images have the largest contrast among tapping, TR mode I, and TR mode II techniques (after [27.72])
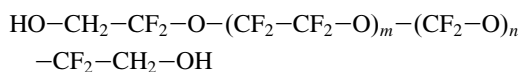
27.5 Boundary Lubrication

27.5.1 Perfluoropolyether Lubricants

The classical approach to lubrication uses freely supported multimolecular layers of liquid lubricants [27.2, 9, 16, 149]. The liquid lubricants are sometimes chemically bonded to improve their wear resistance [27.2, 14, 16, 103, 104]. Partially chemically bonded, molecularly thick perfluoropolyether (PFPE) films are used for the lubrication of magnetic storage media because of their thermal stability and extremely low vapor pressure [27.16]. Chemically bonded lubricants are considered potential candidate lubricants for MEMS/NEMS. Molecularly thick PFPEs are well suited because of the following properties: low surface tension and a low contact angle which allows easy spreading on surfaces and provide hydrophobic properties; chemical and thermal stability which minimizes degradation under use; low vapor pressure which provides low out-gassing; high adhesion to substrate via organic functional bonds; and good lubricity which reduces contact surface wear.

For boundary lubrication studies, friction, adhesion, and durability experiments have been performed on virgin Si(100) surfaces and silicon surfaces lubricated with various PFPE lubricants [27.41–43, 47, 51, 53, 54]. More recently, there has been interest in selected ionic liquids for lubrication [27.150–152]. They possess efficient heat transfer properties. They are also electrically conducting, which is of interest in various MEMS/NEMS applications. Results of the following two PFPE lubricants will be presented here: Z-15 (with $-CF_3$ nonpolar end groups),

$$CF_3-O-(CF_2-CF_2-O)_m-(CF_2-O)_n-CF_3$$
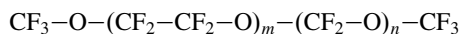
($m/n \approx 2/3$) and Z-DOL (with $-OH$ polar end groups),

$$HO-CH_2-CF_2-O-(CF_2-CF_2-O)_m-(CF_2-O)_n$$
$$-CF_2-CH_2-OH$$

($m/n \approx 2/3$). Z-DOL film was thermally bonded at 150 °C for 30 min, and the unbonded fraction was removed by a solvent (fully bonded) [27.16]. The thicknesses of Z-15 and Z-DOL films were 2.8 nm and 2.3 nm, respectively. The lubricant chain diameter of these molecules is about 0.6 nm, and molecularly thick films generally lie flat on surfaces with high coverage.

The adhesive forces of Si(100), Z-15, and Z-DOL (fully bonded) measured by a force calibration plot and a friction force versus normal load plot are summarized in Fig. 27.63 [27.47]. The data obtained by these two methods are in good agreement. Figure 27.63 shows that the presence of mobile Z-15 lubricant film

increases the adhesive force as compared to that of Si(100) by meniscus formation. Whereas, the presence of the solid-like phase of the Z-DOL (fully bonded) film reduces the adhesive force as compared that of Si(100) because of the absence of mobile liquid. The schematic (bottom) in Fig. 27.63 shows the relative size and sources of the meniscus. It is well known that the native oxide layer (SiO_2) on top of the Si(100) wafer exhibits hydrophilic properties, and some water molecules can be adsorbed on this surface. The condensed water will form a meniscus as the tip approaches the sample surface. The larger adhesive force in Z-15 is not only caused by the Z-15 meniscus alone, the nonpolarized Z-15 liquid does not have good wettability and strong bonding with Si(100). Consequently, in the ambient environment, the condensed water molecules from the environment will permeate through the liquid Z-15 lubricant film and compete with the lubricant molecules present on the substrate. The interaction of the liquid lu-
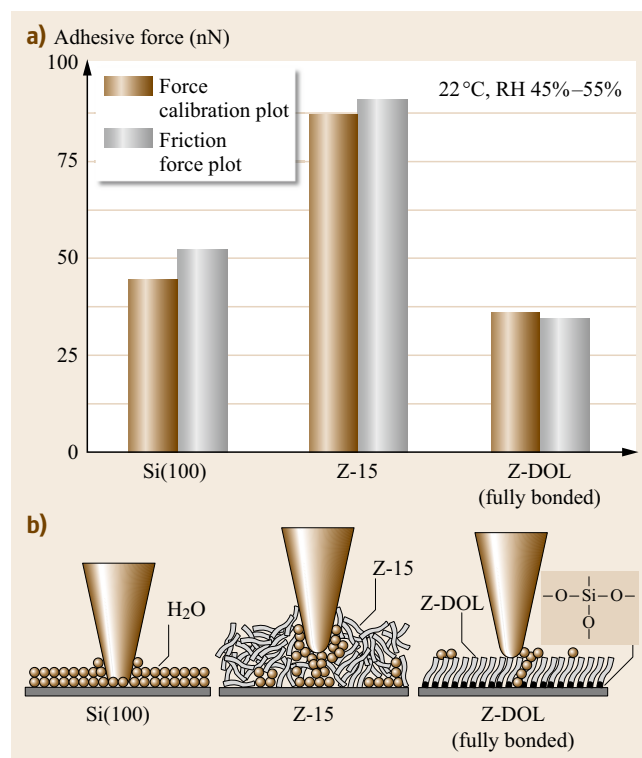

Fig. 27.63a,b Summary of the adhesive forces of Si(100) and Z-15 and Z-DOL (fully bonded) films measured by force calibration plots and friction force versus normal load plots in ambient air **(a)**. **(b)** Schematic showing the effect of the meniscus, formed between the AFM tip and the surface sample, on the adhesive and friction forces (after [27.47])

bricant with the substrate is weakened, and a boundary layer of the liquid lubricant forms puddles [27.42, 43]. This dewetting allows water molecules to be adsorbed on the Si(100) surface along with Z-15 molecules, and both of them can form a meniscus while the tip approaches the surface. Thus, the dewetting of the liquid Z-15 film results in a higher adhesive force and poorer lubrication performance. In addition, the Z-15 film is soft compared to the solid Si(100) surface, and penetration of the tip in the film occurs while pushing the tip down. This results in a large area of the tip being wetted by the liquid to form the meniscus at the tip–liquid (mixture of Z-15 and water) interface. It should also be noted that Z-15 has a higher viscosity compared to water, therefore the Z-15 film provides a higher resistance to motion and the coefficient of friction. In the case of the Z-DOL (fully bonded) film, both of the active groups of Z-DOL molecules are mostly bonded on the Si(100) substrate, thus the Z-DOL (fully bonded) film has low free surface energy and cannot be displaced readily by the water molecules or can readily adsorb the water molecules. Thus, the use of Z-DOL (fully bonded) can reduce the adhesive force.

To study the velocity effect on friction and adhesion, the variation of friction force, the adhesive force, and the coefficient of friction of Si(100), Z-15, and Z-DOL (fully bonded) as a function of velocity are summarized in Fig. 27.64 [27.47]. It indicates that for a silicon wafer, the friction force decreases logarithmically with increasing velocity. For Z-15, the friction force decreases with increasing velocity up to $10\,\mu m/s$, after which it remains almost constant. The velocity has a very small effect on the friction force of Z-DOL (fully bonded); it reduced slightly only at very high velocity. Figure 27.64 also indicates that the adhesive force of Si(100) is increased when the velocity is higher than $10\,\mu m/s$. The adhesive force of Z-15 is reduced dramatically with a velocity increase up to $20\,\mu m/s$, after which it is reduced slightly, and the adhesive force of Z-DOL (fully bonded) is also decreased at high velocity. In the testing range of velocity, only the coefficient of friction of Si(100) decreases with velocity, but the coefficients of friction of Z-15 and Z-DOL (fully bonded) almost remain constant. This implies that the friction mechanisms of Z-15 and Z-DOL (fully bonded) do not change with the variation of velocity.

The mechanisms of the effect of velocity on adhesion and friction are explained based on schematics shown in Fig. 27.65 (right) [27.47]. For Si(100), a tribochemical reaction plays a major role. Although, at high velocity, the meniscus is broken and does not have enough time to rebuild, the contact stresses and high velocity lead to tribochemical reactions of the Si(100) wafer (which has native oxide (SiO_2)) and Si_3N_4 tip

with water molecules and they form $Si(OH)_4$. The $Si(OH)_4$ is removed and continuously replenished during sliding. The $Si(OH)_4$ layer between the tip and the Si(100) surface is known to be of low shear strength and causes a decrease in friction force and coefficient of friction [27.103, 104]. The chemical bonds of Si–
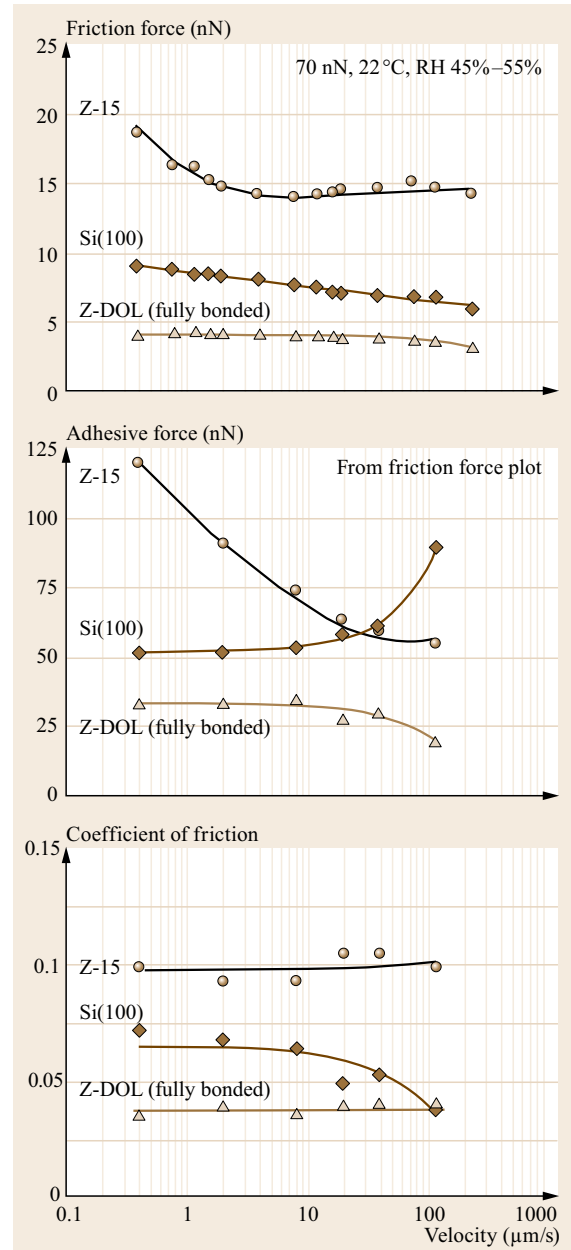
Fig. 27.64 The influence of velocity on the friction force, adhesive force, and coefficient of friction of Si(100) and Z-15 and Z-DOL (fully bonded) films at 70 nN, in ambient air (after [27.47])

OH between the tip and Si(100) surface induce a large adhesive force. For the Z-15 film, at high velocity the meniscus formed by the condensed water and the Z-15 molecules is broken and does not have enough time to rebuild, therefore, the adhesive force and consequently friction force is reduced. The friction mechanisms for the Z-15 film still shear the same viscous liquid even at high velocity range, thus the coefficient of friction of the Z-15 film does not change with velocity. For the Z-DOL (fully bonded) film, the surface can adsorb a few water molecules in an ambient condition, and at high velocity these molecules are displaced, which is responsible for a slight decrease in friction force and adhesive force. *Koinkar* and *Bhushan* [27.42, 43] have suggested that in the case of samples with mobile films, such as condensed water and Z-15 films, alignment of the liquid molecules (shear thinning) is responsible for the drop in friction force with an increase in scanning velocity. This could be another reason for the decrease in friction force for the Si(100) and Z-15 films with velocity in this study.

To study the relative humidity effect on friction and adhesion, the variation of friction force, adhesive force, and the coefficient of friction of Si(100), Z-15, and Z-DOL (fully bonded) as a function of relative hu-

midity are shown in Fig. 27.66 [27.47]. It shows that for Si(100) and Z-15 film, the friction force increases with a relative humidity increase up to 45%, and then it shows a slight decrease with a further increase in the relative humidity. Z-DOL (fully bonded) has a smaller friction force than Si(100) and Z-15 in the whole testing
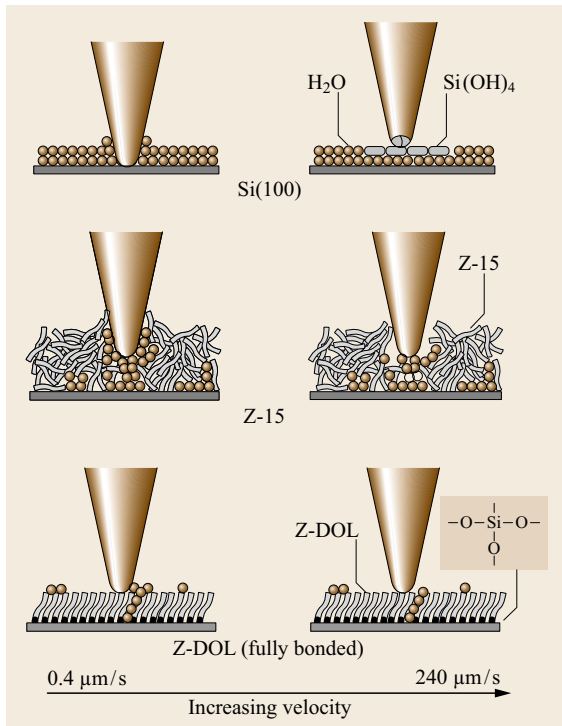
Fig. 27.65 The schematic shows the change of surface composition (by tribochemical reaction) and formation of a meniscus while increasing the velocity (after [27.47])
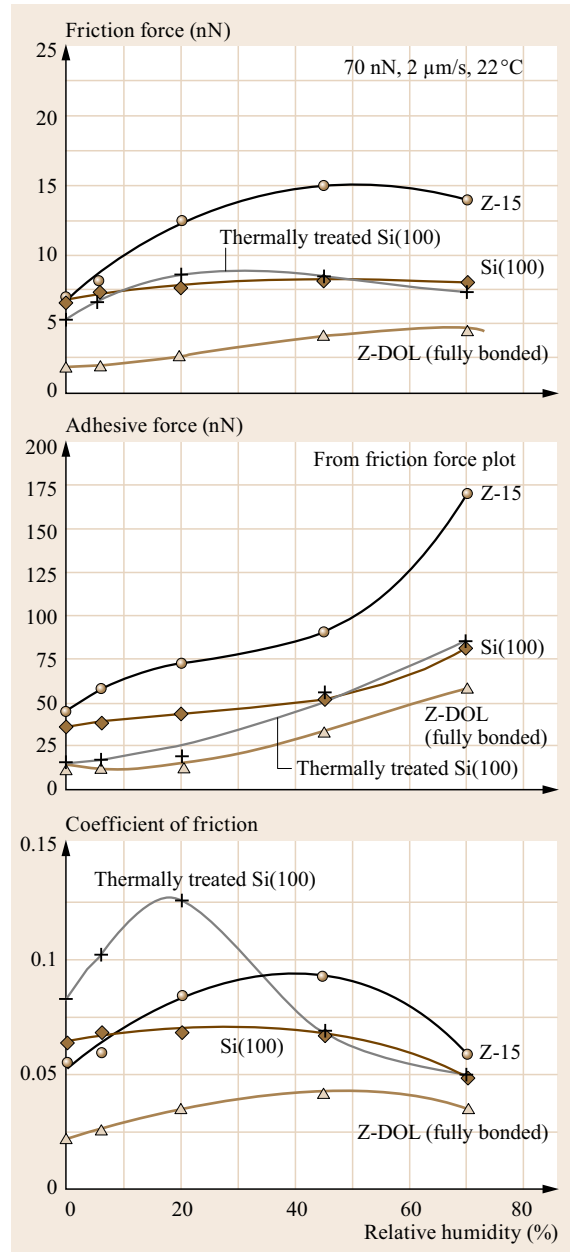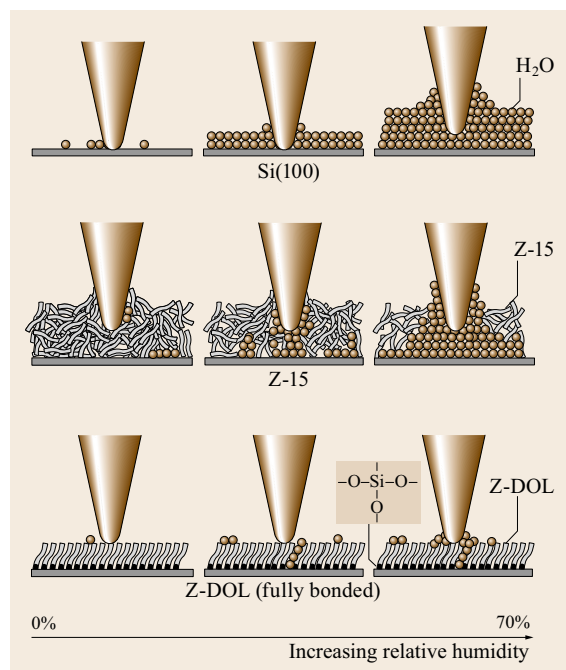

Fig. 27.66 The influence of relative humidity on the friction force, adhesive force, and coefficient of friction of Si(100) and Z-15 and Z-DOL (fully bonded) films at 70 nN, 2 μm/s, and in 22 °C air (after [27.47])

range, and its friction force shows a relative apparent increase when the relative humidity is higher than 45%. For Si(100), Z-15, and Z-DOL (fully bonded), their adhesive forces increase with relative humidity, and their coefficients of friction increase with relative humidity up to 45%, after which they decrease with a further increase in relative humidity. It is also observed that the humidity effect on Si(100) really depends on the history of the Si(100) sample. As the surface of the Si(100) wafer readily adsorbs water in air, without any pretreatment the Si(100) used in our study almost reaches a saturated stage in terms of adsorbed water, and is responsible for less effect during increasing relative humidity. However, once the Si(100) wafer was thermally treated by baking at 150 °C for 1 h, a greater effect was observed.

The schematic (right) in Fig. 27.67 shows that because of its high free surface energy Si(100) can adsorb more water molecules during an increase in relative humidity [27.47]. As discussed earlier, for the Z-15 film in the humid environment, the condensed water from the humid environment competes with the lubricant film present on the sample surface, and the interaction of the liquid lubricant film with the sili-

con substrate is weakened and a boundary layer of the liquid lubricant forms puddles. This dewetting allows water molecules to be adsorbed on the Si(100) substrate mixed with Z-15 molecules [27.42, 43]. Obviously, more water molecules can be adsorbed on the

Fig. 27.67 Schematic shows the change of meniscus while increasing relative humidity. In this figure, the thermally treated Si(100) represents the Si(100) wafer that was baked at 150 °C for 1 h in an oven (in order to remove the adsorbed water) just before it was placed in the 0% RH chamber (after [27.47])
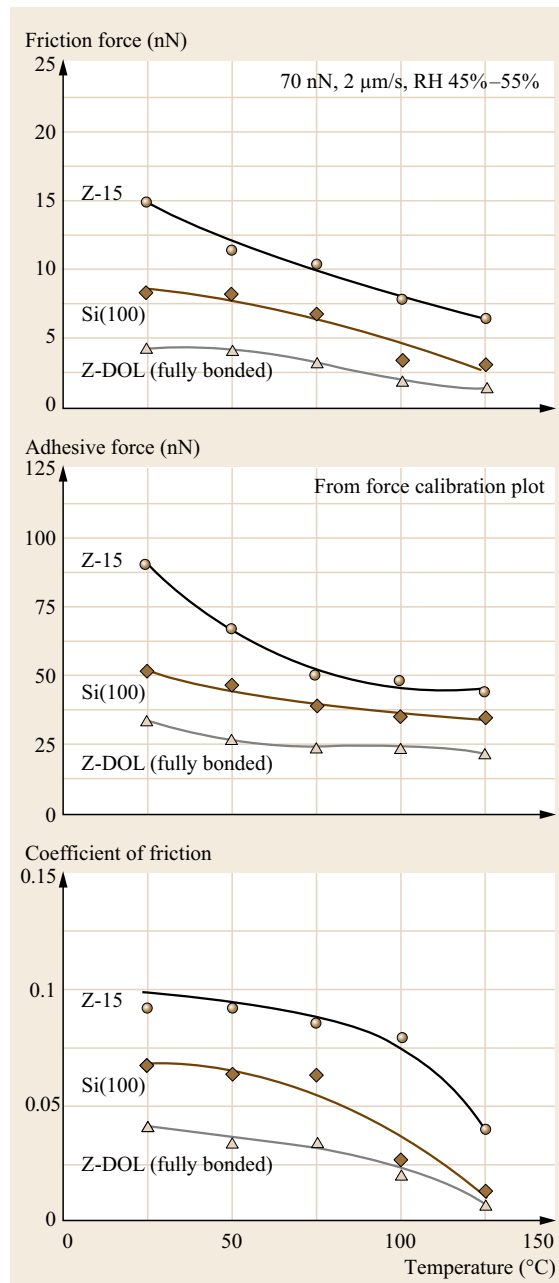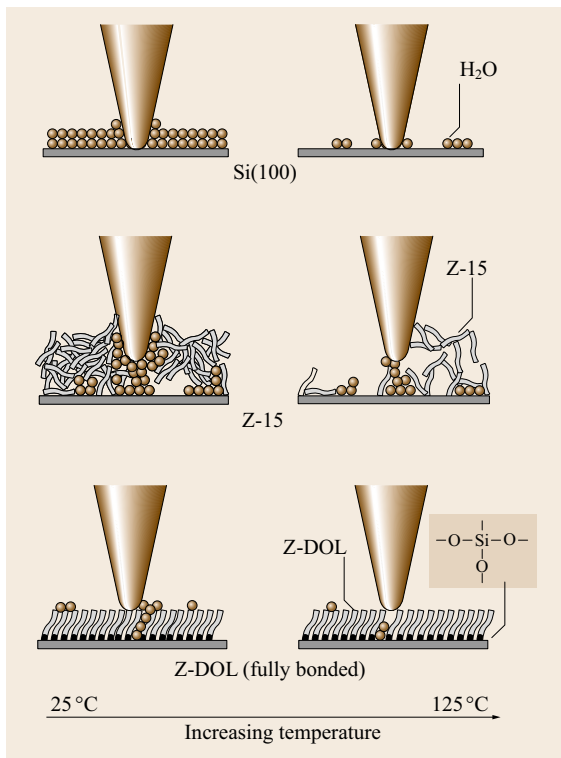

Fig. 27.68 The influence of temperature on the friction force, adhesive force, and coefficient of friction of Si(100) and Z-15 and Z-DOL (fully bonded) films at 70 nN, 2 μm/s, and in RH 40−50% air (after [27.47])

Z-15 surface while increasing relative humidity. The more adsorbed water molecules in the case of Si(100), along with lubricant molecules in the Z-15 film case, form a bigger water meniscus which leads to an increase of friction force, adhesive force, and coefficient of friction of Si(100) and Z-15 with humidity, but at a very high humidity of 70%, large quantities of adsorbed water can form a continuous water layer that separates the tip and sample surface and acts as a kind of lubricant, which causes a decrease in the friction force and the coefficient of friction. For the Z-DOL (fully bonded) film, because of their hydrophobic surface properties, water molecules can be adsorbed at humidity higher than 45%, and cause an increase in the adhesive force and friction force.

To study the temperature effect on friction and adhesion, the variation of friction force, adhesive force, and coefficient of friction of Si(100), Z-15, and Z-DOL (fully bonded) as a function of temperature are summarized in Fig. 27.68 [27.47]. It shows that the increasing temperature causes a decrease of friction force, adhesive force, and coefficient of friction of Si(100), Z-15, and Z-DOL (fully bonded). The schematic (right) in Fig. 27.69 indicates that at high temperature, desorption of water leads to a decrease of the friction force, the adhesive forces, and the coefficient of friction for all samples. For the Z-15 film, the reduction of viscosity at high temperature also has a contribution to the decrease of friction force and coefficient of friction. In the case of the Z-DOL (fully bonded) film, molecules can be more easily oriented at high temperature, which

Fig. 27.69 The schematic shows that at high temperature, desorption of water decreases the adhesive forces. And the reduced viscosity of Z-15 leads to the decrease of coefficient of friction. High temperature facilitates orientation of molecules in the Z-DOL (fully bonded) film which results in a lower coefficient of friction (after [27.47])
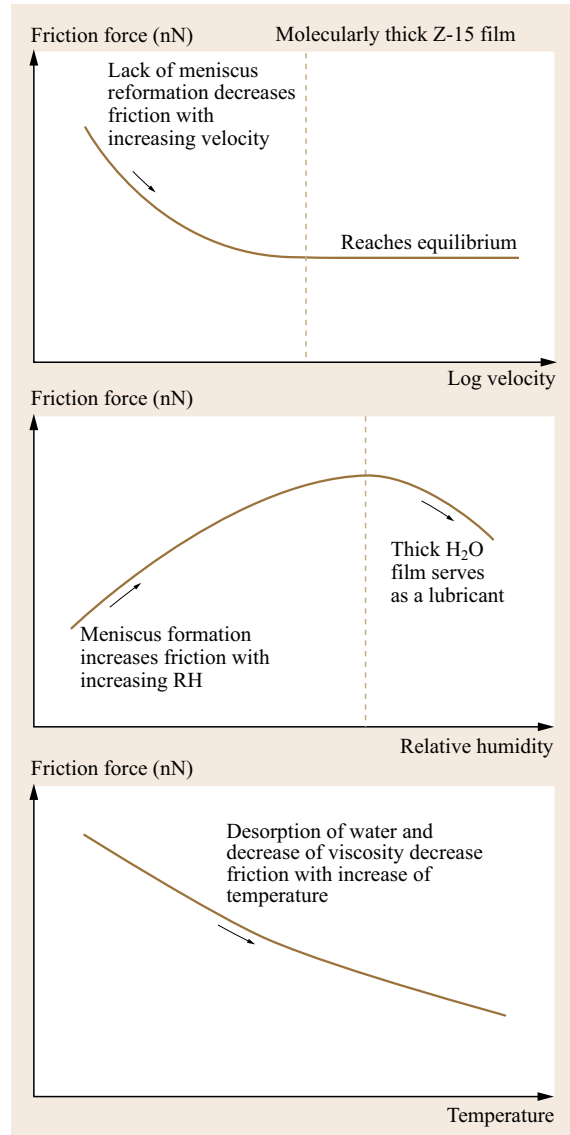
Fig. 27.70 Schematic shows the change of friction force of molecularly thick Z-15 films with log velocity, relative humidity, and temperature. The changing trends are also addressed in this figure (after [27.47])

may be partly responsible for the low friction force and coefficient of friction.

As a brief summary, the influence of velocity, relative humidity, and temperature on the friction force of a mobile Z-15 film is presented in Fig. 27.70 [27.47]. The changing trends are also addressed in this figure.

To study the durability of lubricant films at the nanoscale, the friction of Si(100), Z-15, and Z-DOL (fully bonded) as a function of the number of scanning cycles are shown in Fig. 27.71 [27.47]. As observed earlier, the friction force of Z-15 is higher than that of Si(100) with the lowest values for Z-DOL (fully bonded). During cycling, the friction force and the coefficient of friction of Si(100) show a slight decrease during the initial few cycles then remain constant. This is related to the removal of the native oxide. In the case of the Z-15 film, the friction force and coefficient of friction show an increase during the initial few cycles and then approach higher stable values. This is believed to be caused by

the attachment of the Z-15 molecules to the tip. After several scans, the molecular interaction reaches equilibrium, and after that the friction force and coefficient of friction remain constant. In the case of the Z-DOL (fully bonded) film, the friction force and coefficient of friction start out low and remain low during the entire test for 100 cycles. This suggests that Z-DOL (fully bonded) molecules do not become attached or displaced as readily as Z-15.
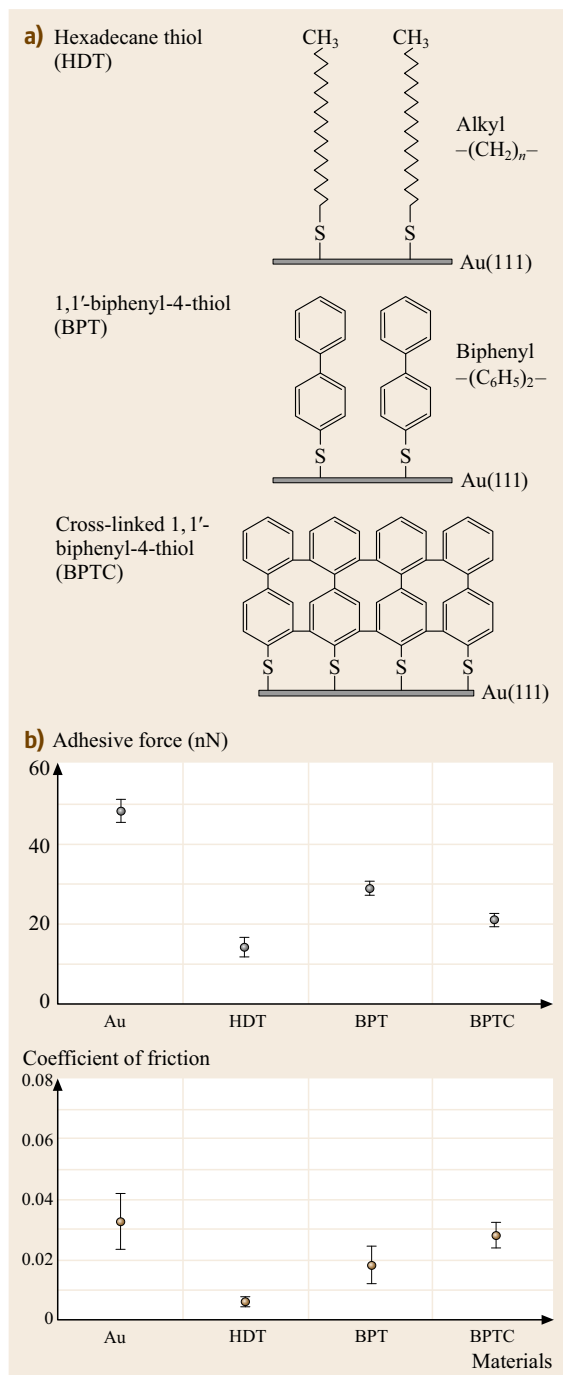
27.5.2 Self-Assembled Monolayers

For the lubrication of MEMS/NEMS, another effective approach involves the deposition of organized and dense molecular layers of long-chain molecules. Two common methods to produce monolayers and thin films are Langmuir–Blodgett (L–B) deposition and self-assembled monolayers (SAMs) by chemical grafting of molecules. LB films are physically bonded to the substrate by weak van der Waals attraction, while SAMs are chemically bonded via covalent bonds to the substrate. Because of the choice of chain length and terminal linking group that SAMs offer, they hold great promise for boundary lubrication of MEMS/NEMS. A number of studies have been conducted to study the tribological properties of various SAMs deposited on Si, Al, and Cu substrates [27.20, 39–41, 44–46, 48–50, 111, 153–159].

Bhushan and *Liu* [27.44] studied the effect of film compliance on adhesion and friction. They used hexadecane thiol (HDT), 1,1′-biphenyl-4-thiol (BPT), and crosslinked BPT (BPTC) solvent deposited on an Au(111) substrate (Fig. 27.72a). The average values and standard deviation of the adhesive force and coefficient of friction are presented in Fig. 27.72b. On the basis of this data, the adhesive force and coefficient of friction of SAMs are less than the corresponding substrates. Among various films, HDT exhibits the lowest values. Based on the stiffness measurements of various SAMs, HDT was most compliant, followed by BPT and BPTC. On the basis of friction and stiffness measurements, SAMs with high-compliance long carbon chains exhibit low friction; chain compliance is desirable for low friction. The friction mechanism of SAMs is explained by a so-called *molecular spring* model (Fig. 27.73). According to this model, the chemically adsorbed self-assembled molecules on a substrate are like assembled molecular springs anchored to the substrate. An asperity sliding on the surface of SAMs is like a tip sliding on the top of the *molecular springs or brush*. The molecular spring assembly has compliant features and can experience orientation and compression under load. The orientation of the molecular springs or brush under normal load reduces the shearing force at
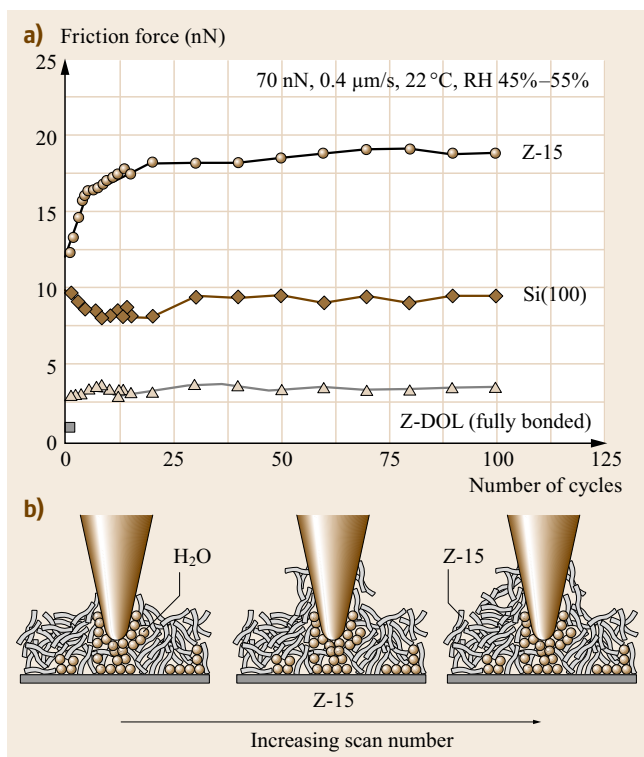
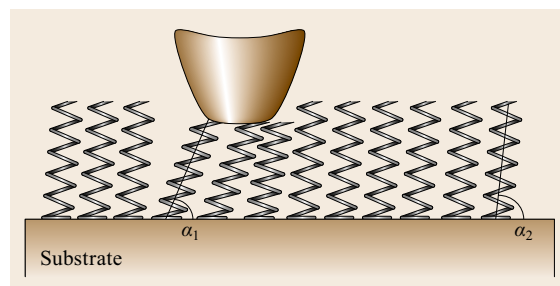**Fig. 27.71 (a)** Friction force versus number of sliding cycles for Si(100) and Z-15 and Z-DOL (fully bonded) films at 70 nN, 0.8 μm/s, and in ambient air. **(b)** Schematic shows that some liquid Z-15 molecules can be attached to the tip. The molecular interaction between the molecules attached to the tip with the Z-15 molecules in the film results in an increase of friction force with multiscanning (after [27.47])

a) Hexadecane thiol
(HDT)

CH₃   CH₃

Alkyl
$-(CH_2)_n-$

S   S
Au(111)

1,1′-biphenyl-4-thiol
(BPT)

Biphenyl
$-(C_6H_5)_2-$

S   S
Au(111)

Cross-linked 1,1′-
biphenyl-4-thiol
(BPTC)

S   S   S   S
Au(111)

b) Adhesive force (nN)

Au   HDT   BPT   BPTC

Coefficient of friction

Au   HDT   BPT   BPTC
Materials

Fig. 27.72 (a) Schematics of structures of hexadecane thiol and biphenyl thiol SAMs on Au(111) substrates, and **(b)** adhesive force and coefficient of friction of Au(111) substrate and various SAMs (after [27.44]) ◄
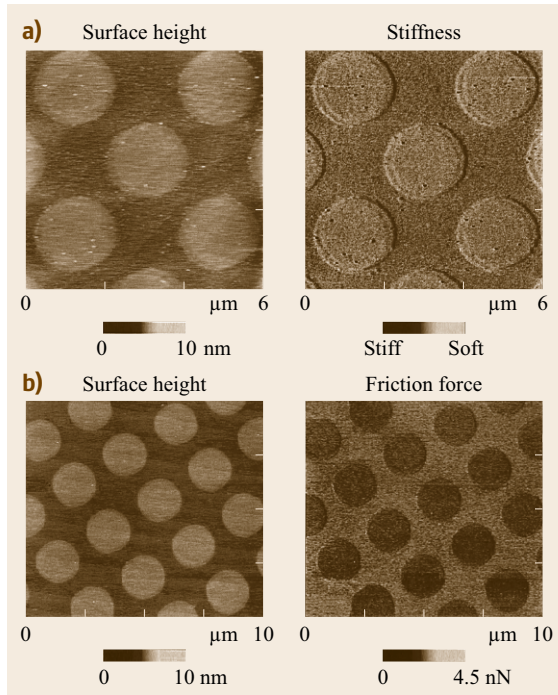

Fig. 27.73 Molecular spring model of SAMs. In this figure, $\alpha_1 < \alpha_2$, which is caused by further orientation under the normal load applied by an asperity tip (after [27.44])

fects along the molecular chains, which lead to energy dissipation.

An elegant way to demonstrate the influence of molecular stiffness on friction is to investigate SAMs with different structures on the same wafer. For this purpose, a micropatterned SAM was prepared. First, the biphenyldimethylchlorosilane (BDCS) was deposited on silicon by a typical self-assembly method [27.46]. Then the film was partially crosslinked using a mask technique with low-energy electron irradiation. Finally, the micropatterned BDCS films were realized, which had the as-deposited and crosslinked coating regions on the same wafer. The local stiffness properties of this micropatterned sample were investigated by the force-modulation AFM technique [27.66]. The variation in the deflection amplitude provides a measure of the relative local stiffness of the surface. Surface height, stiffness, and friction images of the micropatterned BDCS specimen were obtained and are presented in Fig. 27.74 [27.46]. The circular areas correspond to the as-deposited film, and the remaining area to the crosslinked film. Figure 27.74a indicates that crosslinking caused by the low-energy electron irradiation leads to about 0.5 nm decrease of the surface height of BDCS films. The corresponding stiffness images indicate that the crosslinked area has a higher stiffness than the as-deposited area. Figure 27.74b indicates that the as-deposited area (higher surface height area) has a lower friction force. Obviously, these data of the micropatterned sample prove that the local stiffness of SAMs has an influence on their friction performance. Higher stiffness leads to larger friction force. These results provide strong proof of the suggested molecular spring model.

The SAMs with high-compliance long carbon chains also exhibit the best wear resistance [27.44, 46].

the interface, which in turn reduces the friction force. The orientation is determined by the spring constant of a single molecule as well as by the interaction between the neighboring molecules, which can be reflected by the packing density or the packing energy. It should be noted that the orientation can lead to conformational de-

Fig. 27.74 (a) AFM gray-scale surface height and stiffness images, and **(b)** AFM gray-scale surface height and friction force images of micropatterned BDCS (after [27.46])

In wear experiments, the wear depth as a function of normal load curves shows a critical normal load, at which the film wears rapidly. A representative curve is shown in Fig. 27.75. Below the critical normal load, SAMs undergo orientation; at the critical load SAMs wear away from the substrate due to the relatively weak interface bond strengths, while above the critical normal load severe wear takes place on the substrate.

27.5.3 Liquid Film Thickness Measurements

Liquid film thickness mapping of ultrathin films (on the order of 2 nm) can be obtained using friction force microscopy [27.42] and adhesive force mapping [27.125]. Figure 27.76 shows the gray-scale plots of the surface topography and friction force obtained simultaneously for unbonded Demnum S-100-type PFPE lubricant film on silicon. Demnum-type PFPE lubricant (Demnum, Daikin, Japan) chains have $-CF_2-CH_2-OH$, a reactive end group on one end, whereas Z-DOL chains have the hydroxyl groups on both ends, as described earlier. The friction force plot shows well-distinguished low and high friction regions roughly corresponding to high and low regions in surface topography (thick and thin lubricant regions). A uniformly lubricated sample does not show such a variation in the friction.
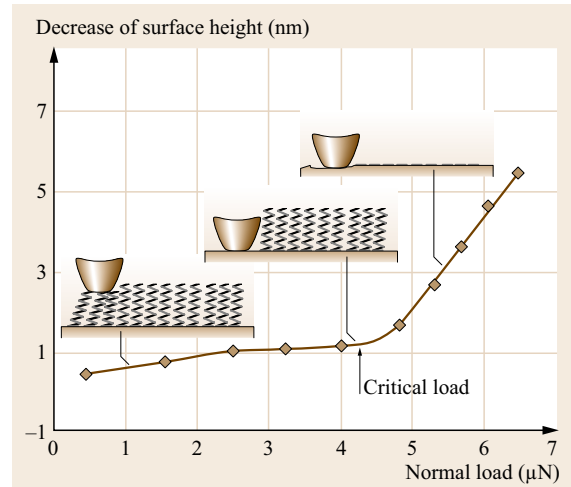
Fig. 27.75 Illustration of the wear mechanism of SAMs with increasing normal load (after [27.46])
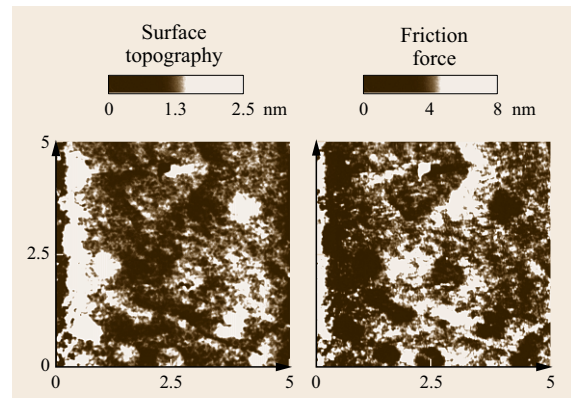
Fig. 27.76 Gray-scale plots of the surface topography and friction force obtained simultaneously for an unbonded Demnum-type perfluoropolyether lubricant film on silicon (after [27.42])

Friction force imaging can thus be used to measure the lubricant uniformity on the sample surface, which cannot be identified by surface topography alone. Figure 27.77 shows the gray-scale plots of the adhesive force distribution for silicon samples coated uniformly and nonuniformly with Z-DOL-type PFPE lubricant. It can be clearly seen that a region exists that has an adhesive force distinctly different from the other region for the nonuniformly coated sample. This implies that the liquid film thickness is nonuniform, giving rise to a difference in the meniscus forces.

Quantitative measurements of liquid film thickness of thin lubricant films (on the order of a few nm) with nanometer lateral resolution can be made with the AFM [27.2, 14, 72, 105]. The liquid film thickness is
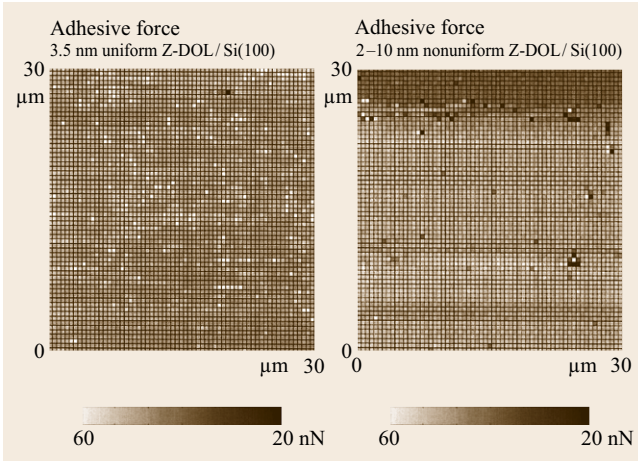
Fig. 27.77 Gray-scale plots of the adhesive force distribution of a uniformly coated, 3.5 nm thick unbonded Z-DOL film on silicon and 3−10 nm thick unbonded Z-DOL film on silicon that was deliberately coated nonuniformly by vibrating the sample during the coating process (after [27.125])

obtained by measuring the force on the tip as it approaches, contacts, and pushes through the liquid film and ultimately contacts the substrate. The distance be-

tween the sharp snap-in (owing to the formation of a liquid meniscus and van der Waals forces between the film and the tip) at the liquid surface and the hard repulsion at the substrate surface is a measure of the liquid film thickness. Figure 27.78 shows a plot of forces between the tip and both virgin hair and conditioner-treated hair. The hair sample was first brought into contact with the tip and then pulled away at a velocity of 400 nm/s. The zero tip–sample separation is defined to be the position where the force on the tip is zero, and the tip is not in contact with the sample. As the tip approaches the sample, a negative force exists which indicates an attractive force. The treated hair surface shows a much longer range of interaction with the tip compared to the very short range of interaction between virgin hair surfaces and the tip. Typically, the tip suddenly snaps into contact with the conditioner layer at a finite separation H (about 30 nm), which is proportional to conditioner thickness h. As the tip contacts the substrate, the tip travels with the sample. When the sample is withdrawn, the forces on the tip slowly decrease to zero once the meniscus of liquid is drawn out from the hair surface. It should be noted that the distance H between the sharp snap-in at the liquid surface and the hard wall contact with the substrate is not the real conditioner thickness h. Because of interaction of the liquid with the tip at some spacing distance, H tends to be thicker than the actual film thickness, but can still provide an estimate of the actual film thickness and upper limit of thickness.
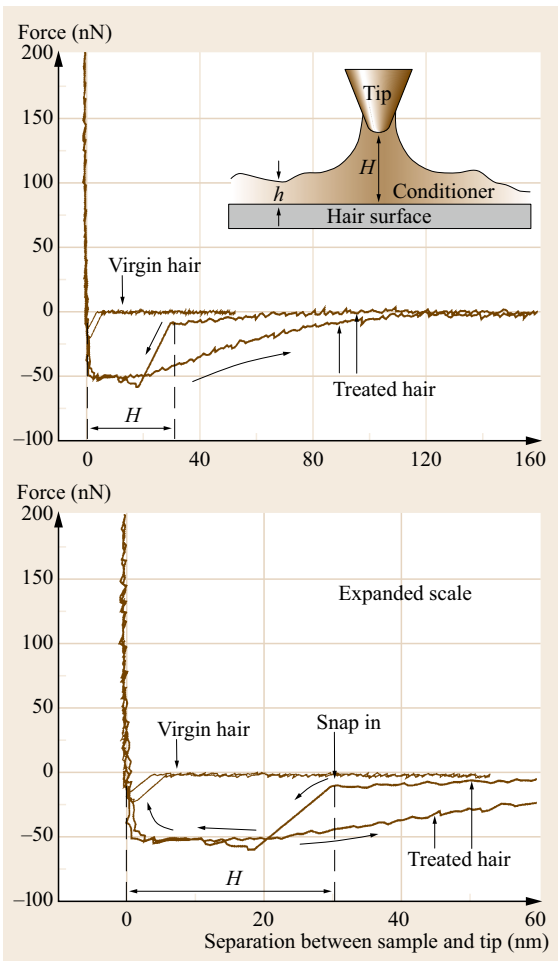
Fig. 27.78 Forces between tip and hair surface as a function of tip–sample separation for virgin hair and conditioner-treated hair. A schematic of measurement for localized conditioner thickness is shown in the *inset at the top*. The expanded scale view of force curve at small separation is shown *at the bottom* (after [27.72]) ◄

27.6 Conclusion

For most solid–solid interfaces of technological relevance, contact occurs at multiple asperities. A sharp AFM/FFM tip sliding on a surface simulates just one such contact. However, asperities come in all shapes and sizes. The effect of the radius of a single asperity (tip) on the friction/adhesion performance can be studied using tips of different radii. AFM/FFM are used to study various tribological phenomena including surface roughness, adhesion, friction, scratching, wear, indentation, detection of material transfer, and boundary lubrication. Measurement of the atomic-scale friction of a freshly cleaved, highly oriented, pyrolytic graphite exhibits the same periodicity as that of the corresponding topography. However, the peaks in friction and those in the corresponding topography are displaced relative to each other. Variations in atomic-scale friction and the observed displacement can be explained by the variation in interatomic forces in the normal and lateral directions. The relevant friction mechanism is atomic-scale stick-slip. Local variations in microscale friction occur and are found to correspond to the local slopes, suggesting that a ratchet mechanism and collision effects are responsible for this variation. Directionality in the friction is observed on both micro- and macroscales which results from the surface roughness and surface preparation. Anisotropy in surface roughness accentuates this effect. Friction contrast in conventional frictional measurements is based on interactions dependent upon interfacial material properties superimposed by roughness-induced lateral forces. To obtain roughness-independent friction, lateral or torsional modulation techniques can be used. These techniques also allow measurements over a small region. AFM/FFM experiments are generally conducted at relative velocities up to about $200\,\mu m/s$. High-velocity experiments can be performed by either mounting a sample on a shear wave transducer driven at very high frequencies or mounting a sample on a high-velocity piezo stage. By using these techniques, friction and wear experiments can be performed at a range of sliding velocities as well as normal loads, and the data have been used to develop nanoscale friction and wear maps. Relevant friction mechanisms are different for different ranges of sliding velocities and normal loads.

Adhesion and friction in a wet environment depend on the tip radius, surface roughness, and relative humidity. Superhydrophobic surfaces can be designed by roughness optimization.

Nanoscale friction is generally found to be smaller than microscale friction. There are several factors responsible for the differences including wear and contaminant particles, the transition from elasticity to plas-

ticity, scale-dependent roughness and mechanical properties, and meniscus effects. Nanoscale friction values increase with an increase in the normal load above a certain critical load (pressure), approaching the macroscale friction. The critical contact pressure corresponds to the hardness of the softer of the two contacting materials.

The wear rate on the microscale for single-crystal silicon is negligible below $20\,\mu N$, and is much higher and remains approximately constant at higher loads. Elastic deformation at low loads is responsible for negligible wear. Most of the wear debris is loose. SEM and TEM studies of the wear region suggest that the material on the microscale is removed by plastic deformation with a small contribution from elastic fracture; this observation corroborates with the scratch data. Evolution of wear has also been studied using AFM. Wear is found to be initiated at nanoscratches. For a sliding interface requiring near-zero friction and wear, contact stresses should be below the hardness of the softer material to minimize plastic deformation and surfaces should be free of nanoscratches. Further, wear precursors can be detected at early stages of wear by using surface potential measurements. It is found that even in the case of zero wear (no measurable deformation of the surface using AFM), there can be a significant change in the surface potential inside the wear mark, which is useful for the study of wear precursors. Detection of material transfer on a nanoscale is possible with AFM.

In situ surface characterization of the local deformation of materials and thin coatings can be carried out using a tensile stage inside an AFM. An AFM can also be used for nanofabrication/nanomachining.

A modified AFM can be used to obtain load–displacement curves and for the measurement of nanoindentation hardness and Young's modulus of elasticity, with a depth of indentation as low as 1 nm. A continuous stiffness technique can be used to measure variations in mechanical properties of layered materials and nonhomogeneous composites. Mechanical properties are scale-dependent. For example, hardness of ceramics on nanoscales is found to be higher than that on the microscale. Ceramics exhibit significant plasticity and creep on a nanoscale. By using the force modulation technique, localized surface elasticity maps of composite materials with penetration depth as low as 1 nm can be obtained. By using phase contrast microscopy in tapping or torsional mode, it is possible to obtain phase contrast maps or the contrast in viscoelastic properties of near-surface regions. Scratching and indentation on the nanoscale are powerful ways to screen for adhesion and resistance to deformation of ultrathin films.

Boundary lubrication studies and measurement of lubricant-film thickness with a lateral resolution on the nanoscale can be conducted using AFM. Chemically bonded lubricant films and self-assembled monolayers are superior in friction and wear resistance. For chemically bonded lubricant films, the adsorption of water, formation of meniscus and its changes during sliding, and surface properties play an important role in regard to the adhesion, friction, and durability of these films. Sliding velocity, relative humidity, and temperature affect adhesion and friction. For SAMs, their friction mechanism is explained by a so-called *molecular spring* model. Films with high-compliance, long carbon chains exhibit low friction and wear. Also, perfluoroalkylsilane SAMs on Si appear to be more hy-

drophobic with lower adhesion than alkylsilane SAMs on Si.

Investigations of adhesion, friction, wear, scratching, and indentation on the nanoscale using an AFM can provide insight into the failure mechanisms of materials. Coefficients of friction, wear rates, and mechanical properties such as hardness have been found to be different on the nanoscale than on the macroscale; generally, the coefficients of friction and wear rates on micro- and nanoscales are smaller, whereas the hardness is greater. Therefore, nanotribological studies may help define the regimes for ultralow friction and near-zero wear. These studies also provide insight into the atomic origins of adhesion, friction, wear, and lubrication mechanisms.

References

27.1 B. Bhushan, J.N. Israelachvili, U. Landman: Nanotribology: Friction, wear and lubrication at the atomic scale, Nature **374**, 607–616 (1995)
27.2 B. Bhushan: *Handbook of Micro/Nanotribology*, 2nd edn. (CRC, Boca Raton 1999)
27.3 B. Bhushan: *Micro/Nanotribology and its Applications*, Nato Science, Vol. 330 (Kluwer, Dordrecht 1997)
27.4 I.L. Singer, H.M. Pollock: *Fundamentals of Friction: Macroscopic and Microscopic Processes*, Nato Science Series, Vol. E220 (Kluwer, Dordrecht 1992)
27.5 H.J. Guntherodt, D. Anselmetti, E. Meyer: *Forces in Scanning Probe Methods*, Vol. E286 (Kluwer, Dordrecht 1995)
27.6 B.N.J. Persson, E. Tosatti: *Physics of Sliding Friction*, Nato Science, Vol. E311 (Kluwer, Dordrecht 1996)
27.7 B. Bhushan: Nanoscale tribophysics and tribomechanics, Wear **225–229**, 465–492 (1999)
27.8 B. Bhushan: Wear and mechanical characterisation on micro- to picoscales using AFM, Int. Mater. Rev. **44**, 105–117 (1999)
27.9 B. Bhushan: *Modern Tribology Handbook: Principles of Tribology*, Vol. 1 (CRC, Boca Raton 2001)
27.10 B. Bhushan: *Fundamentals of Tribology and Bridging the Gap Between the Macro- and Micro/Nanoscales*, NATO Science Series II, Vol. 10 (Kluwer, Dordrecht 2001)
27.11 B. Bhushan: Nano- to microscale wear and mechanical characterization studies using scanning probe microscopy, Wear **251**, 1105–1123 (2001)
27.12 B. Bhushan: Nanotribology and nanomechanics, Wear **259**, 1507–1531 (2005)
27.13 B. Bhushan: Nanotribology, nanomechanics and nanomaterials characterization, Philos. Trans. R. Soc. A **366**, 1351–1381 (2008)
27.14 B. Bhushan: *Nanotribology and Nanomechanics – An Introduction*, 4th edn. (Springer International, Cham 2017)
27.15 B. Bhushan: *Encyclopedia of Nanotechnology*, 2nd edn. (Springer, Cham 2016)
27.16 B. Bhushan: *Tribology and Mechanics of Magnetic Storage Devices*, 2nd edn. (Springer, New York 1996)
27.17 B. Bhushan: *Tribology Issues and Opportunities in MEMS* (Kluwer, Dordrecht 1998)
27.18 B. Bhushan: Chemical, mechanical and tribological characterization of ultra-thin and hard amorphous carbon coatings as thin as 3.5 nm: Recent developments, Diam. Relat. Mater. **8**, 1985–2015 (1999)
27.19 B. Bhushan: Adhesion and stiction: Mechanisms, measurement techniques, and methods for reduction, J. Vac. Sci. Technol. B **21**, 2262–2296 (2003)
27.20 B. Bhushan, A.V. Kulkarni, V.N. Koinkar, M. Boehm, L. Odoni, C. Martelet, M. Belin: Microtribological characterization of self-assembled and Langmuir–Blodgett monolayers by atomic and friction force microscopy, Langmuir **11**, 3189–3198 (1995)
27.21 G. Binnig, C.F. Quate, C. Gerber: Atomic force microscopy, Phys. Rev. Lett. **56**, 930–933 (1986)
27.22 G. Binnig, C. Gerber, E. Stoll, T.R. Albrecht, C.F. Quate: Atomic resolution with atomic force microscope, Europhys. Lett. **3**, 1281–1286 (1987)
27.23 C.M. Mate, G.M. McClelland, R. Erlandsson, S. Chiang: Atomic-scale friction of a tungsten tip on a graphite surface, Phys. Rev. Lett. **59**, 1942–1945 (1987)
27.24 B. Bhushan, J. Ruan: Atomic-scale friction measurements using friction force microscopy: Part II – Application to magnetic media, ASME J. Tribol. **116**, 389–396 (1994)
27.25 J. Ruan, B. Bhushan: Atomic-scale friction measurements using friction force microscopy: Part I – general principles and new measurement techniques, ASME J. Tribol. **116**, 378–388 (1994)

27.26 J. Ruan, B. Bhushan: Atomic-scale and microscale friction of graphite and diamond using friction force microscopy, J. Appl. Phys. **76**, 5022–5035 (1994)

27.27 J. Ruan, B. Bhushan: Frictional behavior of highly oriented pyrolytic graphite, J. Appl. Phys. **76**, 8117–8120 (1994)

27.28 B. Bhushan, V.N. Koinkar, J. Ruan: Microtribology of magnetic media, Proc. Inst. Mech. Eng., Part J: J. Eng. Tribol. **208**, 17–29 (1994)

27.29 B. Bhushan, A.V. Kulkarni: Effect of normal load on microscale friction measurements, Thin Solid Films **278**, 49–56 (1996)

27.30 B. Bhushan, A.V. Kulkarni: Erratum to "Effect of normal load on microscale friction measurement", Thin Solid Films **293**, 333 (1997)

27.31 B. Bhushan, S. Sundararajan: Micro/nanoscale friction and wear mechanisms of thin films using atomic force and friction force microscopy, Acta Mater. **46**, 3793–3804 (1998)

27.32 V. Scherer, W. Arnold, B. Bhushan: Active friction control using ultrasonic vibration. In: *Tribology Issues and Opportunities in MEMS*, ed. by B. Bhushan (Kluwer, Dordrecht 1998) pp. 463–469

27.33 V. Scherer, W. Arnold, B. Bhushan: Lateral force microscopy using acoustic friction force microscopy, Surf. Interface Anal. **27**, 578–587 (1999)

27.34 M. Reinstaedtler, U. Rabe, V. Scherer, U. Hartmann, A. Goldade, B. Bhushan, W. Arnold: On the nanoscale measurement of friction using atomic-force microscope cantilever torsional resonances, Appl. Phys. Lett. **82**, 2604–2606 (2003)

27.35 M. Reinstaedtler, U. Rabe, A. Goldade, B. Bhushan, W. Arnold: Investigating ultra-thin lubricant layers using resonant friction force microscopy, Tribol. Int. **38**, 533–541 (2005)

27.36 M. Reinstaedtler, T. Kasai, U. Rabe, B. Bhushan, W. Arnold: Imaging and measurement of elasticity and friction using the TR mode, J. Phys. D **38**, R269–R282 (2005)

27.37 B. Bhushan, T. Kasai: A surface topography-independent friction measurement technique using torsional resonance mode in an AFM, Nanotechnology **15**, 923–935 (2004)

27.38 N.S. Tambe, B. Bhushan: A new atomic force microscopy based technique for studying nanoscale friction at high sliding velocities, J. Phys. D: Appl. Phys. **38**, 764–773 (2005)

27.39 B. Bhushan, T. Kasai, G. Kulik, L. Barbieri, P. Hoffmann: AFM study of perfluorosilane and alkylsilane self-assembled monolayers for anti-stiction in MEMS/NEMS, Ultramicroscopy **105**, 176–188 (2005)

27.40 B. Bhushan, D. Hansford, K.K. Lee: Surface modification of silicon and polydimethylsiloxane surfaces with vapor-phase-deposited ultrathin fluorosilane films for biomedical nanodevices, J. Vac. Sci. Technol. A **24**, 1197–1202 (2006)

27.41 B. Bhushan, M. Cichomski, Z. Tao, N.T. Tran, T. Ethen, C. Merton, R.E. Jewett: Nanotribological characterization and lubricant degradation studies of metal-film magnetic tapes using novel

lubricants, ASME J. Tribol. **129**, 621–627 (2007)

27.42 V.N. Koinkar, B. Bhushan: Micro/nanoscale studies of boundary layers of liquid lubricants for magnetic disks, J. Appl. Phys. **79**, 8071–8075 (1996)

27.43 V.N. Koinkar, B. Bhushan: Microtribological studies of unlubricated and lubricated surfaces using atomic force/friction force microscopy, J. Vac. Sci. Technol. A **14**, 2378–2391 (1996)

27.44 B. Bhushan, H. Liu: Nanotribological properties and mechanisms of alkylthiol and biphenyl thiol self-assembled monolayers studied by AFM, Phys. Rev. B **63**, 245412-1–245412-11 (2001)

27.45 H. Liu, B. Bhushan, W. Eck, V. Staedtler: Investigation of the adhesion, friction, and wear properties of biphenyl thiol self-assembled monolayers by atomic force microscopy, J. Vac. Sci. Technol. A **19**, 1234–1240 (2001)

27.46 H. Liu, B. Bhushan: Investigation of nanotribological properties of self-assembled monolayers with alkyl and biphenyl spacer chains, Ultramicroscopy **91**, 185–202 (2002)

27.47 H. Liu, B. Bhushan: Nanotribological characterization of molecularly-thick lubricant films for applications to MEMS/NEMS by AFM, Ultramicroscopy **97**, 321–340 (2003)

27.48 T. Kasai, B. Bhushan, G. Kulik, L. Barbieri, P. Hoffmann: Nanotribological study of perfluorosilane SAMs for anti-stiction and low wear, J. Vac. Sci. Technol. B **23**, 995–1003 (2005)

27.49 K.K. Lee, B. Bhushan, D. Hansford: Nanotribological characterization of perfluoropolymer thin films for biomedical micro/nanoelectromechanical systems applications, J. Vac. Sci. Technol. A **23**, 804–810 (2005)

27.50 N.S. Tambe, B. Bhushan: Nanotribological characterization of self assembled monolayers deposited on silicon and aluminum substrates, Nanotechnology **16**, 1549–1558 (2005)

27.51 Z. Tao, B. Bhushan: Bonding, degradation, and environmental effects on novel perfluoropolyether lubricants, Wear **259**, 1352–1361 (2005)

27.52 Z. Tao, B. Bhushan: Degradation mechanisms and environmental effects on perfluoropolyether, self assembled monolayers, and diamondlike carbon films, Langmuir **21**, 2391–2399 (2005)

27.53 M. Palacio, B. Bhushan: Surface potential and resistance measurements for detecting wear of chemically-bonded and unbonded molecularly-thick perfluoropolyether lubricant films using atomic force microscopy, J. Colloid Interface Sci. **315**, 261–269 (2007)

27.54 M. Palacio, B. Bhushan: Wear detection of candidate MEMS/NEMS lubricant films using atomic force microscopy-based surface potential measurements, Scr. Mater. **57**, 821–824 (2007)

27.55 B. Bhushan, V.N. Koinkar: Tribological studies of silicon for magnetic recording applications, J. Appl. Phys. **75**, 5741–5746 (1994)

27.56 V.N. Koinkar, B. Bhushan: Microtribological studies of Al_2O_3-TiC, polycrystalline and single-crystal Mn–Zn ferrite and SiC head slider materials, Wear

202, 110–122 (1996)

27.57 V.N. Koinkar, B. Bhushan: Microtribological properties of hard amorphous carbon protective coatings for thin film magnetic disks and heads, Proc. Inst. Mech. Eng. Part J **211**, 365–372 (1997)

27.58 S. Sundararajan, B. Bhushan: Development of a continuous microscratch technique in an atomic force microscope and its application to study scratch resistance of ultra-thin hard amorphous carbon coatings, J. Mater. Res. **16**, 75–84 (2001)

27.59 J. Ruan, B. Bhushan: Nanoindentation studies of fullerene films using atomic force microscopy, J. Mater. Res. **8**, 3019–3022 (1993)

27.60 B. Bhushan, A.V. Kulkarni, W. Bonin, J.T. Wyrobek: Nano/picoindentation measurement using a capacitance transducer system in atomic force microscopy, Philos. Mag. **74**, 1117–1128 (1996)

27.61 B. Bhushan, V.N. Koinkar: Nanoindentation hardness measurements using atomic force microscopy, Appl. Phys. Lett. **64**, 1653–1655 (1994)

27.62 X. Li, B. Bhushan: A review of nanoindentation continuous stiffness measurement technique and its applications, Mater. Charact. **48**, 11–36 (2002)

27.63 B. Bhushan, X. Li: Nanomechanical characterisation of solid surfaces and thin films, Int. Mater. Rev. **48**, 125–164 (2003), (invited)

27.64 P. Maivald, H.J. Butt, S.A.C. Gould, C.B. Prater, B. Drake, J.A. Gurley, V.B. Elings, P.K. Hansma: Using force modulation to image surface elasticities with the atomic force microscope, Nanotechnology **2**, 103–106 (1991)

27.65 B. Anczykowski, D. Kruger, K.L. Babcock, H. Fuchs: Basic properties of dynamic force microscopy with the scanning force microscope in experiment and simulation, Ultramicroscopy **66**, 251–259 (1996)

27.66 D. DeVecchio, B. Bhushan: Localized surface elasticity measurements using an atomic force microscope, Rev. Sci. Instrum. **68**, 4498–4505 (1997)

27.67 U.D. Schwarz, O. Zwoerner, P. Koester, R. Wiesendanger: Friction force spectroscopy in the low-load regime with well-defined tips. In: *Micro/Nanotribology and Its Applications*, ed. by B. Bhushan (Kluwer, Dordrecht 1997) pp. 233–238

27.68 S. Amelio, A.V. Goldade, U. Rabe, V. Scherer, B. Bhushan, W. Arnold: Measurements of elastic properties of ultra-thin diamond-like carbon coatings using atomic force acoustic microscopy, Thin Solid Films **392**, 75–84 (2001)

27.69 W.W. Scott, B. Bhushan: Use of phase imaging in atomic force microscopy for measurement of viscoelastic contrast in polymer nanocomposites and molecularly-thick lubricant films, Ultramicroscopy **97**, 151–169 (2003)

27.70 B. Bhushan, J. Qi: Phase contrast imaging of nanocomposites and molecularly-thick lubricant films in magnetic media, Nanotechnology **14**, 886–895 (2003)

27.71 T. Kasai, B. Bhushan, L. Huang, C. Su: Topography and phase imaging using the torsional resonance mode, Nanotechnology **15**, 731–742 (2004)

27.72 N. Chen, B. Bhushan: Morphological, nanomechanical and cellular structural characterization of human hair and conditioner distribution using torsional resonance mode in an AFM, J. Micros. **220**, 96–112 (2005)

27.73 M.S. Bobji, B. Bhushan: Atomic force microscopic study of the micro-cracking of magnetic thin films under tension, Scr. Mater. **44**, 37–42 (2001)

27.74 M.S. Bobji, B. Bhushan: In situ microscopic surface characterization studies of polymeric thin films during tensile deformation using atomic force microscopy, J. Mater. Res. **16**, 844–855 (2001)

27.75 N.S. Tambe, B. Bhushan: In situ study of nano-cracking of multilayered magnetic tapes under monotonic and fatigue loading using an AFM, Ultramicroscopy **100**, 359–373 (2004)

27.76 M. Palacio, B. Bhushan: Normal and lateral force calibration techniques for AFM cantilevers, Crit. Rev. Solid State Mater. Sci. **35**, 73–104 (2010)

27.77 M. Palacio, B. Bhushan: Erratum to: Normal and lateral force calibration techniques for AFM cantilevers, Crit. Rev. Solid State Mater. Sci. **36**, 261 (2010)

27.78 B. Bhushan, T. Kasai, C.V. Nguyen, M. Meyyappan: Multiwalled carbon nanotube AFM probes for surface characterization of micro/nanostructures, Microsyst. Technol. **10**, 633–639 (2004)

27.79 B. Bhushan: Micro/nanotribology and its applications to magnetic storage devices and MEMS, Tribol. Int. **28**, 85–95 (1995)

27.80 A. Avila, B. Bhushan: Electrical measurement techniques in atomic force microscopy, Crit. Rev. Solid State Mater. Sci. **35**, 38–51 (2010)

27.81 B. Bhushan, A.V. Goldade: Kelvin probe microscopy measurements of surface potential change under wear at low loads, Wear **244**, 104–117 (2000)

27.82 D.T. Lee, J.P. Pelz, B. Bhushan: Instrumentation for direct, low frequency scanning capacitance microscopy, and analysis of position dependent stray capacitance, Rev. Sci. Instrum. **73**, 3523–3533 (2002)

27.83 D. DeVecchio, B. Bhushan: Use of a nanoscale Kelvin probe for detecting wear precursors, Rev. Sci. Instrum. **69**, 3618–3624 (1998)

27.84 B. Bhushan, A.V. Goldade: Measurements and analysis of surface potential change during wear of single crystal silicon (100) at ultralow loads using kelvin probe microscopy, Appl. Surf. Sci. **157**, 373–381 (2000)

27.85 I.P. Seshadri, B. Bhushan: In-situ tensile deformation characterization of human hair with atomic force microscopy, Acta Mater. **56**, 774–781 (2008)

27.86 I.P. Seshadri, B. Bhushan: Effect of ethnicity and treatments on in situ tensile response and morphological changes of human hair characterized by atomic force microscopy, Acta Mater. **56**, 3585–3597 (2008)

27.87 H.U. Krotil, T. Stifter, H. Waschipky, K. Weishaupt, S. Hild, O. Marti: Pulse force mode: A new method for the investigation of surface properties, Surf. Interface Anal. **27**, 336–340 (1999)

27.88   U. Rabe, K. Janser, W. Arnold: Vibrations of free and surface-coupled atomic force microscope cantilevers: Theory and experiment, Rev. Sci. Instrum. **67**, 3281–3293 (1996)

27.89   V. Scherer, B. Bhushan, U. Rabe, W. Arnold: Local elasticity and lubrication measurements using atomic force and friction force microscopy at ultrasonic frequencies, IEEE Trans. Magn. **33**, 4077–4079 (1997)

27.90   J. Tamayo, R. Garcia: Deformation, contact time, and phase contrast in tapping mode scanning force microscopy, Langmuir **12**, 4430–4435 (1996)

27.91   R. Garcia, J. Tamayo, M. Calleja, F. Garcia: Phase contrast in tapping-mode scanning force microscopy, Appl. Phys. A **66**, S309–S312 (1998)

27.92   Y. Song, B. Bhushan: Quantitative extraction of in-plane surface properties using torsional resonance mode in atomic force microscopy, J. Appl. Phys. **87**, 83533 (2005)

27.93   Z. Tao, B. Bhushan: Surface modification of AFM silicon probes for adhesion and wear reduction, Tribol. Lett. **21**, 1–16 (2006)

27.94   B. Bhushan, J. Ruan, B.K. Gupta: A scanning tunnelling microscopy study of fullerene films, J. Phys. D: Appl. Phys. **26**, 1319–1322 (1993)

27.95   B. Bhushan, P.S. Mokashi, T. Ma: A new technique to measure poisson's ratio of ultrathin polymeric films using atomic force microscopy, Rev. Sci. Instrum. **74**, 1043–1047 (2003)

27.96   G.A. Tomlinson: A molecular theory of friction, Philos. Mag. **7**, 905–939 (1929)

27.97   D. Tomanek, W. Zhong, H. Thomas: Calculation of an atomically modulated friction force in atomic force microscopy, Europhys. Lett. **15**, 887–892 (1991)

27.98   E. Meyer, R. Overney, R. Luthi, D. Brodbeck, L. Howald, J. Frommer, H.J. Guntherodt, O. Wolter, M. Fujihira, T. Takano, Y. Gotoh: Friction force microscopy of mixed Langmuir–Blodgett films, Thin Solid Films **220**, 132–137 (1992)

27.99   C.D. Frisbie, L.F. Rozsnyai, A. Noy, M.S. Wrighton, C.M. Lieber: Functional group imaging by chemical force microscopy, Science **265**, 2071–2074 (1994)

27.100   V.N. Koinkar, B. Bhushan: Scanning and transmission electron microscopies of single-crystal silicon microworn/machined using atomic force microscopy, J. Mater. Res. **12**, 3219–3224 (1997)

27.101   S. Sundararajan, B. Bhushan: Topography-induced contributions to friction forces measured using an atomic force/friction force microscope, J. Appl. Phys. **88**, 4825–4831 (2000)

27.102   V.N. Koinkar, B. Bhushan: Effect of scan size and surface roughness on microscale friction measurements, J. Appl. Phys. **81**, 2472–2479 (1997)

27.103   B. Bhushan: *Principles and Applications of Tribology*, 2nd edn. (Wiley, New York 2013)

27.104   B. Bhushan: *Introduction to Tribology*, 2nd edn. (Wiley, New York 2013)

27.105   B. Bhushan, G.S. Blackman: Atomic force microscopy of magnetic rigid disks and sliders and its applications to tribology, ASME J. Tribol. **113**, 452–458 (1991)

27.106   K. Yamanaka, E. Tomita: Lateral force modulation atomic force microscope for selective imaging of friction forces, Jpn. J. Appl. Phys. **34**, 2879–2882 (1995)

27.107   I.P. Seshadri, B. Bhushan: Effect of rubbing load on nanoscale charging characteristics of human hair characterized by AFM based Kelvin probe, J. Colloid Interface Sci. **325**, 580–587 (2008)

27.108   O. Marti, H.-U. Krotil: Dynamic friction measurement with the scanning force microscope. In: *Fundamentals of Tribology and Bridging the Gap Between the Macro- and Micro/Nanoscales*, ed. by B. Bhushan (Kluwer, Dordrecht 2001) pp. 121–135

27.109   Z. Tao, B. Bhushan: A new technique for studying nanoscale friction at sliding velocities up to 200 mm/s using atomic force microscope, Rev. Sci. Instrum. **77**, 103705 (2006)

27.110   N.S. Tambe, B. Bhushan: Scale dependence of micro/nano-friction and adhesion of MEMS/NEMS materials, coatings and lubricants, Nanotechnology **15**, 1561–1570 (2004)

27.111   N.S. Tambe, B. Bhushan: Friction model for the velocity dependence of nanoscale friction, Nanotechnology **16**, 2309–2324 (2005)

27.112   N.S. Tambe, B. Bhushan: Durability studies of micro/nanoelectromechanical system materials, coatings, and lubricants at high sliding velocities (up to 10 mm/s) using a modified atomic force microscope, J. Vac. Sci. Technol. A **23**, 830–835 (2005)

27.113   N.S. Tambe, B. Bhushan: Identifying materials with low friction and adhesion for nanotechnology applications, Appl. Phys. Lett. **86**, 061906 (2005)

27.114   Z. Tao, B. Bhushan: Velocity dependence and rest time effect in nanoscale friction of ultrathin films at high sliding velocities, J. Vac. Sci. Technol. A **25**, 1267–1274 (2007)

27.115   O. Zworner, H. Holscher, U.D. Schwarz, R. Wiesendanger: The velocity dependence of frictional forces in point-contact friction, Appl. Phys. A **66**, S263–S267 (1998)

27.116   E. Gnecco, R. Bennewitz, T. Gyalog, C. Loppacher, M. Bammerlin, E. Meyer, H.-J. Guntherodt: Velocity dependence of atomic friction, Phys. Rev. Lett. **84**, 1172–1175 (2000)

27.117   J.S. Helman, W. Baltensperger, J.A. Holyst: Simple-model for dry friction, Phys. Rev. B **49**, 3831–3838 (1994)

27.118   C. Fusco, A. Fasolino: Velocity dependence of atomic-scale friction: A comparative study of the one- and two-dimensional tomlinson model, Phys. Rev. B **71**, 045413 (2005)

27.119   N.S. Tambe, B. Bhushan: Nanoscale friction and wear maps, Philos. Trans. R. Soc. A **366**, 1405–1424 (2008)

27.120   N.S. Tambe, B. Bhushan: Nanoscale friction mapping, Appl. Phys. Lett. **86**, 193102 (2005)

27.121   N.S. Tambe, B. Bhushan: Nanoscale friction-induced phase transformation of diamond-like carbon, Scr. Mater. **52**, 751–755 (2005)

27.122 S.C. Lim, M.F. Ashby: Wear mechanism maps, Acta Metall. **35**, 1–24 (1987)

27.123 S.C. Lim, M.F. Ashby, J.H. Brunton: Wear-rate transitions and their relationship to wear mechanisms, Acta Metall. **35**, 1343–1348 (1987)

27.124 N.S. Tambe, B. Bhushan: Nanowear mapping: A novel atomic force microscopy based approach for studying nanoscale wear at high sliding velocities, Tribol. Lett. **20**, 83–90 (2005)

27.125 B. Bhushan, C. Dandavate: Thin-film friction and adhesion studies using atomic force microscopy, J. Appl. Phys. **87**, 1201–1210 (2000)

27.126 T. Stifter, O. Marti, B. Bhushan: Theoretical investigation of the distance dependence of capillary and van der Waals forces in scanning probe microscopy, Phys. Rev. B **62**, 13667–13673 (2000)

27.127 B. Bhushan, H. Liu, S.M. Hsu: Adhesion and friction studies of silicon and hydrophobic and low friction films and investigation of scale effects, ASME J. Tribol. **126**, 583–590 (2004)

27.128 H. Liu, B. Bhushan: Adhesion and friction studies of microelectromechanical systems/nanoelectromechanical systems materials using a novel microtriboapparatus, J. Vac. Sci. Technol. A **21**, 1528–1538 (2003)

27.129 B. Bhushan, B.K. Gupta: *Handbook of Tribology: Materials, Coatings and Surface Treatments* (Krieger, Malabar 1997)

27.130 B. Bhushan, S. Venkatesan: Mechanical and tribological properties of silicon for micromechanical applications: A review, Adv. Inf. Storage Syst. **5**, 211–239 (1993)

27.131 Properties of Silicon, EMIS Data Reviews Series No. 4 (INSPEC, Institution of Electrical Engineers, London 1988)

27.132 J.E. Field: *The Properties of Natural and Synthetic Diamond* (Academic, London 1992)

27.133 National Carbon Company: *The Industrial Graphite Engineering Handbook* (National Carbon Company, New York 1959)

27.134 M. Nosonovsky, B. Bhushan: Scale effects in dry friction during multiple-asperity contact, ASME J. Tribol. **127**, 37–46 (2005)

27.135 B. Bhushan, M. Nosonovsky: Scale effects in friction using strain gradient plasticity and dislocation-assisted sliding (microslip), Acta Mater. **51**, 4331–4345 (2003)

27.136 B. Bhushan, M. Nosonovsky: Comprehensive model for scale effects in friction due to adhesion and two- and three-body deformation (plowing), Acta Mater. **52**, 2461–2474 (2004)

27.137 B. Bhushan, M. Nosonovsky: Scale effects in dry and wet friction, wear, and interface temperature, Nanotechnology **15**, 749–761 (2004)

27.138 X. Zhao, B. Bhushan: Material removal mechanism of single-crystal silicon on nanoscale and at ultralow loads, Wear **223**, 66–78 (1998)

27.139 W. Tang, B. Bhushan, S. Ge: Triboelectrification studies of skin and skin cream using Kelvin probe microscopy, J. Vac. Sci. Technol. A **28**, 1018–1028 (2010)

27.140 R.A. Lodge, B. Bhushan: Effect of physical wear and triboelectric interaction on surface charges measured by kelvin probe microscopy, J. Colloid Interface Sci. **310**, 321–330 (2007)

27.141 S.C. Nagpure, B. Bhushan, S.S. Babu: Surface potential measurement of aged li-ion batteries using kelvin probe microscopy, J. Power Sources **196**, 1508–1512 (2011)

27.142 U. Zaghloul, B. Bhushan, F. Coccetti, P. Pons, R. Plana: Kelvin probe force microscopy based characterization techniques applied for electrostatic MEMS and thin dielectric films to investigate the dielectric substrate charging phenomena, J. Vac. Sci. Technol. A **29**, 051101 (2011)

27.143 A.V. Kulkarni, B. Bhushan: Nanoscale mechanical property measurements using modified atomic force microscopy, Thin Solid Films **290/291**, 206–210 (1996)

27.144 A.V. Kulkarni, B. Bhushan: Nano/picoindentation measurements on single-crystal aluminum using modified atomic force microscopy, Mater. Lett. **29**, 221–227 (1996)

27.145 A.V. Kulkarni, B. Bhushan: Nanoindentation measurement of amorphous carbon coatings, J. Mater. Res. **12**, 2707–2714 (1997)

27.146 N.A. Fleck, G.M. Muller, M.F. Ashby, J.W. Hutchinson: Strain gradient plasticity: Theory and experiment, Acta Metall. Mater. **42**, 475–487 (1994)

27.147 W.D. Nix, H. Gao: Indentation size effects in crystalline materials: A law for strain gradient plasticity, J. Mech. Phys. Solids **46**, 411–425 (1998)

27.148 W.B. Li, J.L. Henshall, R.M. Hooper, K.E. Easterling: The mechanism of indentation creep, Acta Metall. Mater. **39**, 3099–3110 (1991)

27.149 F.P. Bowden, D. Tabor: *The Friction and Lubrication of Solids, Part 1* (Clarendon, Oxford 1950)

27.150 B. Bhushan, M. Palacio, B. Kinzig: AFM-based nanotribological and electrical characterization of ultrathin wear-resistant ionic liquid films, J. Colloid Interface. Sci. **317**, 275–287 (2008)

27.151 M. Palacio, B. Bhushan: Ultrathin wear-resistant ionic liquid films for novel MEMS/NEMS applications, Adv. Mater. **20**, 1194–1198 (2008)

27.152 M. Palacio, B. Bhushan: Molecularly thick dicationic liquid films for nanolubrication, J. Vac. Sci. Technol. A **27**, 986–995 (2009)

27.153 E. Hoque, J.A. DeRose, P. Hoffmann, H.J. Mathieu, B. Bhushan, M. Cichomski: Phosphonate self-assembled monolayers on aluminum surfaces, J. Chem. Phys. **124**, 174710 (2006)

27.154 E. Hoque, J.A. DeRose, G. Kulik, P. Hoffmann, H.J. Mathieu, B. Bhushan: Alkylphosphonate modified aluminum oxide surfaces, J. Phys. Chem. B **110**, 10855–10861 (2006)

27.155 E. Hoque, J.A. DeRose, P. Hoffmann, B. Bhushan, H.J. Mathieu: Alkylperfluorosilane self-assembled monolayers on aluminum: A comparison with alkylphosphonate self-assembled monolayers, J. Phys. Chem. C **111**, 3956–3962 (2007)

27.156 E. Hoque, J.A. DeRose, P. Hoffmann, B. Bhushan, H.J. Mathieu: Chemical stability of nonwetting, low adhesion self-assembled monolayer films

formed by perfluoroalkylsilazation of copper, J. Chem. Phys. **126**, 114706 (2007)

27.157   E. Hoque, J.A. DeRose, B. Bhushan, H.J. Mathieu: Self-assembled monolayers on aluminum and copper oxide surfaces: Surface and interface characteristics, nanotribological properties, and chemical stability. In: *Applied Scanning Probe Methods Vol. IX – Characterization*, ed. by B. Bhushan, H. Fuchs, M. Tomitori (Springer, Berlin, Heidelberg 2008) pp. 235–281

27.158   E. Hoque, J.A. DeRose, B. Bhushan, K.W. Hipps: Low adhesion, non-wetting phosphonate self-assembled monolayer films formed on copper oxide surfaces, Ultramicroscopy **109**, 1015–1022 (2009)

27.159   J.A. DeRose, E. Hoque, B. Bhushan, H.J. Mathieu: Characterization of perfluorodecanote self-assembled monolayers on aluminum and comparison of stability with phosphonate and siloxy self-assembled monolayers, Surf. Sci. **602**, 1360–1367 (2008)